COMPUTATIONAL BENCHMARKING IN BIOMIMETIC NICKEL, COPPER, AND IRON COMPLEXES

A Dissertation

by

SCOTT MICHAEL BROTHERS

Submitted to the Office of Graduate Studies of
Texas A&M University
in partial fulfillment of the requirements for the degree of

DOCTOR OF PHILOSOPHY

December 2011

Major Subject: Chemistry

COMPUTATIONAL BENCHMARKING IN BIOMIMETIC NICKEL, COPPER, AND IRON COMPLEXES

A Dissertation

by

SCOTT MICHAEL BROTHERS

Submitted to the Office of Graduate Studies of
Texas A&M University
in partial fulfillment of the requirements for the degree of

DOCTOR OF PHILOSOPHY

Approved by:

Chair of Committee,	Marcetta Y. Darensbourg
Committee Members,	Michael B. Hall
	Manuel P. Soriaga
	Daniel F. Shantz
	Donald J. Darensbourg
Head of Department,	David H. Russell

December 2011

Major Subject: Chemistry

ABSTRACT

Computational Benchmarking in Biomimetic

Nickel, Copper, and Iron Complexes. (December 2011)

Scott Michael Brothers, B.S., Wheeling Jesuit University

Chair of Advisory Committee: Dr. Marcetta Y. Darensbourg

Sophisticated catalytically active sites of metalloenzymes provide inspiration to synthetic chemists, as the metal coordination environments are often atypical to those found on the chemist's benchtop. Furthermore, metal-ligand cooperativity using earth-abundant metals is anticipated to eventually supplant noble metals, currently used in industrial catalysis. Despite progress in synthesis of small molecule active site models, reproduction of the enzymatic function is rarely observed. However, differences that might define catalytic efficiency of enzymes can be addressed by theory. Density functional theory, or DFT, has been developed as an *in silico* tool to complement and interpret crystallographic and spectroscopic results or to make predictions in the absence of experimental data. In this dissertation, such techniques serve to elucidate the observed reactivity or electronic character of both nickel and copper bound in square planar N_2S_2 ligand fields, and of $\{Fe(NO)_2\}$ units, respectively.

Nickel and copper complexes in tetraanionic $N_2S_2^{4-}$ ligand environments were investigated with respect to change of metal, to modification of ligand environment, and to response in reactivity of thiolate sulfur atoms. From the DFT calculations and

consistent with experimental observations, it was discovered that binding of a nucleophile at one thiolate sulfur effectively decreases reactivity of the second sulfur, and nucleophilic binding at both sulfurs serves to deactivate the complex toward further thiolate reactivity. Additionally, despite both Cu and Ni binding comfortably in the $N_2S_2^{4-}$ coordination sphere, the former displays increased ionicity versus the latter, demonstrated by electrostatic potential mapping.

A methodology for accurate modeling of geometry and vibrational frequencies of complexes containing a $\{Fe(NO)_2\}$ unit was determined from the results of a test set of complexes using a matrix of functionals and basis sets. Utilizing the optimum performer, the BP86 functional and a mixed SDD ECP basis set on iron and 6-311++G(d,p) on other atoms, a series of iron dinitrosyl complexes containing diverse ancillary ligands spanning the spectrochemical series was subsequently investigated. The electrochemical potentials of the pairs of "oxidized" and "reduced" DNIC complexes were evaluated for values occurring in the biological regime. Furthermore, as the $\{Fe(NO)_2\}$ unit is capable of coordination in interesting yet dissimilar geometric motifs, bimetallic, tetrameric, and adamantane-like DNIC complexes have been investigated with our DFT methodology.

DEDICATION

I dedicate this dissertation to all those who have inspired me to forge ahead in all my academic pursuits: Sarah Turner, Cheryl Brothers, Dr. Marcetta Y. Darensbourg, Dr. Michael B. Hall, Dr. Norman V. Duffy, Dr. Kayla N. Green, and Dr. Jennifer L. Hess. It is through your tireless enthusiasm and love of life that I am in this position today.

"The only people for me are the mad ones, the ones who are mad to live, mad to talk, mad to be saved, desirous of everything at the same time, the ones who never yawn or say a commonplace thing, but burn, burn, burn like fabulous yellow roman candles exploding like spiders across the stars and in the middle you see the blue centerlight pop and everybody goes 'Awww!'" (Jack Kerouac)

ACKNOWLEDGEMENTS

First and foremost, I would like to sincerely acknowledge my advisor, Dr. Marcetta Y. Darensbourg, who I will remember fondly as the one person to have such an infinite degree of patience with an ill-prepared novice student. The first time I ate lunch in the lunchroom you told me I was too young to appreciate the movie *Sideways*, and in my last year here you advised me to see *Midnight in Paris*, so barring anything else, that's progress, right? In all seriousness, I appreciate to an unexplainable degree how deeply you have helped me mature as a scientist and a person. Every former student of yours to which I have spoken has made it explicitly clear how tenaciously you fight for your students, and I fully agree from personal experience. You have taught me better how to think and to express my words and thoughts in a clear and rational manner. Your contributions to my growth will be always remembered. I thank you.

Without a doubt I must acknowledge my coadvisor, Dr. Michael B. Hall, for his multitude of contributions to my graduate student journey, even prior to my official joining of the group in both the Structure and Bonding class as well as consultation on the nickel and copper N_2S_2 studies. I deeply appreciate the hours spent poring over manuscripts and pointing out my many instances of repetition and of clarification of the details of the chemistry explored. In just two years, under your guidance, my understanding of computational and theoretical chemistry has increased exponentially, and now I feel comfortable passing the experience on to students in the future.

In this regard I would also like to gratefully acknowledge Dr. Lisa Perez and the entirety of the Laboratory for Molecular Simulation facility for both the man-hours and computer hours teaching me the techniques that I have used to expand preliminary and rudimentary studies into full-fledged published stories.

I would like to acknowledge the graduate students and post-docs in the Darensbourg and Hall laboratories with whom I have interacted and who have helped me, through advice, friendship, or both: Marilyn, Steve, Kayla, Elky, Leo, William, Roxanne, Mike, Jen, Mark, Tiffany, Ryan, Jason, Danielle, Randara, Eric, Shawn, Jeremy, Ross, Stephanie (Darensbourg), Li, Amanda, Caiping, Justin, Zhenggang, Ana, Ivica, and Eszter (Hall). In particular, I would like to acknowledge Chung-Hung (Mark) Hsieh for all of the talents and skills that have you have brought to our group. Your unending thirst for the field of chemistry is inspiring to all of us. The interesting projects under your auspices that you have bestowed upon our group have given me more meaningful data than I ever thought I would have to put together. Thank you.

Further reflection on my graduate school tenure leads to a strikingly common theme: guidance and friendship by strong women; namely Kayla Green and Jennifer Hess. Kayla, you were certainly my *de facto* mentor, whether you want to take responsibility for it or not, and not a day goes by that I don't remember how upbeat and wonderful the labs seemed when you were there to help me through projects or to receive my multitude of hugs. I learned more from you than any other single graduate student over the past several years. When times got rough, you put me back on a stable path, and I certainly have you to thank for achieving this milestone.

Jen, what can I say about you that hasn't already been incorrectly told in one of Jason's stories. You were my rock, my confidant, my motivation, and always there to give me a cheerful word of advice or a solid punch on the arm, whichever was appropriate to the situation. Our journeys have been crossed since my first day when I asked you for help in using the glovebox, and since then I know that we have brought out so much good in one another.

To all others who were always good for a laugh and a smile, don't think I've forgotten about you. Jeremy, your openness, honesty, and kindness drew me to our friendship, and your Southern-isms kept me there. Eric, from our first conversation about Simon and Garfunkel to our most recent encounter, I consider you a lifelong friend. Dempsey, never had I had a roommate as long as you, and it was a blast getting to get to know you. You have the single most dynamic personality that I have ever known. Ross, though we may have gotten off on the wrong foot, I am deeply lucky to have you as a friend.

I acknowledge all those from the Corner Table Club in college: Tim, RJ, Falbo, Levi, Virginia, Eric, Pat, Bethany, Shawn, Jason, Chuck, and all others past and present. Although we haven't kept in touch as well as we should have, I miss you all and all the times we had.

I want to sincerely thank Dr. Norman V. Duffy for being the best undergraduate advisor I could ask for. His caring and compassion and love for chemistry were unequalled for me at the time and have had an impact on all I have done in the past and

will do in the future. I appreciate the numerous recommendation letters, job opportunities, and simple email conversations over the last six years.

I want to thank my father Jeff for instilling in me a strong work ethic and demonstrating that self-improvement and the continued ability to love is always possible. I thank my sister Stacy and brother Steven for always caring about me and just being the best siblings for which one could ask. Thank you Adam and Jamie for bringing the most precious niece into the world. I hope I can be an important part of her life just as I hope you will be of my own.

I would be remiss in not outpouring my infinite love for the two strongest people in all of my life, my mother Cheryl and my best friend Joe "Tuna" Allen. No one I know has gone through the trials that you both have and weathered it with such strength and dignity. You are both sources of inspiration and strength for my life, and I don't know that I can ever repay all that you have both given to me. Your love, compassion, humor, and ability to completely listen to me are debts I may never be able to pay, but will always promise to try.

Finally, last but certainly not least, I would like to acknowledge the most important person in the world to me, Sarah Turner. To call you my muse would be to poetically understate the truth by such a large degree; you are so much more than that. I met you at a crossroads in my life, but everything has seemed so much clear and direct since you joined me on my journey. No one except you has ever made me feel such an overwhelming goodness and calmness simply by their presence. I am excited for wherever our lives may take us. I love you.

TABLE OF CONTENTS

LIST OF FIGURES

FIGURE Page

FIGURE Page

FIGURE Page

LIST OF TABLES

CHAPTER I

INTRODUCTION

In the past several decades, our understanding of bioinorganic chemistry, in particular those active sites containing metals capable of engaging in or promoting catalytic reactivity, has blossomed. Two examples of well-studied active sites of this nature are the [FeFe]-hydrogenase (H_2ase) active site, which is found to be a diiron site bridged by thiolate sulfurs and promotes uptake of protons and electrons to produce molecular dihydrogen[1] and the nitrogenase active site, which utilizes a FeMoCo cluster in order to fix atmospheric nitrogen gas and to produce ammonia.[2-4] Sketches of the active sites of these enzymes are found in Figure I-1.

While the majority of enzymatic active sites contain zinc, iron, or copper due to their relative abundance on earth, in some instances other metals are utilized in active site coordination environments, such as nickel in Acetyl Coenzyme A Synthase (ACS)[5-6] and Nickel Superoxide Dismutase (NiSOD).[7-8] Each of these examples contain nickel bound to nitrogen and sulfur, with the former in a Cys-Gly-Cys (N_2S_2) four-coordinate, square-planar motif, and the latter in utilizing a free N-terminus amino group of a histidine, the amide nitrogen and thiolate sulfur of a cysteine, and the thiolate sulfur of a second cysteine in order to make a square-planar, four-coordinate (N_2SS') motif or a square pyramidal five-coordinate ($N'N_2SS'$) motif dependent on the flexible imidazole group of the histidine, which is capable of binding at the axial fifth site. These structures

---

This dissertation follows the style of *Journal of the American Chemical Society*.

are described in Figure I-1. Note that two of the nitrogen donors are from deprotonated amides of the protein "backbone."

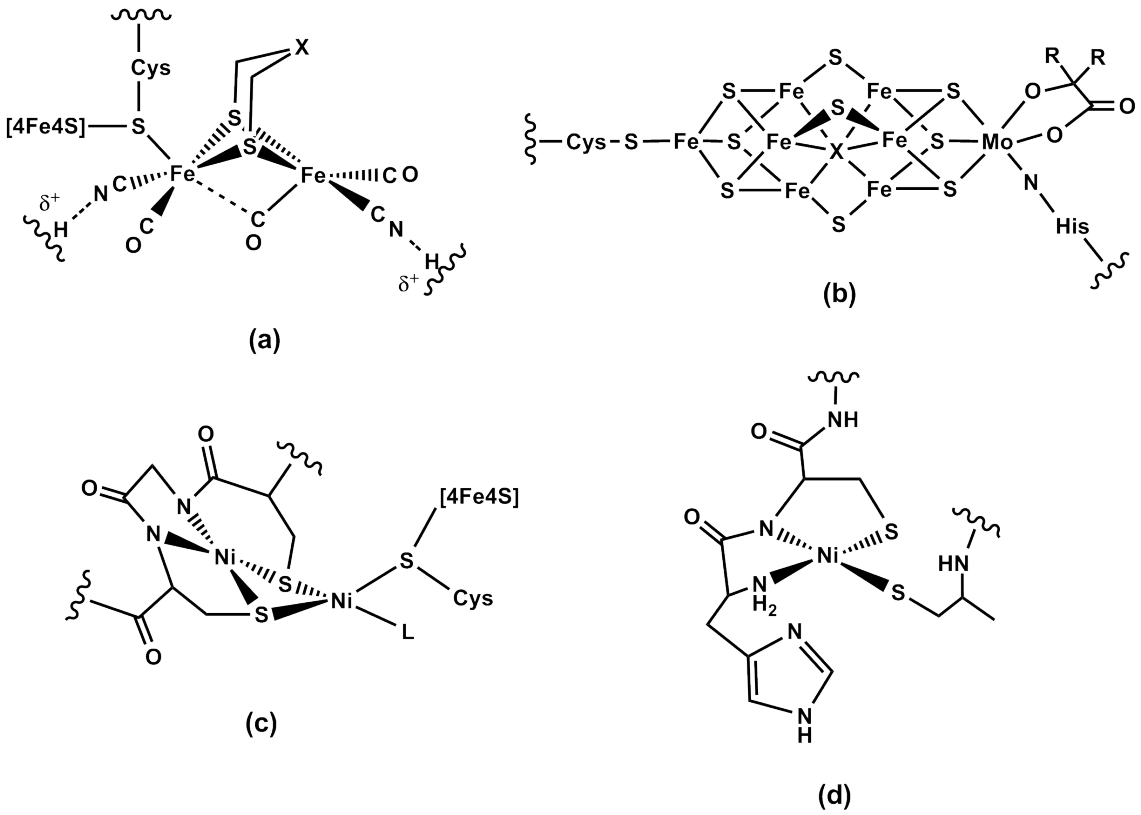

Figure I-1. Active site structures of [FeFe]-hydrogenase (a), the FeMoCo cluster of nitrogenase (b), Acetyl Coenzyme A Synthase (c), and $NiSOD_{red}$ (d).

Synthetic Approaches to NiN_2S_2 Complexes

Two metal sites were discovered in the ACS active site, defined as the distal site M_d, which is considered distant from the 4Fe4S cluster, and the proximal site, M_p, which is adjacent to the 4Fe4S cluster. Early crystal structures and reactivity studies indicated that the proximal metal could be Zn, Cu, or Ni; it was subsequently verified that only the nickel, Ni_p, showed enzyme activity.[5-6,9-10] While the Ni_p was "labile" and readily removed by exogeneous bases, the distal site was, for all intents and purposes, only found to bind Ni and to bind it tightly, see Figure I-1. In order to determine the role of the distal nickel site, a considerable effort was made to mimic its features. Even before the active site was elucidated, an excellent model of the dianionic distal site was reported by Holm and Krüger with uptake of nickel(II) into tetraanionic ligand templates of *N,N'*-ethylenebis(2-mercaptoacetamide) [ema^{4-}] and *N,N'*-ethylenebis(2-mercaptoisobutyramide) [emi^{4-}] (see Figure I-2) as well as the related phenylene derivatives.[11] These early models contained many of the features of the enzymatic distal site, i.e., an overall dianionic charge, contiguous N_2S_2 coordination environment, carboxyamido oxygens on the ligand architecture, and nickel in the appropriate oxidation state.[11] Although the ACS active site was not known at the time of the synthesis of these complexes, their electrochemical and electron paramagnetic resonance parameters were found to result in suitable mimics of the distal site of ACS upon its later discovery.[11]

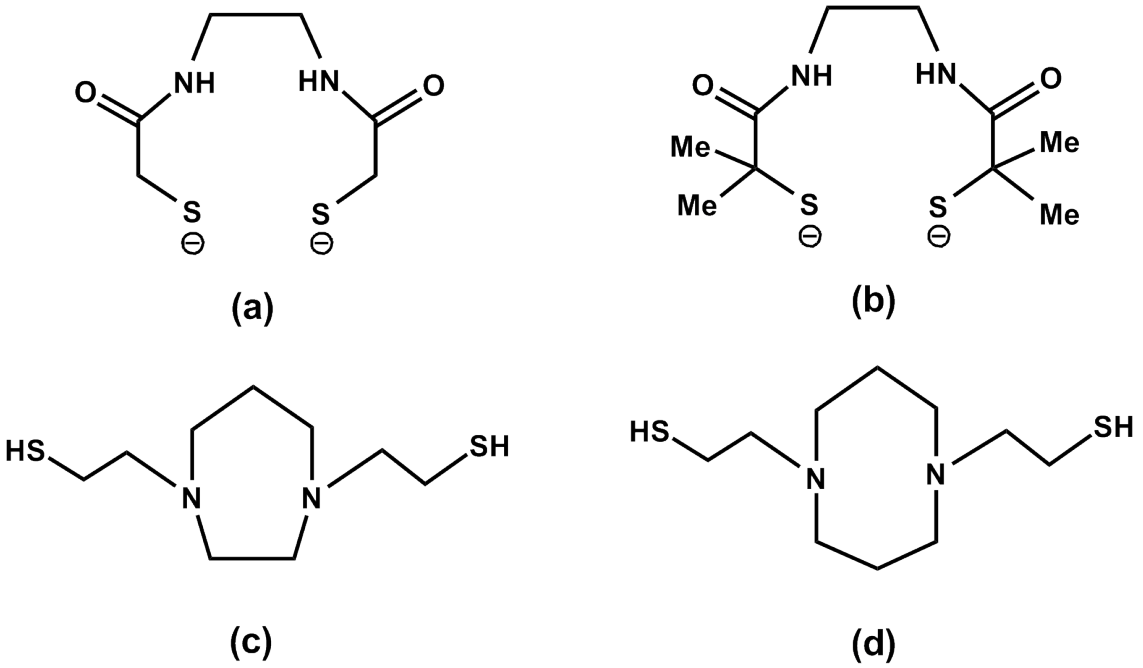

Figure I-2. Ligand architectures of $[H_2ema]^{2-}$ (a),[11] $[H_2emi]^{2-}$ (b),[11] $[H_2bme\text{-}dach]$ (c) and $[H_2bme\text{-}daco]$ (d).

Contemporary to these studies were similar investigations by the Darensbourg group utilizing dianionic N_2S_2 ligands such as *N,N′*-bis(2-mercaptoethyl)-1,4-diazacycloheptane) $[bme\text{-}dach]^{2-}$ and *N,N′*-bis(2-mercaptoethyl)-1,4-diazacyclooctane) $[bme\text{-}daco]^{2-}$ (see Figure I-2), forming overall neutral NiN_2S_2 complexes.[12-15] These complexes have been investigated in terms of S-based reactivity with a variety of reagents, such as metal sources, molecular oxygen, SO_2, and alkylating reagents to produce nickel-bound, sulfur modified products of S-metallation, S-oxygenation, and S-alkylation.[14,16-23] A strong nucleophilicity of the thiolate sulfurs was thus indicated and extended into a subsequent series of complexes that explored the ligating ability of the

NiN_2S_2 coordination complex to tungsten carbonyls, i.e., $[(NiN_2S_2)W(CO)_x]$, where x = 4,5.[23-25]

The donating ability of the $NiN_2S_2^x$ (x = 0, -2) complexes was explored via the $\nu_{(CO)}$ infrared data of the $[(NiN_2S_2)W(CO)_4]$ complexes,[23-26] as well as a series of $[(NiN_2S_2)Rh(CO)_2]^+$ complexes.[27-28] Upon gauging the $\nu_{(CO)}$ stretches of these complexes, it was determined that the dianionic $Ni(ema)^{2-}$ complex is a stronger donor than the neutral Ni(bme-dach) and Ni(bme-daco) complexes and related α-methylated derivatives, all of which have relatively identical carbonyl stretching frequencies. In turn, all of the NiN_2S_2 bimetallic complexes show lower $\nu_{(CO)}$ frequencies (stronger donation) than typical N- and P- donor ligands such as bipyridine, piperidine, and diphosphine ligands. These results, consistent with the reactivity of the thiolate sulfurs to electrophiles of strengths ranging from dioxygen to alkylating agents, indicate that the role of the distal metal site in ACS is to serve as both a donor unit and a structural component of the proximal metal site. Its presence promotes organometallic reactivity and electrochemical activity of Ni_p, as would a diphosphine ligand.

That the dianionic $NiN_2S_2^{2-}$ complexes were found to be the best metalloligands with respect to donor ability, ligand architecture, and physical features of the distal $Ni(CGC)^{2-}$ motif *in vivo*, peptide synthesis of the Cys-Gly-Cys^{4-} motif was investigated by both the Riordan and Darensbourg groups, specifically by Dr. Kayla Green.[27,29-30] As expected and as in a similar fashion to the reactivity described above for the $Ni(ema)^{2-}$ complex, the $Ni(CGC)^{2-}$ in both its free and resin-bound forms is capable of reacting with similar electrophilic reagents. Upon reaction with $(pip)_2W(CO)_4$, the

$[Ni(CGC)W(CO)_4]^{2-}$ was found to exhibit similar infrared frequencies to the non-peptidic $[(NiN_2S_2)W(CO)_4]^{2-}$ complexes.[27]

Recent work by Shearer, *et al.*, describes monoanionic $NiN_2S_2^-$ complexes containing one carboxyamido oxygen relevant to the NiSOD active site and exhibiting reactivity between the dianionic $NiN_2S_2^{2-}$ and neutral $NiN_2S_2^0$ complexes.[31-32] To this end, computational studies have been performed by Grapperhaus, *et al.*[33] and by us[34] to determine the orbitals responsible for reactivity and the nature of the distal metal motif both before and after complexation. Molecular orbital analysis, natural bond orbital analysis, and electrostatic potential mapping have been performed to elucidate the role of the Ni_d site, and the results from our laboratories are described in Chapter III.

Investigation of $M(N_2S_2)$ Complexes (M = Cu^{II}, FeNO, CoNO)

Similar to the NiN_2S_2 complexes described above, the tetradentate N_2S_2 chelating ligands are appropriate for a multitude of metals, among them Cu, Fe, Co, and Zn, each of which has a unique structural geometry. Copper binds as square planar Cu^{II} with slight tetrahedrality (full tetrahedrality is prohibited due to the rigidity of the N_2S_2 ligand); iron and cobalt are found as five-coordinate complexes in dimeric form $[M(N_2S_2)]_2$ or with an additional ligand bound in an axial position, i.e., $(NO)M(N_2S_2)$; and zinc prefers to bind in a five- or six-coordinate geometry, not uncommon for Zn^{II} with relatively strong field ligands.

Studies of CuN_2S_2 are of importance due to the fact that several of the initial crystallographic structures of the ACS active site found either Cu or Zn in the proximal

site. Nickel is now known by rigorous biological investigations to be the catalytically active metal in both sites,[9-10] agreeing with computation.[35] More specifically, we considered it important to understand whether the exclusion of copper from the distal coordination site was due to the aptitude of N_2S_2 chelates to preferentially bind nickel over copper.[30]

To date, only a few square-planar Cu^{II} complexes containing nitrogen and sulfur donation in the first coordination sphere have been isolated, several of these are shown in Figure I-3. Of note is $Cu(phmi)^{2-}$, denoted as (c) in Figure I-3, which is a Cu^{II} in a ligand set that, as described previously, appropriately models the distal site of ACS.[36] Interestingly, this complex was oxidized by bulk electrolysis to a stable Cu^{III} complex, which is a rarity in the literature, at a relatively negative potential of -1.16 V vs. Fc/Fc^{+}.[36]

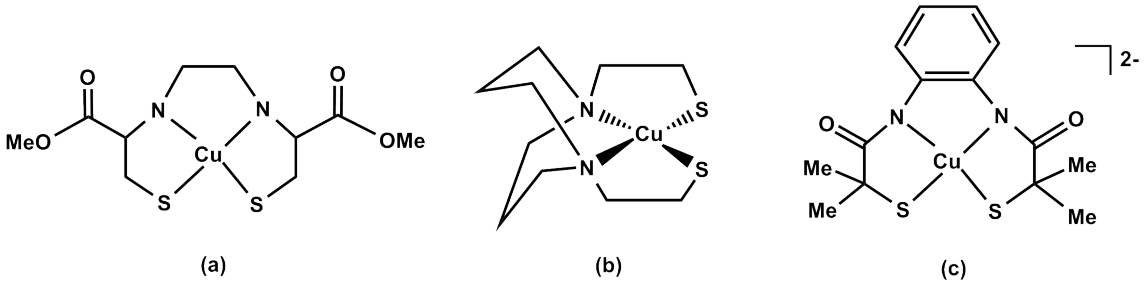

Figure I-3. Copper in square planar N_2S_2 ligand environments.[36-38]

Recent investigations in our laboratory have demonstrated that both Ni^{II} and Cu^{II} can be metallated into the tetradentate emi^{4-} and ema^{4-} ligands, and that the $CuN_2S_2^{2-}$ complexes of this series display even more negative $Cu^{III/II}$ electrochemical potentials of -1.40 V and -1.20 V with emi^{4-} and ema^{4-}, respectively. The former is, to our knowledge, the most negative potential of this type reported. Metal exchange studies of Cu^{II} and Ni^{II} could not reasonably predict a preference of either metal in the $N_2S_2^{4-}$ binding sites. Thus, it was concluded by metal exchange results that no physical analysis could rationalize the exclusion of Cu^{II} from the distal site of ACS and must instead be a consequence of a biosynthetic pathway.[30] Computational studies of these systems are a major focus of Chapter III.

The facility of the N_2S_2 complexes to bind a variety of metals led to some of the initial forays of the Darensbourg group into the realm of nitrosyl chemistry. Due to the preference of Fe^{II} and Co^{II} in N_2S_2 complexes to prefer square pyramidal geometries, the thermodynamic product of metal salts to the dianionic $N_2S_2^{2-}$ ligands has indicated five-coordinate metals in dimeric products of the form $[Fe(N_2S_2)]_2$, where the metal of each monomer is bound axially to a sulfur of the adjacent monomer.[39-41] The dimeric structure can be displaced in the presence of free nitric oxide (NO) to form the mononitrosyl complexes $(NO)Fe(N_2S_2)$ or $(NO)Co(N_2S_2)$, which have characteristic $\nu_{(NO)}$ infrared frequencies of ~1650 and 1600 cm^{-1}, respectively.[40-42] The S-based reactivity of these complexes tie into the NiN_2S_2 story as follows.

The extensive NiN_2S_2 investigations have been bridged to the nitrosyl chemistry, via the synthesis of bimetallic nickel-iron complexes that might mimic the active site of

[NiFe]-hydrogenase. Similar to a bimetallic structure reported by Pohl and coworkers in 1997, the structure of which is shown in Figure I-4,[43] complexes with the bme-daco ligand set were synthesized and are depicted in Scheme I-1.[40] In (A), the complex [Ni(bme-daco)Fe(NO)$_2$] was synthesized by 1) the addition of a Ni^{2+} source to the (H^+-bme-daco)Fe(NO)$_2$ complex in CH_3CN and 2) the introduction of the dinitrosyl reagent Fe(CO)$_2$(NO)$_2$ to a solution of Ni(bme-daco).[40]

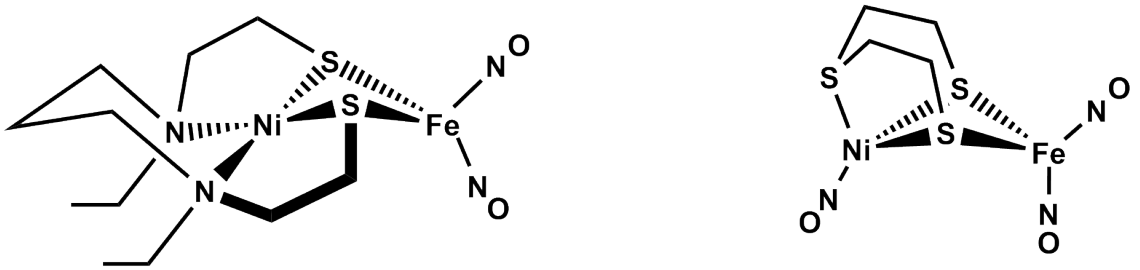

Figure I-4. [NiFe]-hydrogenase model containing N_2S_2 ligation and an iron dinitrosyl unit, and a (NO)Ni(S'$_3$)Fe(NO)$_2$ complex.[40,43]

The resultant complex presented similar structural features to that of the Pohl complex and infrared frequencies of 1677 and 1630 cm^{-1}, consistent with a reduced iron dinitrosyl complex. Similarly, a (NO)Ni(S'$_3$)Fe(NO)$_2$ complex, which had been reported previously was synthesized by two routes; 1) the addition of a $Ni^0(NO)^+$ source to (S'$_3$)Fe(NO)$_2^-$ and 2) the reaction of the well-characterized $[(SPh)_2Fe(NO)_2]^-$ complex in a solution of $NaNO_2$ and (NiS'$_3$)$_2$. The trinitrosyl product displays infrared frequencies

of 1798, 1763, and 1723 cm^{-1}, of which the latter two correspond to the dinitrosyl side and are typical of an oxidized DNIC; this reactivity is displayed in Scheme I-1 (B).[40] The biological relevance and importance of nitrosyls as well as the descriptive Enemark-Feltham notation utilized to describe this chemistry is defined in more detail below.

Scheme I-1

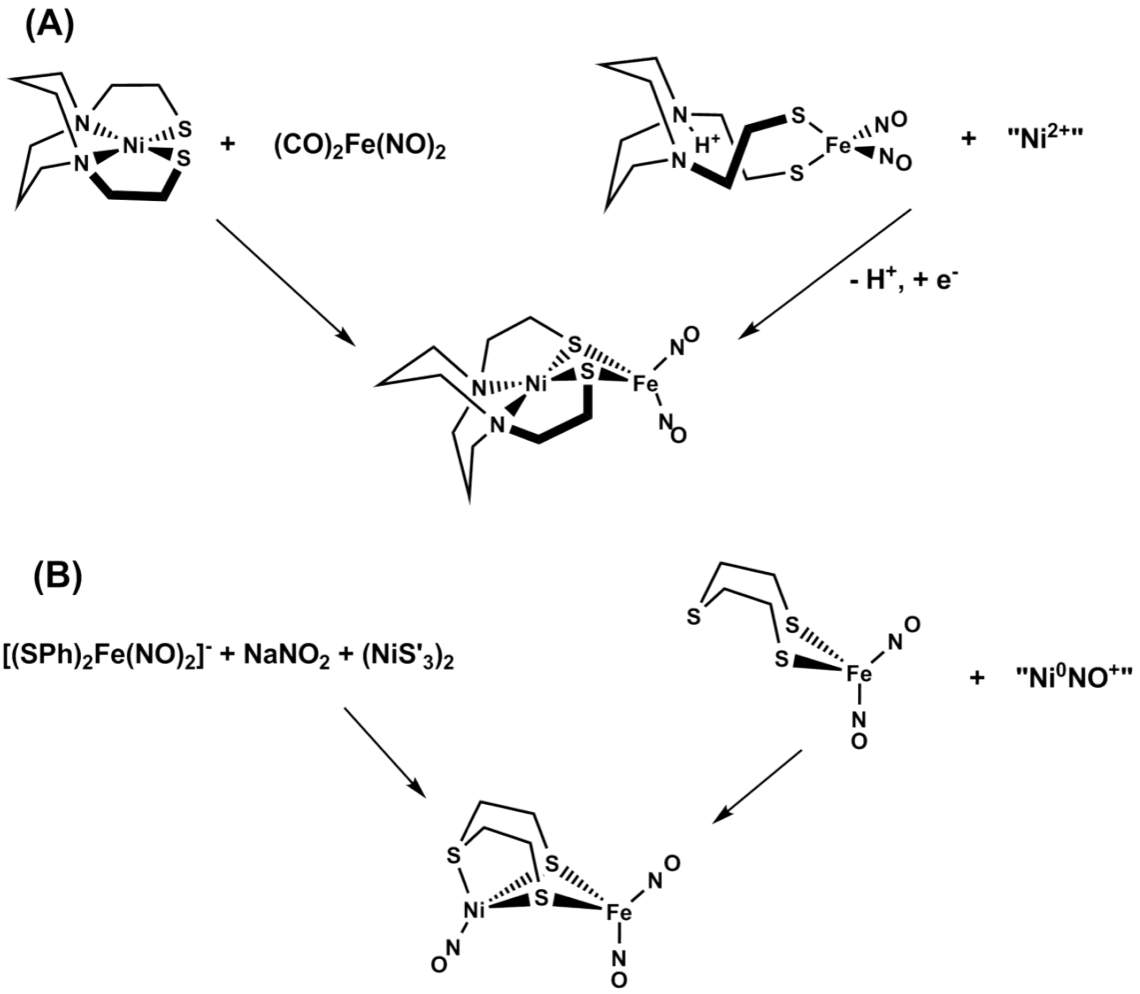

Fundamental Concepts Regarding Nitric Oxide

Nitric oxide formally exists in its ground state as a radical containing one unpaired electron. Other oxidation states of the nitric oxide molecule are the nitrosonium cation (NO^+), which is formally a ground state singlet and isoelectronic with carbon monoxide (CO), and NO^-, which typically exists as nitroxyl (HNO), and shares the triplet ground state of, and is isoelectronic with, dioxygen (O_2). For these reasons, nitric oxide serves as an interesting ligand to a variety of metal complexes and has been discovered in a number of enzyme active sites and in transport complexes in biology, discussed further, *vide infra*.

Because NO, upon binding to a metal center, can exist in three oxidation states and participate in redox chemistry, it is termed a "non-innocent" ligand due to the extensive delocalization possible between the metal and the NO ligand. The traditional view of M-N-O complexes has been to correlate the bond angle with the oxidation state of the nitrosyl ligand. In this simplistic view, a crystallographic bond angle of ~ 180º typifies nitric oxide in the NO^+ form, ~ 150º is in the neutral, radical form, and ~ 120º form.[44-46] This view, while accurate for a number of mononitrosyl complexes, becomes harder to correlate with other non-innocent ligands or additional nitrosyl ligands bound to the metal center.

In order to circumvent complexities and uncertainties that may arise from the non-innocent behavior of the NO ligand, a formalism has been developed in order to best describe such systems where the oxidation state of the metal may be difficult to

unambiguously distinguish. The notation used originally by Enemark and Feltham describes metal-nitrosyl complexes in the following manner:

$$\{M(NO)_x\}^y$$

In this formalism, the metal oxidation state is determined by spectator ligands. The variable labeled as *x* corresponds to the number of nitrosyl ligands bound to the given metal atom. The *y* value is determined of the sum of the M *d* electrons and the π^* electrons given a defined oxidation state for both the metal and the nitrosyl ligands.[44] Delocalization between the valence orbitals of iron and nitrosyl as ligand renders oxidation state assignments equivocal even in such a simple case as the mononitrosyl iron Fe(NO) unit, within a dianionic porphyrin ligand setting where alternate possibilities (neglecting the possible spin state ambiguities) exist as follows: a) $Fe^{I}(NO^{+})$ b) $Fe^{II}(NO^{\cdot})$ c) $Fe^{III}(NO^{-})$. All of these are, in the E-F, notation, $\{Fe(NO)\}^7$. Although the E-F notation avoids the oxidation state ambiguity, it hides the difficulty in description of the electronic structures that arise from the near degeneracy of the NO π^* and metal *d* orbitals. Despite this shortcoming, this notation will be used to describe iron nitrosyl systems for the remainder of this dissertation.

Biological Implications of Nitrosyl Chemistry

The field of nitrosyl chemistry has been of interest to chemists, particularly inorganic and bioinorganic chemists, for a number of years, in that the nitrosyl ligand can have inhibitory effects on biological processes, such as the mitochondrial respiratory chain as well as strongly binding to reduced hemoglobin reversibly under low

concentrations, inhibiting oxygen uptake.[47] It is also an atmospheric pollutant that subsequently oxidizes to NO_2.[48] Alternatively, the nitric oxide molecule has been discovered to play a significant role in beneficial biological processes[49] and is frequently used as a spin probe in metallobiochemistry. For this reason, in 1991 NO was named Molecule of the Year by the journal *Science*,[50] due to its role in biological functions as diverse as signaling and neurotransmission,[51-53] vasodilation,[54] and immunology.[55-56]

Additionally, it has been found that nitric oxide *in vivo* is closely associated with iron, such as occupying an axial site in nitrosyl heme complexes[57] or in the active site of the as-isolated, inactive nitrile hydratase enzyme, in which the Fe-NO unit is bound within a tripeptide N_2S_2 coordination sphere.[58-60] Complexes of these types, with one iron metal bound to a single nitrosyl ligand are termed mononitrosyl iron complexes (MNICs). These examples of biological MNICs are described in Figure I-5. While heme-Fe(NO) complexes have been investigated for decades, the recent biological discoveries of NO have led to a flurry of work from inorganic chemists with the goal of modeling biological iron dinitrosyl complexes and mimicking their NO-release properties.[40-42]

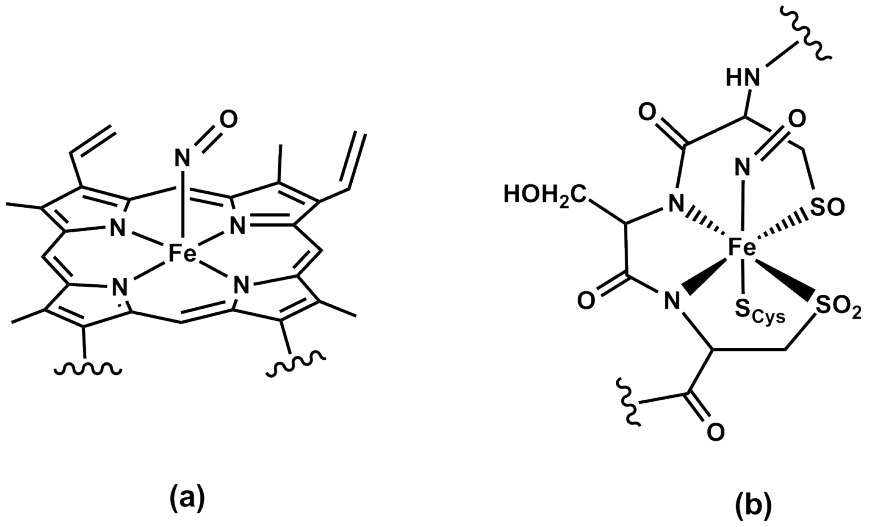

Figure I-5. Nitrosyl containing biological complexes. (a) Nitrosylated heme-*b*[57] (b) Active site of nitrile hydratase.[58-59]

Dinitrosyl Iron Complexes (DNICs)

Dinitrosyl iron complexes are a class of compound that exhibits a tetrahedral iron center bound to two nitrosyl ligands and either two monodentate or one bidentate ancillary ligands. This iron dinitrosyl unit is typified by two oxidation states given in the E-F notation as "oxidized" $\{Fe(NO)_2\}^9$ or "reduced" $\{Fe(NO)_2\}^{10}$, with features typically distinguished by infrared frequencies, presence or absence of EPR signal, or, in a number of more recent cases, electrochemical potentials and Mössbauer parameters. Biologically, both high-molecular weight (HMW), protein-bound DNICs and low-molecular weight (LMW), protein-free DNICs have been suggested, the former of which is presumed to act as an NO storage agent and the latter of which is presumed to act as an NO transport agent *in vivo*.[61-68]

As a result of iron-sulfur cluster degradation, HMW-DNICs have been proposed to be formed and protein bound through cysteinyl sulfurs. In fact, a recent example of a HMW-DNIC has been identified whereby an $\{Fe(NO)_2\}$ unit has been introduced to human glutathione transferase, producing a DNIC with both O- and S- binding through a phenolate oxygen and a glutathione sulfur, encouraging speculation in this field that other, endogenous HMW-DNIC complexes are apt to be discovered.[69] An example of a LMW-DNIC potentially released from the protein is the bis-cysteinyl $[(RS)_2Fe(NO)_2]^-$ species, in which the paramagnetic $[Fe(NO)_2]^+$ unit is described as the oxidized form of DNIC, with a signature g = 2.03 EPR signal. Over the last decade a number of sulfur and nitrogen containing DNICs have been synthesized and fully characterized, with the group of Liaw and coworkers as a strong contributor to this field.[64-67] Many of these syntheses resulted in the "Roussin's red ester" motif, which contains the structural core $[(NO)_2Fe(\mu\text{-}SR)_2Fe(NO)_2]$ with spin-coupled $\{Fe(NO)_2\}^9$ units. The RREs are largely considered to be thermodynamic sinks in iron dinitrosyl chemistry.[68,70-79] Another structural motif containing iron dinitrosyl units and first studied by Li, *et al.* has been in the tetrameric $[(Imid\text{-}H)Fe(NO)_2]_4$ unit, which is shown in Figure I-6.[80]

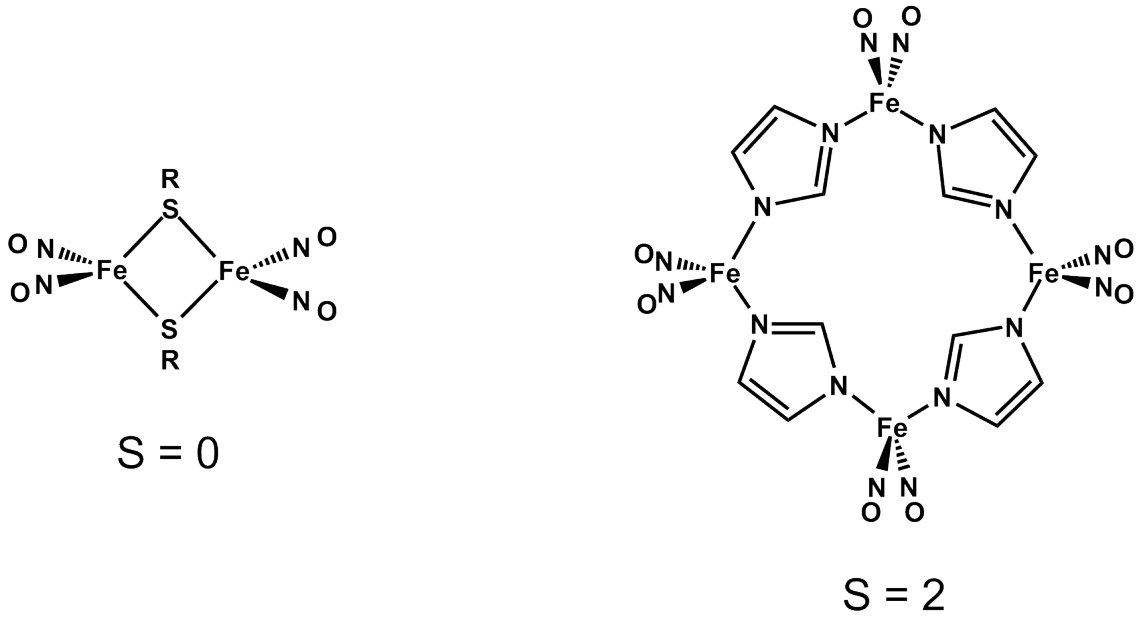

Figure I-6. Structure of a Roussin's Red Ester (RRE) and $[(Imid\text{-}H)Fe(NO)_2]_4$.

From the organometallic literature, diamagnetic dinitrosyl iron complexes were isolated and analyzed via several spectroscopic techniques, including infrared and Mössbauer spectroscopies, these complexes often contained carbon monoxide or abiological trialkylphosphine as ancillary ligands.[81-84] As the biological role for DNICs complexes has been borne out through the studies mentioned above, both synthesis and analysis of these complexes has been investigated using biological ligands, such as those containing S-, N-, and O-donation.[85-91] Recent studies have attempted to quantify and qualify the effects of the ancillary L ligands of $[(L)(L')Fe(NO)_2]$ complexes regarding donor ability and effect on geometric parameters and vibrational frequencies, through bidentate nitrogen donors such as bipyridine, by imidazole and N-heterocyclic carbene

ligands, and through conjugated bidentate ligands such as a β-diketimate. Examples of these classes of DNIC are shown in Figure I-7.[85,89-91]

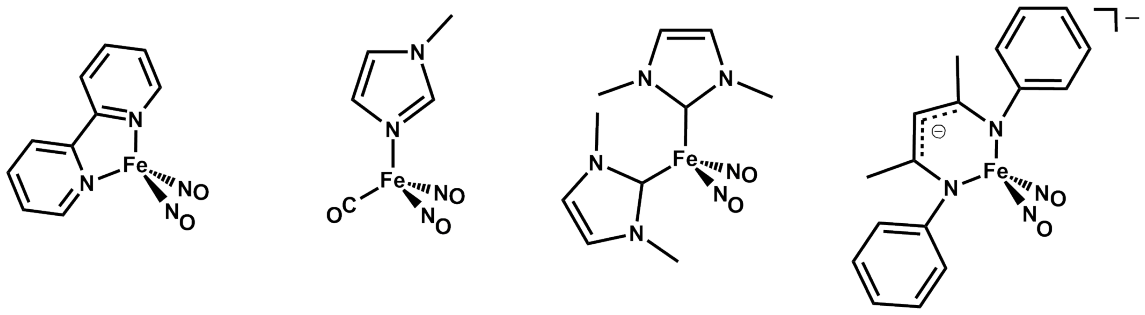

Figure I-7. Dinitrosyl iron complexes containing biologically-relevant ligands.[85,89-91]

Interestingly, in the β-diketimate case, which was formed upon introduction of NO to a Rieske-type model complex [(NRN')Fe(μ-S)$_2$Fe(SRS')], the complex [(NRN')Fe(NO)$_2$]$^{-/0}$ was synthesized and subsequently found to be stable in both the oxidized {Fe(NO)$_2$}^{9} and reduced {Fe(NO)$_2$}^{10} forms,[91] which was previously reported for only a few examples of DNIC, including phosphines.[81] Experimentally, the infrared data and electrochemical potentials indicated clearly the two oxidation states of these DNICs. However, the Mössbauer data indicated similar iron nuclei, with the isomer shift of the oxidized form of the complex at 0.19 mm/s and the reduced form at 0.22 mm/s.[90-91] Density functional theory calculations were undertaken by Ye and Neese in order to describe the electronic natures of two oxidation states and to elucidate the

similarities of the Mössbauer parameters.[92] In order to integrate these results with those of Ye and Neese, we have used density functional theory results for a range of DNICs containing ligands spanning the spectroelectrochemical series. These results are described below, Chapter V.

Density Functional Theory Approach to Biomimetic Active Site Modeling

Density functional theory, or DFT, is a powerful tool that has found increased utility over the past several decades to address geometric and spectroscopic modeling as well as to provide a technique by which reasonable transition states in a reaction pathway can be proposed. While traditionally DFT had been developed and used successfully in organic chemistry, through the expansion of basis set and functional design, an increased utility for calculation of transition metal complexes in both gas-phase and solution-phase has become ubiquitous.[93] Furthermore, inorganic chemists have embraced density functional theory for the facility of modeling physical inorganic and spectroscopic features, such as infrared frequencies,[94] electrochemical potentials,[95] spin densities and populations,[96] and Mössbauer parameters,[97] amidst myriad other characteristics. The utility of density functional theory to modern inorganic chemists has recently been elegantly described by Frank Neese.[98] Pitfalls also may abound.

From a bioinorganic standpoint, DFT calculations have been invaluable. The isolation of a metalloenzyme active site within a protein permits gas phase calculations to be particularly appropriate to a step by step reaction profile. A notable example of the utility of density functional theory to address current issues in biomimetic modeling has

been in the field of mechanism prediction of certain active sites. A large part of the initial modeling of the reactivity of the [FeFe]-H_2ase and [NiFe]-H_2ase was investigated by the Hall group at Texas A&M University. Through their work and others, it was determined that a high-spin Ni^{II} may be responsible for the reactivity exhibited by the enzyme; additionally, hemilability of a Ni_p-S bond was also invoked (see Figure I-8).[35,] By comparison, mechanistic studies on the reactivity at the ACS active site have been proposed from experimental results, with one example indicating a Ni^{I} proximal site which oxidatively adds CH_3^+ and CO in subsequent steps with redox participation by a 4Fe4S cluster.[99] A second proposed mechanism describes a Ni^0 proximal site that undergoes CO and CH_3^+ addition in subsequent steps, with the oxidation state change of the proximal metal due to an oxidative addition of the methyl group.[6] The original computational mechanism by the Hall group is a combination of these possibilities, with a Ni^0 proximal site but with CH_3^+ oxidative addition followed by CO uptake and insertion in that order as a possibility for the stepwise reactivity of the ACS active site, shown in Figure I-8.[35]

The computational methodology chosen, *i.e.*, functional and basis set can be significant to the calculated parameters of interest, in terms of adequate modeling of geometries, thermodynamic parameters, energies, and spectroscopic values. In one example, the pure (that is, no Hartree-Fock exchange energy) functional BP86 is known to perform poorly upon calculation of energies, whereas bond distances and angles (geometric parameters) as well as frequencies are calculated quite accurately.[98] Other functionals of fairly advanced utility in modern computational chemistry are PW91

(adept at exchange couplings), B3LYP (standard functional for most parameters),[100-101] and TPSS (functional *sans* chemically derived parameters).[102] Additional description of DFT methods is given in Chapter II and their applications to iron dinitrosyl chemistry is found in Chapter IV.

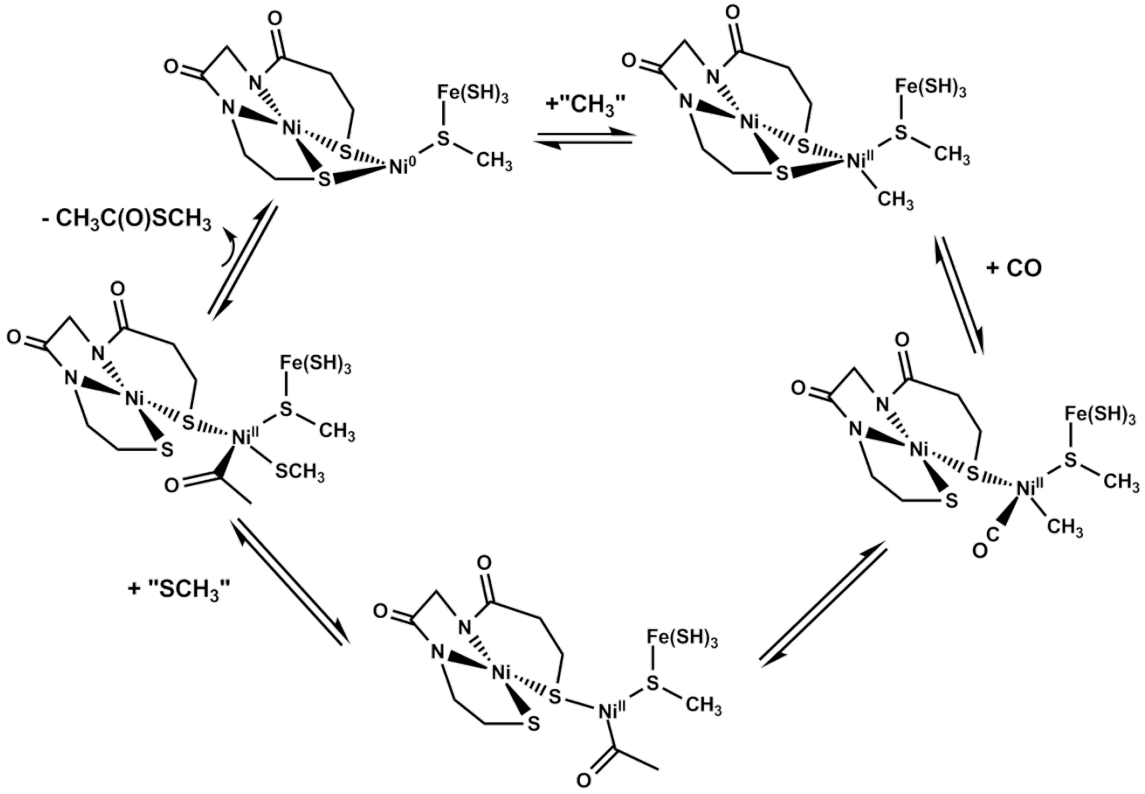

Figure I-8. Hall mechanism of insertion in the ACS active site.[35]

In the work described within my dissertation, DFT has been utilized to address the challenges of adequate biomimetic modeling of structures, electronic effects, and

spectrochemical features. Chapter III describes calculations used to identify metal effects in a rigid N_2S_2 core and to attempt to explain both thiolate reactivity and understanding of preference or exclusion of certain metals within the active site of Acetyl Coenzyme A Synthase. In Chapter IV, a computational methodology is determined through a number of basis set functional pairs in order to best corroborate DFT results to experiment. Chapters V and VI describe results aiming to elucidate the effect of ancillary ligands or metalloligands on the electron distribution in the delocalized iron dinitrosyl units and oxidation states.

CHAPTER II

COMPUTATIONAL METHODOLOGY

Abbreviations

AGUI = AMPAC Graphical User Interface

B3LYP = Three-parameter exchange functional of Becke (B3) and the correlation functional of Lee, Yang, and Parr (LYP)

BP86 = Becke exchange functional (B) and Perdew 86 correlation functional (P86)

cc-pVDZ = Dunning's correlated consistent polarized valence double-ζ basis set

cc-pVTZ = Dunning's correlated consistent polarized valence triple-ζ basis set

DFT = Density functional theory

DZP = Double-ζ + polarization

ECP = Effective core potential

ema = *N,N'*-ethylenebis(2-mercaptoacetamide)

emi = *N,N'*-ethylenebis(2-mercaptoisobutyramide)

eV = Electron volts

G03 = *Gaussian 2003* version

G09 = *Gaussian 2009* version

M06 = Hybrid functional of Truhlar and Zhao.

LANL2DZ = Los Alamos National Laboratory double-ζ basis set

NBO = Natural bond orbital

PCM = Polarizable continuum model

SDD = Stuttgart-Dresden basis set

THF = Tetrahydrofuran

TPSS = τ-dependent gradient corrected pure functional of Tao, Perdew, Staroverov, and Scuseria

TPSSh = Hybrid version of TPSS functional

ωB97X-D = Hybrid functional of Head-Gordon and coworkers, which contains empirical dispersions.

Computational Chemistry: Classical and Quantum Mechanical Approaches

Computational chemistry is a branch of chemistry that integrates the mathematics of classical-mechanical (*i.e.*, Newtonian) atoms and/or quantum-mechanical subatomic particles with computers in order to calculate the properties of a chemical system, particularly the structure and energy of the species and their spectroscopic signatures.[103]

The successful development of these techniques and their subsequent usage has been a major achievement of computational chemistry, with respects to its ability to serve as a predictive tool in ever more complex chemical systems. Previously, questions of this kind were solved by reducing the rigorous mathematics to phenomenological models that could be solved without the aid of computational resources. Modern computational chemical techniques find application in areas as vastly different as drug and catalyst design, mechanistic chemistry, solid-state chemistry, and biochemistry of enzymes.

The technique known as molecular mechanics (MM) involves implementation of classical mechanics to molecules, in which the atoms in the molecule behave as single particles with chemical characteristics introduced as empirical parameters. Typically, harmonic potentials are used to represent the interactions between atoms, where the entire set of potentials representing bond lengths and bond angles is referred to as the force field. In addition to the harmonic forces between atoms, electrostatic and Van der Waals (London) forces are also added.[104] A given force field is purely empirical, with atomic charges, radii, typical geometry parameters, and energy functions built into the force field by values determined from experiment or quantum-level calculation.

For example, in a simple diatomic molecule the force field for the bonding interaction is modeled as a spring (Hooke's Law) connecting the two atoms, with the empirical parameters of the force field, the spring constant and the resting position, determining the stretching frequency and the equilibrium distance, respectively. In a large molecule a steepest-descent energy minimization process is used to determine an overall optimal solution. As the force field is built from empirical parameters, the solution can be quite accurate for systems very close to the system from which the parameters were obtained, but the procedure has less general applicability to systems for which parameters have not been accurately determined. Generally, force field techniques find their greatest application in systems that are quite large, such as proteins, where the types of bonds are well known and the size makes this computationally rapid technique advantageous.

In systems not well parameterized, such as transition metal complexes, and in chemical reactions that involve bond breaking and bond making, other techniques are more suitable. Rather than energy minimization through an artificial force field built from empirical parameters as described above, quantum mechanical computational techniques that solve for the energy as a function of the many-electron wavefunction ψ and the electronic molecular Hamiltonian $\hat{H}$.[98,103] Here, the application of the theory involves the interaction of the fundamental particles that make up the atoms: protons, neutrons and electrons. In computational chemistry these techniques are known as *ab initio* (from first principles) techniques. A description of quantum mechanical theorems and *ab initio* techniques is given below.

Schrödinger Equation

The Schrödinger equation (II-1, 2, 3) provides a quantum mechanical solution of physical systems, which begins at the submicroscopic scale of nuclei and electrons but can also describe the microscopic level such as atoms, molecules, and nanoparticles (typically the types of system investigated by chemists) and the macroscopic level.[105] The solution of these equations yields the quantum state of a physical system as the wavefunction ψ, which contains information on the spin, position in space, and time dependency of the given set of particles (electrons and nuclei). The square of the wavefunction ψ^2 corresponds to the probability of finding a particle in a given location.

The two most common forms of the Schrödinger equations are the time-dependent equation, which is shown in Equation II-1 and has a time term, t, indicative

that this form of the equation represents a dynamic system evolving with time as implied by its nomenclature. The second most frequent form is the time-independent form, found in Equations II-2 and II-3, which are the more commonly used forms of this equation in computational chemistry methods.[98,103,105]

$$\hat{H}\Psi = i\hbar\frac{\partial}{\partial t}\Psi \tag{II-1}$$

$$\hat{H}\psi = E\psi \tag{II-2}$$

$$E\psi(r) = -\frac{\hbar^2}{2m}\nabla^2\psi(r) + V(r)\psi(r) \tag{II-3}$$

In these equations, *V(r)* corresponds to the time-independent potential energy at a given position, $-\frac{\hbar^2}{2m}\nabla^2$ corresponds to the kinetic energy operator, *m* corresponds to the mass, and ψ(r) corresponds to the wavefunction at a given position. According to Equation II-2, the time-independent form of the Schrödinger equation relates the total energy of the system *E* to the Hamiltonian operator $\hat{H}$ with wavefunctions ψ, which, as described above, is related to a probability density for particles as a function of space, spin, or momentum.[98]

Born-Oppenheimer Approximation

The Born-Oppenheimer approximation is a quantum mechanical approximation that utilizes experimentally known phenomena to eliminate terms from the Schrödinger equation, in essence, simplifying and facilitating the solution.[106] Specifically, the full Hamiltonian of the Schrödinger equation contains terms based on Coulombic

interactions between and kinetic energies of both electrons and nuclei. In order to simplify this equation, the Born-Oppenheimer approximation recognizes differences in relative masses of the nuclei versus electrons. One can then assume that the lighter electron moves so much faster than the heavier nuclei that the term coupling electronic and nuclear motion (T_N) is negligible and can be eliminated from the Schrödinger equation. Thus, for molecules, one can compute the motion of the electrons at fixed nuclear positions and then change the nuclear positions and recompute the electron motion, a process that will generate the potential energy in which the nuclei move. In this manner, the nuclear-nuclear repulsion is unchanging and is thus held constant during each electronic energy determination (V_{NN} term in Equation II-4).[98,103,107] A general form of the Born-Oppenheimer-modified Schrodinger equation is given in Equation II-4 and II-5 and the form of the equation as it relates to the time-independent Schrödinger equation is shown in Equation II-6. These approximations have been used in the realm of quantum computational chemistry since its inception.[98,103,105]

$$\hat{H}_{BO} = T_e + V_{eN} + V_{ee} + V_{NN} \tag{II-4}$$

$$\hat{H}_{BO} = -\frac{1}{2}\sum_{i=1}^{N}\nabla_i^2 - \sum_{i=1}^{N}\sum_{A=1}^{M}\frac{Z_A}{|r_i - R_A|} + \frac{1}{2}\sum_{i=1}^{N}\sum_{j>i}^{N}\frac{1}{|r_i - r_j|} + \frac{1}{2}\sum_{A=1}^{M}\sum_{\substack{B=1 \\ A\neq B}}^{M}\frac{Z_A Z_B}{|R_A - R_B|} \tag{II-5}$$

$$\hat{H}_{BO}\psi(x_1,...,x_N|R_1,...,R_M) = E\psi(x_1,...,x_N|R_1,...,R_M) \tag{II-6}$$

Quantum Chemistry, *Ab Initio* Techniques, and Semi-Empirical Techniques

Over the last half-century, a wide variety of computational techniques have been developed to solve the molecular Hamiltonian in order to describe molecular systems.

The level of empirical assumptions built into the methodology has traditionally defined the type of calculation, the relative computational cost, and the ability to approach an exact solution of the Schrödinger equation. Methods that forego empirical assumptions altogether, *i.e.*, solving the molecular Hamiltonian from "first principles" alone, are referred to as *ab initio* techniques. *Ab initio* techniques operate strictly on fundamental constants contained in quantum chemical theory, and calculations of this type usually begin at the Hartree-Fock formalism, whereby an *N*-electron wavefunction of some molecule can be approximated by a single determinant of molecular orbitals to solve the Schrödinger equation. If the average motion of the electrons described by this single determinate is not accurate enough, one can add additional determinants to the wavefunction so that it will provide an improved solution by including the correlated motion of the electrons. In this way, series of non-linear equations is produced and solved iteratively to a desired level of accuracy.[103]

One concern with *ab initio* calculations is in the scaling of larger molecules. *Ab initio* calculations are well suited to produce solutions approaching the exact solution of the Schrödinger equation for relatively small systems; however, the cost of the calculation scales as a high power of N with increasing size of the molecule. While this may be a deterrent for usage of *ab initio* techniques for many-atom systems; with sufficient resources and time even very large systems will converge to solutions nearing the exact Schrödinger solution.[103]

Subsequent to the original description of *ab initio* calculations, new techniques have been developed which combine *ab initio* methodology with a number of empirical

approximations. These calculations are referred to as semi-empirical. Furthermore, the development of density functional theory (DFT) has grown over the last several decades, and is now often the computational method of choice of transition metal complexes.

Density Functional Theory and Functionals

Density functional theory, while initially utilized mainly in solid-state chemistry and physics, has recently become more ubiquitous due to comparable performances in energy minimization and modeling of thermochemical parameters of molecules to the techniques that examine the many-electron wavefunctions directly, such as the *ab initio* theory mentioned above.[98,103] DFT can operate as a suitable alternative to these techniques due the use of functionals, named for functions of a given function. Specifically, in the case of DFT, the many-electron wavefunction can be replaced by the spatially-dependent electron density. One benefit of DFT over *ab initio* methods is the overall computational cost; the cost of DFT scales as N^3 whereas *ab initio* scales as N^4 or greater, indicating that if ρ is a adequate substitute for the many-electron wavefunction of a given system, then DFT methods can be utilized at a fraction of the overall computational cost.

The theoretical basis for density functional theory was originally proven by the work of Hohenberg, Kohn, and Sham.[108-109] Originally, Hohenberg and Kohn proved that "the full many particle ground state is a unique functional" of $\rho(r)$, where $\rho(r)$ is the density. This is known as the Hohenberg-Kohn Theorem.[108] The overall conclusions from the work of Hohenberg and Kohn was related to, in part, the earlier work of

Thomas and Fermi,[110,111] which made assumptions that electrons behave like a classical liquid; however, the utility of the H-K Theorem does not require such assumptions, as their proof indicates that a universal functional exists that is determined from the electronic density.[108] The electronic ground state was found to be exact where there is a nearly constant or a slowly varying density.[108] The Hohenberg-Kohn Theorem states that the molecular Hamiltonian $\hat{H}$ can be deduced from $\rho(\mathbf{r})$, and the exact energy can be solved within the Born-Oppenheimer Approximation if the functional is known. This functional can be written as shown in Equation II-7:[98]

$$E[\rho] = V_{NN} + V_{eN}[\rho] + J[\rho] + T[\rho] + E_{XC}[\rho] \tag{II-7}$$

The latter term $E_{XC}[\rho]$ is the exchange-correlation functional, which Kohn and Sham have described.[109]

By using the Kohn-Sham energy expression,[109] the total energy functional can be described as

$$E[\rho] = 2\sum_{i=1}^{Nel/2} \int \psi_i^*(r)\left(-\frac{1}{2}\nabla^2\right)\psi_i(r)dr + E_{Coul}[\rho] + E_{ext}[\rho] + E'_{XC}[\rho] \tag{II-8}$$

where the terms are, from left to right, the kinetic energy term, the Coulombic interaction term, the external potential of the real system, and the exchange-correlation functional. It should be noted that the $E'_{XC}[\rho]$ terms in Equation II-8 includes a correction for the fact that Kohn-Sham replaces the kinetic energy functional $T[\rho]$ in Equation II-7 with an approximate kinetic energy based on a single determinant wavefunction.

The exchange interactions between electrons, originally discovered by Heisenberg[112] and Dirac[113] arise because the solution for the motion of the electrons must be antisymmetric with respect to the interchange or exchange of electrons in a given system. The exchange functional is one that has been investigated and developed by many researchers over the past several decades, and the functionals are defined broadly as pure or hybrid functionals, with the terminology referring to the amount of non-local, exact Hartree-Fock exchange integrated into the method. The "pure" functionals contain no Hartree-Fock exchange, and "hybrid" functionals contain some fraction of Hartree-Fock exchange, dependent on the particular functional. To date, exchange functionals developed by Becke (identified as B or B3) have been the standard in modern DFT.[100,114]

In order to provide a suitable model for the exchange and correlation interactions denoted as $E_{XC}[\rho]$, the exchange functionals described above must be coupled with correlation functionals. The correlation energy refers to the correlation of electrons relative to the movement of other electrons (referred to as dynamic correlation) and to cases where a single Slater determinant cannot accurate describe the ground state in the Hartree-Fock description (referred to as static correlation). It is important to realize that a portion of the correlation corresponding to the correlation of electrons with the same spin (ferromagnetism) is accounted for in the exchange functional, due to the inability of two same-spin electrons existing at the same point in space. Popular correlation functionals in density functional theory have been the 1986 functional developed by Perdew (P86)[115] and the functional developed by Lee, Yang, and Parr (LYP).[101]

Thus, a combined exchange and correlation functional must be implemented in tandem with basis sets defined for the atoms, which are mathematical descriptions of the atomic orbitals of a given atom, in order to solve for the Kohn-Sham energy/Hamiltonian. The common nomenclature of the total functional is a combination of the exchange and correlation functionals, such as B3LYP or BP86, which are standard hybrid and pure functionals, respectively.[100-101,114-115] Other functionals such as TPSS[102] or its hybrid version TPSSh[102] have been finding utility, as well as ωB97x-D, which is a hybrid functional containing long-range correlation effects and dispersion terms.[116] The field of functional design is one that has grown largely due to the applicability and facility of computational chemistry due to the development of density functional theory.

A Broken-Symmetry Approach to DFT

In systems with the possibility of weak electronic coupling, *i.e.*, ferromagnetic or antiferromagnetic coupling, often density functional theory struggles to converge to the appropriate wavefunction, which is extremely method dependent. In systems of this nature, where the electronic state is difficult to define adequately due to a non-innocence ligand or extensive delocalization over several metal or metal-ligand combinations, DFT can be used to start an initial guess at a predetermined, usually high-spin state and then localized orbitals are used to converge the lower-spin states. This methodology is known as the "broken-symmetry" approach that has been developed by Noodleman, *et al.*,[117] originally used for investigations of iron-sulfur clusters[118] and expanded to systems as diverse as metal-imidazolate bridged systems and iron nitrosyl complexes. In

the latter case, that is (L^{2-})Fe(NO) complexes, the Fe(NO) unit could be described as $Fe^{III}(NO^{-})$, $Fe^{II}(NO^{\bullet})$, or $Fe^{I}(NO^{+})$. In a broken-symmetry approach, the system is first calculated as a fully ferromagnetic unit, for example, the $Fe^{III}(NO^{-})$ system would be calculated fully ferromagnetically with 7 unpaired electrons due to the 5 *d* electrons from Fe and the 2 π^{*} electrons on NO^{-}, noted as (5, 2). With this wavefunction, the two other spin descriptions, (4, 1), and (3, 0), can be calculated by manually changing the spin of the metal and nitrosyl units in the software, and the energies and geometries of the different spin descriptions can be evaluated. An expanded explanation of the broken-symmetry method for dinitrosyl iron complexes is found in Chapter V.

General Methodological Details

All density functional and related calculations were performed using the *Gaussian* software suites, either *G03*[119] or *G09*[120], except for Mössbauer calculations, which were performed using *ORCA*.[121] The specific programs used for each chapter are listed in the following methodological sections. Initial guesses for geometry optimizations were started from the crystallographic coordinates whenever available, and in cases where no crystallographic coordinates were available, reasonable initial guesses were constructed in either *GaussView*[122] or *AGUI*[123] (for specific details, refer to the methodologies for each chapter). Following each geometry optimization, the geometric parameters and final guess were read into *Gaussian*, and a vibrational frequency analysis was performed and analyzed for imaginary frequencies, the absence of which indicates a stable minimum energy structure. All energies discussed herein are

electronic energies that have been converted from Hartrees to kilocalories per mole (kcal/mol) unless otherwise indicated, and in comparisons of various related isomers, the lowest energy isomer has been calibrated at 0 kcal/mol, with all other isomers scaled relative to the calibrated value.

Methodological Details for Chapter III

For the NiN_2S_2 and CuN_2S_2 calculations, all atoms were optimized via the use of the 6-311G(d,p) basis set[124-127] with the B3LYP functional, which combines an exchange functional, the three-parameter B3 functional of Becke[100] and a correlation functional denoted LYP,[101] named for Lee, Yang, and Parr. Because of the paramagnetic nature of the model copper complexes, an unrestricted open-shell calculation was initially performed; however, to prevent spin contamination inherent in the unrestricted open-shell calculations, restricted open-shell calculations were also investigated. Optimized bond lengths and angles in these two methods were in all cases nearly identical.

Cartesian coordinates for the starting input geometry of $Ni(ema)^{2-}$ were extracted from the crystallographic structure,[11] and the models of $Ni(emi)^{2-}$ and the copper analogues were modified by adding the gem-dimethyl groups or changing the metal center, respectively. NBO calculations were performed by reading in the optimized geometry and final guess of the $Ni(ema)^{2-}$ complex and related derivatives and utilizing the pop=NBO keyword. Cube files for the individual molecular orbitals under investigation as well as the electron density and the potential surfaces were generated in *Gaussian* and visualized by *Cerius2*.[128] Structures of the optimized geometries were

generated by *JIMP2*.[129] For each calculation in this chapter, the energies have been converted from values in Hartrees to eV.

Methodological Details for Chapter IV

Geometry and frequency calculations were performed at multiple levels of theory. Functionals utilized in this study included B3LYP,[100,101] BP86,[114,115] TPSS,[102] TPSSh,[102] M06,[130] and ωB97X-D.[116] The basis sets on the metal and ligand atoms were of varying levels of complexity, and they are designated as follows:

BS**1**) 6-311++G(d,p)[124-127]

BS**2**) Stuttgart-Dresden (SDD) effective core potential (ECP) on Fe;[131] 6-311++G(d,p) on light atoms (C,H,N, and O)

BS**3**) SDD ECP on Fe; 6-311G(d,p) on light atoms

BS**4**) 6-311++G on Fe; 6-311++G(d,p) on light atoms

BS**5**) 6-311G(d,p)

BS**6**) SDD ECP on Fe; 6-31G(d,p) on light atoms

BS**7**) SDD ECP on Fe; 6-311G on light atoms

BS**8**) SDD ECP on Fe; D95 (Dunning-Huzinaga full double-ζ) on light atoms

BS**9**) LANL2DZ (Los Alamos National Laboratory 2-double-ζ) ECP on Fe,[132] D95 on light atoms

In complexes containing sulfur atoms, the double-ζ LANL2DZ ECP or all-electron triple-ζ basis sets were used with an additional d polarization function in the former case. These basis sets will be referred to as BS$\mathbf{X}_{\mathrm{LANL}}$ and BS$\mathbf{X}_{\mathrm{POP}}$.[133]

Where possible, input geometries were extracted from crystallographic coordinates and imported into Ampac Graphical User Interface (*AGUI*)[123] as starting geometries for the optimizations. For triplet species, the optimized singlet structure was used as the starting geometry. Geometry optimizations and frequency calculations were performed using the *Gaussian 09* software suite,[120] and the frequency calculations on stable geometries had no imaginary frequencies.

Specifically, the frequency values were determined analytically via calculation of the second derivative of the energy by using the **Freq** keyword with default parameters in *Gaussian 09*.[120] Selected complexes were analyzed with a solvation model using the polarizable continuum model (PCM) parameters for tetrahydrofuran (THF) as implemented in *Gaussian 09*. *AGUI*[123] was used to extract the geometric properties and the infrared frequencies (including the vectors for stretching and bending) and to generate and render images of the frontier molecular orbitals. The 3D structures were drawn in *Cerius2*.[128]

Methodological Details for Chapter V

The *Gaussian 09* software suite[120] was utilized for optimizations of the DNICs presented herein. Wherever available, the Cartesian coordinates of the molecular structures determined by X-ray diffraction were imported into an input file and used as the preliminary structure for calculation. In complexes where no crystal structures were available, input structures were built manually in *AGUI*,[123] with all Fe-N-O bond angles set to a standardized angle of 180^0 for consistency. A frequency calculation was

performed on optimized structures to determine stability of the structure via absence of imaginary frequencies. All calculations were performed with the BP86 functional[114-115] and an SDD ECP basis set on iron[131] and 6-311++G(d,p) on all other atoms.[124-127]

Reduction potentials were calculated by determining single-point energies using the gas-phase geometries and an implicit solvation model (PCM), using parameters optimized for THF. The single-point energy of the solvated model is summed with the thermal correction of the Gibbs free energy of the gas phase structure, and this value is converted from Hartrees to eV. The value obtained from the reduced species and the oxidized species are subtracted, and this calculated value is referenced to the independently calculated reduction potential of ferrocene under identical parameters. Frequency calculations were performed analytically as implemented into *Gaussian 09*.[120] Molecular orbitals were generated and rendered by the *AGUI*[123] program, and population keywords were entered to determine the Mulliken charges, NBO charges, and percentage contributions to the molecular orbitals, using pop=full, pop=NBO, and pop=(AllOrbitals,ThreshOrbitals=1), respectively. The desired parameters were extracted from the respective output files.

Methodological Details for Chapter VI

For the Ni-Fe bimetallic complexes, computations were performed using the *Gaussian 09* software suite,[120] with the crystallographic parameters used as the starting input structure under a variety of different functional/basis set pairs. The TPSS functional[102] as well as a mixed basis set of the Stuttgart-Dresden (SDD) parameters

with an ECP on iron,[131] LANL2DZ ECP parameters unaugmented on nickel with an additional d-function on the sulfurs, and 6-311++G(d,p) for all other atoms were utilized for final optimizations, and a separate frequency calculation was performed to ascertain a stable structure with the absence of imaginary frequencies. *AGUI*[123] was used to generate molecular orbitals, and *Cerius2*[128] was used to render the overlay structure.

For the tetrameric $[(\text{Imid-R})\text{Fe}(\text{NO})_2]_4$ complexes, DFT calculations were performed at the BP86[114-115]/6-311G(d,p)[124-127] level of theory appropriate for dinitrosyl iron complexes containing N- and C-donor ligands. Calculations of complexes **1-3** focused on fundamental geometric features and orientation of the imidazolate ligands in the gas-phase computations versus that experimentally found in the solid state, and electronic features as referenced to $\nu_{(\text{NO})}$ vibrational data were also determined. Three spin states, the quintet state (one unpaired electron on each $\text{Fe}(\text{NO})_2$ unit; fully ferromagnetic), the singlet state (broken-symmetry fully antiferromagnetic, odd electron on each Fe), and the intermediary triplet state were included in the calculations.

Calculations were performed utilizing the *Gaussian 09* software suite.[120] Starting structures of both the X-ray crystallographic coordinates (for **1-3**) as well as a highly symmetric "square-like" structure (for **3** only) were employed in the optimizations. Additionally, complex **3** was calculated at the crystallographic geometry of **1** (up, up, up, up) and complex **1** was calculated at the crystallographic geometry of **3** (up, down, up down) in order to compare electronic energies of isomers. While the singlet states of tetramers **2** and **3** optimized successfully by a typical unrestricted DFT approach, the singlet state of tetramer **1** was difficult to converge, so it was optimized using an initial

guess generated by the broken-symmetry formalism described by Noodleman, *et al.*[117] and recently described for similar dimeric copper systems.[134]

In difficult to converge cases, loose SCF parameters (SCF = 10^{-4}) and smaller basis sets (6-31G) were utilized to produce a starting guess for subsequent calculations. All data presented here was terminally optimized at the BP86/6-311G(d,p) level of theory with a tight SCF convergence of 10^{-8}, except for **3"**, which was converged at 10^{-10} with an ultrafine grid. Subsequent frequency calculations were performed analytically as implemented into *Gaussian 09*.[120]

The vibrational frequencies of **1**-**3** were calculated both in the gas-phase and solution-phase using the polarizable continuum model (PCM) with CH_2Cl_2 parameters. The slight degree of asymmetry of the tetrameric units leads to multiple, near-degenerate vibrations, which have been averaged to two absorbances in order to make comparisons to the experimental data. Molecular orbitals were rendered in *AGUI* at an isosurface value of 0.03.

CHAPTER III

THEORETICAL INVESTIGATIONS OF Ni(N_2S_2) AND Cu(N_2S_2) COMPLEXES AS MIMICS FOR ACETYL COENZYME A SYNTHASE (ACS)*,‡

Background

As described in the Introduction, the understanding that metals have been found in biology to bind in tripeptide binding sites comprised of coordination environments that look relatively similar to typical inorganic ligand templates has spurred investigations and experimentation in mimicry of these sites. These tripeptides generally have a tetraanionic form (Cys-X-Cys), where X has been found as Gly in the ACS active site, described in Chapter I.[5-6] The Ni(Cys-X-Cys) complexes have features that of are importance that define them as synthetic targets for inorganic chemists. The features necessary for a successful Ni(CGC)$^{2-}$ mimic in particular are as follows: a) a coordination sphere containing contiguous nitrogen and sulfur donor atoms (S-N-N-S binding environment); b) an appropriate overall charge of the molecule; c) the presence of amido oxygens on the ligand backbone; and d) reactive thiolate sulfurs.

Predominantly, the bulk of the investigations of modeling Ni(CGC)$^{2-}$ in particular have followed as a result of a class of complexes synthesized well before the

---

structures of the ACS and NiSOD active sites were structurally characterized. This generalized class of complex is epitomized by Holm's square planar $Ni(ema)^{2-}$ complex, where ema^{4-} = *N,N'*-ethylenebis(2-mercaptoacetamide).[11] Other complexes of this general constitution utilize the ligands emi^{4-}, which is *N,N'*-ethylenebis(2-mercaptoisobutyramide) and adds steric bulk in the form of methyl groups at the carbon α to the thiolate sulfurs, and $phma^{4-}$, which is identical to ema^{4-} in every way save for a replacement of the ethylene backbone by phenylene.[11] These complexes have been utilized in the two decades since their initial synthesis to explore diverse reactivity with electrophilic reagents such as CH_3^+,[135] $(pip)_2W(CO)_4$,[23-25] and, more recently in our laboratory by Dr. Kayla N Green, O_2,[34] $[CH_2(CH_3)CH_2]^{2+}$,[34] and "$Rh(CO)_2^+$" sources.[27,28] In an effort to expand the understanding of nickel binding to N_2S_2 ligand coordination environments, the groups of Shearer,[31,32] Grapperhaus,[33] and Darensbourg,[136-137] among others, have investigated complexes with mixed amine/amido ligation in order to mimic the $Ni(CysHis^{\cdots}Cys)^-$ coordination sphere of NiSOD.

Interest in the binding of Cu^{II} in similar, i.e. N_2S_2, coordination environments is as a result of the well-studied Type 1 "blue" copper proteins.[138] Examples of Type 1, 2, and 3 copper proteins are shown in Figure III-1. In particular, Type 1 Cu proteins, despite sharing a commonality in histidine-N binding, also are prone to binding biological sulfur atoms, typically of cysteine and methionine residues. In fact, the active site of plastocyanin exhibits a $Cu^{II}N_2S_2$ binding, although it differs distinctly from NiN_2S_2 in that it coordinates in a tetrahedral geometry.[139-140] Additionally, in early active site structures of Acetyl Coenzyme A Synthase (ACS), Cu ions were found to

occupy the proximal site of the Ni_d-M_p core.[5-6,9-10] Due to the concentration of copper *in vivo*,[49] and with the knowledge that Cu has an affinity for N- and S- rich coordination environments, the natural question of how/why copper might be excluded from the distal site was explored by synthesis and spectroscopy by Dr. Kayla Green and Dr. David Rockcliffe.[30]

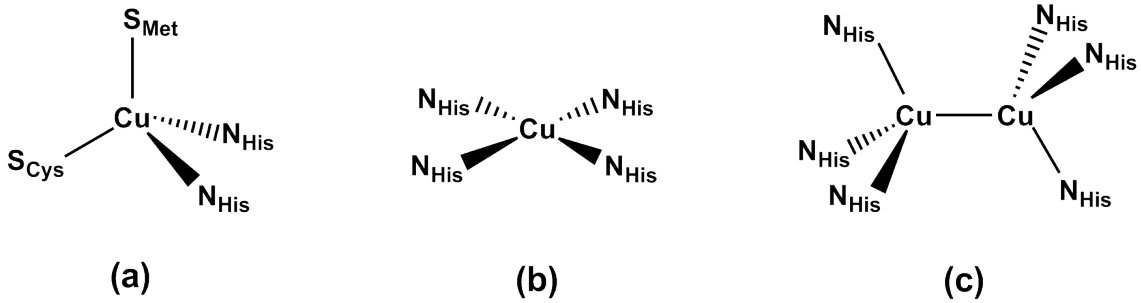

Figure III-1. Examples of Type 1, 2, and 3 copper proteins. (a) Active site of plastocyanin, (b) Cu-Zn Superoxide Dismutase, and (c) Deoxyhemocyanin.[49,138-140]

Several examples of complexes containing direct Cu-N and Cu-S ligation are shown in Figure III-2.[36,141-143] In particular, the complex shown as III-2 (b), notated $Cu(emi)^{2-}$, was synthesized by Krüger and coworkers in 1996 and demonstrated Cu in a relatively square planar $CuN_2S_2^{2-}$ environment, effectively mimicking Cu in the ACS distal site.[36] Even more extraordinarily, this complex demonstrated a mild $Cu^{III/II}$ redox potential, which led to isolation and structural characterization in both oxidation levels.

Furthermore, the complex shown as III-2 (d), which does not have sulfur ligation to the Cu center, can undergo auto-oxidation to Cu^{III} under atmospheric O_2 conditions.[143]

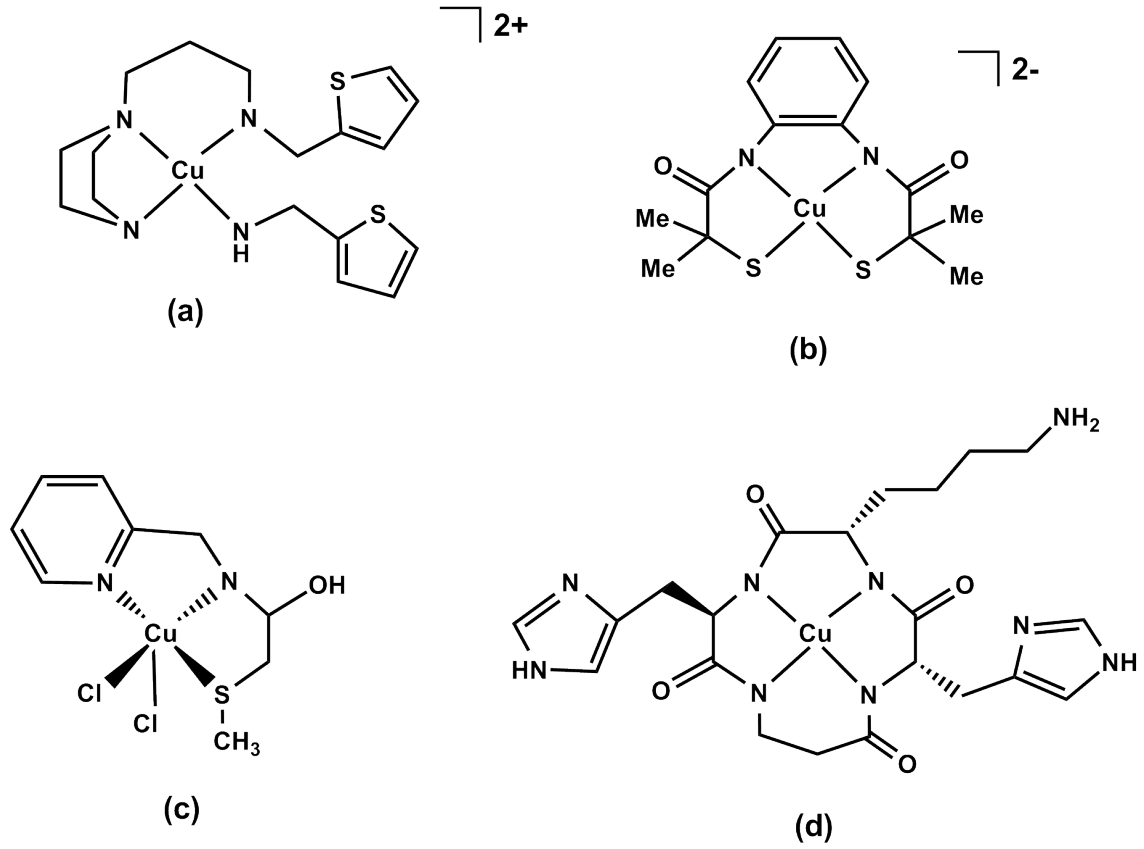

Figure III-2. Examples of copper complexes containing S- and N- ligation.[36,141-143]

To this end, the systems described above are ideal for density functional calculations, in order to determine the role of the thiolate sulfurs and to determine electronic differences between the Cu and Ni metal centers. It has been previously

demonstrated through DFT studies by Brunold, *et al.* that the M_d and S_p interactions are responsible for the nucleophilicity of the thiolate sulfurs in truncated NiSOD models as well as [Ni(dmpn)] (dmpn = N,N'-bis(2-mercaptoethyl)-1,3-propanediamine) and $[Ni(pdtc)_2]^-$ (pdtc = pyridine-2,6-bis(monothiocarboxylate)).[144] Moreover, Grapperhaus and coworkers have performed calculations on a series of square planar NiN_2S_2 complexes containing varying ligand substituents or intermolecular thiolate---H interactions in order to quantify the effect of modifying the thiolate sulfurs.[33] Comparably, the neutral $Ni(N_2S_2)$ complexes were calculated to have a HOMO containing localized $S_{thiolate}$ electron density with little metal contribution, a stark contrast to the delocalized HOMO found in $Ni(ema)^{2-}$.[145]

They concluded that the dianionic systems were more nucleophilic towards oxygen than the monoanionic analogues, and that modification of one sulfur atom decreases the nucleophilicity of the unmodified sulfur atom. That the increase in anionic charge promotes increased sulf-oxygenation has been borne by experiments by Shearer, *et al.*, in which they find that a mixed amine/amido complex undergoes sulf-oxygenation at a rate between neutral and dianionic NiN_2S_2 complexes.[31-32] We have explored in detail by density functional theory two effects: a) the overall effect of thiolate modification in a dianionic systems as it relates to geometries, electronic parameters, and bond order analyses and b) the effect of changing the central metal atom from a Ni^{II} to a Cu^{II}. These results are described below.

Computational Details of Ni and Cu (N_2S_2) Complexes and Derivatives

The gas-phase density-functional theory (DFT) computations of the $Ni(N_2S_2)^{2-}$ complexes (B3LYP functional[100-101] and 6-311G(d,p) basis set[124-127]) and of the $Cu(N_2S_2)^{2-}$ complexes (utilizing both unrestricted and restricted open shell B3LYP calculations and the 6-311G(d,p) basis set) resulted in optimized structures and metric parameters fully consistent with the crystallographic experimental results. Tables III-1 and III-2 demonstrate the effective match of experiment to computation for the alkylated and oxygenated derivatives of $Ni(ema)^{2-}$, and Figure III-3 shows the optimized structures for $M(N_2S_2)^{2-}$, where M = Ni^{II}, Cu^{II} and $N_2S_2^{2-}$ = (ema^{4-}, emi^{4-}).

Table III-1. Selected Experimental and Optimized Parameters for $Ni(ema)\bullet(CH_2)_3$

	Experimental	**Calculated**
Ni-S	2.1635(6) / 2.1628(7) Å	2.231 / 2.227
Ni-N	1.8431(15) / 1.8301 (14)	1.843 / 1.838
S-Ni-S	95.36(5) ^{o}	95.14
N-Ni-N	86.23(6)	87.01

Table III-2. Selected Experimental and Optimized Parameters for Ni(ema)•O_2^{2-}

	Experimental	**Calculated**
Ni-S(1)[a]	2.155(1) Å	2.189
Ni-S(2)	2.175(1)	2.234
Ni-N	1.863(4) / 1.859(4)	1.887 / 1.876
S(1)-O	1.427(6) / 1.445 (6)	1.506 / 1.506
S(1)-Ni-S(2)	99.27(7) °	100.82
N-Ni-N	85.45(17)	85.78

[a] S(1) refers to the oxygenated sulfur atom. S(2) refers to the unoxygenated thiolate.

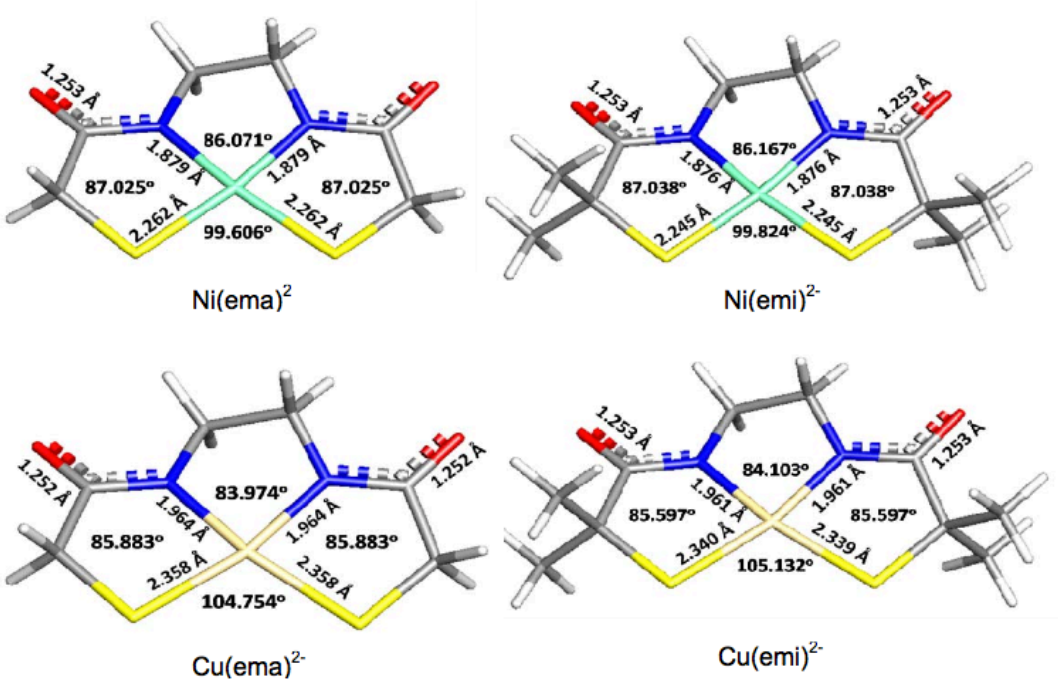

Figure III-3. Optimized Structures of $Ni(ema)^{2-}$, $Ni(emi)^{2-}$, $Cu(ema)^{2-}$, $Cu(emi)^{2-}$

The optimized structure of $Ni(emi)^{2-}$ has nearly identical geometric parameters to the $Ni(ema)^{2-}$ complex; therefore, the following discussion is appropriate to both complexes. Figure III-4 illustrates that the highest occupied molecular orbital (HOMO) and HOMO-1 are close in energy, and are composed of metal-d and sulfur-p π-antibonding interactions, involving antisymmetric and symmetric combinations of the sulfur p_z orbitals in the following linear combinations:

$$\text{HOMO-1: M } d_{yz} - (\text{S } p_z + \text{S } p_z); \text{ HOMO: M } d_{xz} - (\text{S } p_z - \text{S } p_z)$$

The slight energy difference could be explained in terms of the contribution from both the amido nitrogen and the oxygen atoms in the HOMO-1, whereas the oxygen atom interaction is absent in the HOMO.

Table III-3 gives the atomic orbital contributions to the frontier molecular orbitals for the nickel and copper complexes. In both $Ni(ema)^{2-}$ and $Ni(emi)^{2-}$, the metal contribution to the HOMO is essentially the same; however, a slight difference is observed for the sulfur contributions. The HOMO-1 of both $Ni(ema)^{2-}$ and $Ni(emi)^{2-}$ complexes is composed of Ni d_{yz} character and p_z character from each sulfur and also a symmetric combination of the nitrogen p_z orbitals. The lowest unoccupied molecular orbital (LUMO) of $Ni(emi)^{2-}$ consists of an antibonding σ-orbital set, in the *xy* plane. The HOMO−LUMO gap of $Ni(emi)^{2-}$ is calculated to be 4.20 eV, which is slightly higher than that of $Ni(ema)^{2-}$, found to be 4.12 eV.

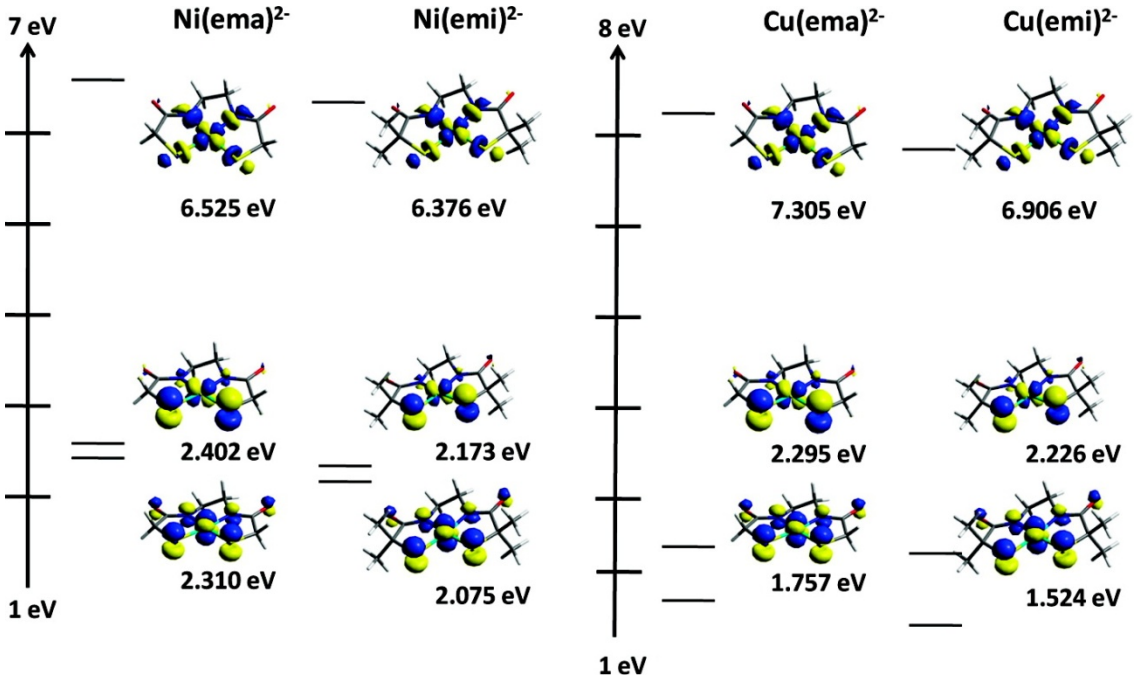

Figure III-4. Frontier molecular orbitals of $Ni(ema)^{2-}$, $Ni(emi)^{2-}$, $Cu(ema)^{2-}$, and $Cu(emi)^{2-}$. For the nickel complexes, the orbital energies descend in the order LUMO, HOMO, and HOMO-1. For the copper complexes, the orbitals descend in the order SOMO, HOMO, and HOMO-1.

The frontier orbitals of $Cu(ema)^{2-}$ and $Cu(emi)^{2-}$ share the same fundamental characteristics with differences in orbital contributions from the copper and the ligand set. The orbital composition of the singly occupied molecular orbital (SOMO), similar to that of the LUMO of the corresponding Ni complexes, involves a σ-antibonding overlap of the d_{xy} orbital of copper with the p_{σ} orbitals of sulfur and nitrogen. The HOMO has a minor (4%) copper contribution to the antisymmetric M−S d_{π}-p_{π} overlap and a thiolate sulfur contribution of 41−43% each. These orbital compositions are different for the

corresponding nickel complexes where a larger metal contribution is observed. For both Ni and Cu, the HOMO-1 is more delocalized relative to the HOMO. The HOMO-SOMO gaps of $Cu(ema)^{2-}$ and $Cu(emi)^{2-}$ are 5.01 and 4.68 eV, respectively, a trend analogous to the HOMO−LUMO gaps of the $Ni(ema)^{2-}$ and $Ni(emi)^{2-}$ complexes (*vide supra*).

Table III-3. Atomic Orbital Contributions to Calculated Frontier Molecular Orbitals

	$Ni(ema)^{2-}$	**$Ni(emi)^{2-}$**	**$Cu(ema)^{2-}$**	**$Cu(emi)^{2-}$**
LUMO/SOMO	32% Ni	29% Ni	45% Cu	43% Cu
	28% S	22% S	24% S	24% S
	12% N	12% N	18% N	18% N
HOMO	40% Ni	39% Ni	4% Cu	4% Cu
	44% S	40% S	86% S	82% S
	4% N	2% N	0% N	0% N
HOMO-1	47% Ni	43% Ni	7% Cu	7% Cu
	28% S	28% S	70% S	68% S
	8% N	8% N	8% N	8% N

The difference in metal orbital contributions to the HOMO and HOMO-1 between the nickel and copper complexes can be attributed to intrinsic metal properties, in that the bonding d orbitals of the copper(II) are stabilized in energy relative to nickel(II), while the antibonding d_{xy}, destabilized as a result of the ligand field symmetry, is indicated by the increase of copper character in the SOMO. Overall, the calculations indicate a greater degree of covalency in the metal−sulfur bond of the nickel complexes as compared to the copper most directly observed in the HOMO and HOMO-1 orbitals.

In general, computational structural parameters (described above) are corroborated by experiment. The most significant differences between the Cu and Ni complexes appear in the M−S and M−N bond lengths, as well as the S−M−S and N−M−N angles. Because of the presence of a half-populated σ* orbital, which is unpopulated in the Ni cases, bond lengths in the copper complexes are about 0.1 Å greater than those found in the analogous nickel complexes, and the S−M−S angle expands by approximately 5° for copper complexes. The distortions from planarity, as indicated by the $S_1N_1N_2S_2$ dihedral angle, are very small for the Ni complexes (3 to 4°), whereas for the Cu complexes a distortion in the form of a T_d twist is between 8.5 and 9.5°, indicating somewhat of a shift toward a pseudo-tetrahedral geometry, which is likely for a d^9 metal ion. The fact that this is not observed in the experimental structures probably reflects crystallographically imposed symmetry. Nevertheless, the amido-thiolate $N_2S_2^{4-}$ ligands are much more rigid binding sites as contrasted to the $N_2S_2^{2-}$ ligands.

The oxygenated and alkylated derivatives of $Ni(ema)^{2-}$ $[Ni(ema)\bullet O_2]^{2-}$ and $[Ni(ema)\bullet(CH_3)_2]$ and $[Ni(ema)\bullet(CH_2)_3]$ have also been investigated by density functional theory. The essential features to note in these modified complexes are in the nature of the HOMOs. In the HOMO of $Ni(ema)^{2-}$, which is described above, the interaction is a d_π-p_π antibonding orbital interaction of the central Ni atom and each thiolate sulfur. Upon oxygenation of one thiolate sulfur, the HOMO changes considerably, indicating delocalized electron density on the orbital over the unoxygenated thiolate, the nickel center, and the amido nitrogen atom trans to the unoxygenated thiolate, thus indicating effective deactivation of the oxygenated sulfur. In the corresponding alkylated complexes, in which each sulfur atom is bound to a positively charged carbon and creating an overall neutral complex; deactivation of both sulfurs is noted and found in the HOMO. In these cases, the HOMO is essentially comprised of a Ni *d* orbital and the p_z character of the amido nitrogen and backbone atoms. The percentage analysis of the FMOs of $Ni(ema)^{2-}$, $Ni(ema)\bullet O_2^{2-}$, and $Ni(ema)\bullet(R)_2$ are indicated in Table III-4.

A natural bond orbital analysis, which is a computational technique by which the principal resonance structures of a given molecule can be determined upon derivation of second-order effects, has been performed on the series of $Ni(ema)^{2-}$ derivatives due to the notable delocalization. In these studies, electronic interactions between atomic orbitals can be gauged and distinguished as covalent, dative, or non-interactions.

Table III-4. Atomic Orbital Contributions to the FMOs of Calculated Ni and Cu(ema) Derivatives

	$Ni(ema)^{2-}$	**$Ni(ema)•O_2^{2-}$**	**$Ni(ema)•(R)_2$**
HOMO	40% Ni	32% Ni	21-22% Ni
	44% S	45% S	0% S
	4% N	4% N	32-36% N
	$Cu(ema)^{2-}$	**$Cu(ema)•O_2^{2-}$**	**$Cu(ema)•(R)_2$**
SOMO	45% Cu	13% Cu	15% Cu
	24% S	42% S	25% S
	18% N	12% N	27% N

The results of this analysis on the four complexes of the series indicated an interaction between the nickel center and the thiolate sulfurs in the parent $Ni(ema)^{2-}$ complex of 1.95 e^-, indicative of a single covalent bond between each Ni-S. Accordingly, the interaction between Ni and N was determined to be 1.71 e^-, presumed to be a weaker, dative interaction between the ligand to metal. The opposite effect was observed upon the NBO analysis of the alkylated derivatives, when $Ni(ema)•(CH_3)_2$ was investigated by this technique. In this manner, the Ni-N interaction was determined to have a population of 1.93 e^-, with the corresponding Ni-S interaction having 1.72 e^-, indicative of a covalent and dative bond, respectively. That the bonding effect is reversed upon alkylation of the thiolate sulfurs is entirely consistent with the results

described above, in that this modification, analogous to biological post-translational modifications shows deactivation upon nucleophile-electrophile interactions. These effects are graphically described in Figure III-5.

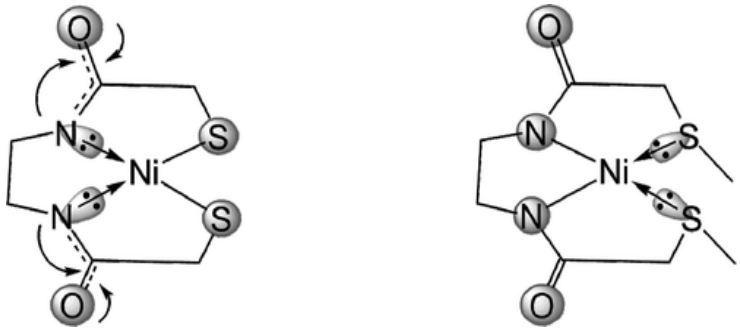

Figure III-5. Resonance NBO structures of $Ni(ema)^{2-}$ and $Ni(ema)\bullet(CH_3)_2$, where dative interactions are indicated by the arrows between atoms.

Electrostatic Potential Maps and Mulliken Charges

The electrostatic potential plots, as well as the Mulliken charges, for the $M(N_2S_2)^{2-}$ [$M = Ni^{II}$, Cu^{II}; $N_2S_2 = ema^{4-}$, emi^{4-}] series offer insight into the probable sites for charge-controlled, electrophilic and nucleophilic reactivity of the four complexes (see Figure III-6 and Table III-5). The overall charge delocalization imparted by the carboxamido unit on these dianionic NiN_2S_2 complexes as compared to the neutral NiN_2S_2 analogues was noted. The negative charge of the carboxamido group is shared between nitrogens and oxygens, creating an iminolate contribution to the metal center.

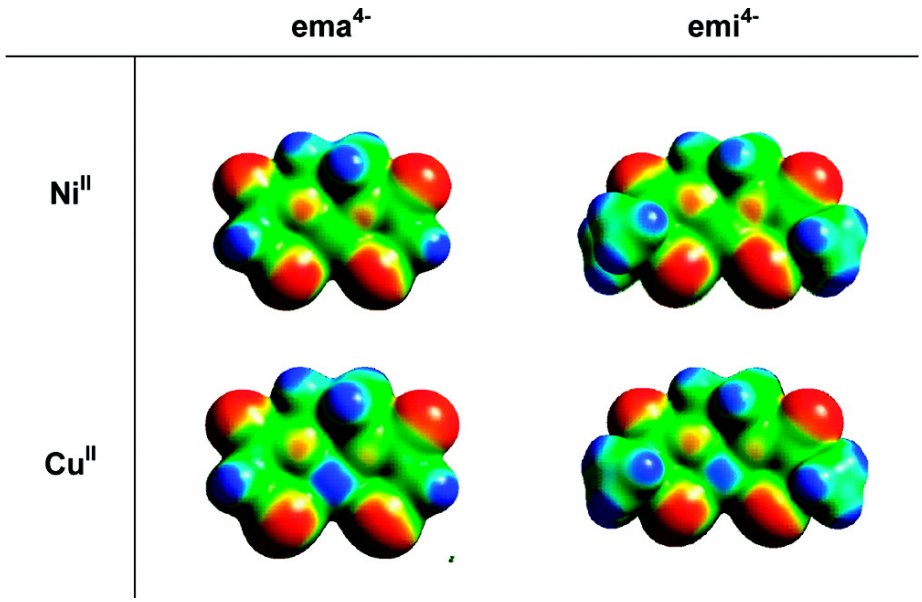

Figure III-6. Electrostatic potential maps of $Ni(ema)^{2-}$, $Ni(emi)^{2-}$, $Cu(ema)^{2-}$, and $Cu(emi)^{2-}$ plotted at an isosurface value of 0.01.

Table III-5. Mulliken Charges of M/S/N/O Atoms in the $Ni(ema)^{2-}$, $Ni(emi)^{2-}$, $Cu(ema)^{2-}$, and $Cu(emi)^{2-}$ Anions

	$Ni(ema)^{2-}$	$Ni(emi)^{2-}$	$Cu(ema)^{2-}$	$Cu(emi)^{2-}$
M	+0.871	+0.858	+1.068	+1.061
S	-0.571/-0.571	-0.509/-0.509	-0.638/-0.638	-0.584/-0.584
N	-0.630/-0.630	-0.628/-0.628	-0.676/-0.676	-0.672/-0.672
O	-0.520/-0.520	-0.512/-0.512	-0.518/-0.518	-0.511/-0.511

The $Cu(ema)^{2-}$ and $Cu(emi)^{2-}$ complexes display a greater degree of charge polarization as compared to the Ni^{II} congeners, implying that the Cu^{II} derivatives have less of a covalent interaction with the $N_2S_2^{4-}$ ligand set. This is seen by inspection of the electrostatic potential maps of Figure III-7 where there are similar areas of positive and negative character on the sulfur, nitrogen, and oxygen atoms of the $N_2S_2O_2$ backbone for all four complexes. However, a major change in these four systems is seen by the amount of positive character on the copper in $Cu(ema)^{2-}$ and $Cu(emi)^{2-}$ versus the Ni^{II} analogues, indicating the greater ionicity in the former complexes.

The Mulliken charges listed in Table III-5 for the ema^{4-} and emi^{4-} metal complexes are entirely consistent with the electrostatic potential maps, but they provide a more quantitative analysis of the charge distribution. For example, the polarization of charge in the copper systems is observed in the thiolate sulfur character which is in the range of −0.584 and −0.638 while the thiolate sulfurs of the nickel complexes are significantly more positive, −0.509 and −0.571. This corresponds to a higher positive charge on copper of about 0.20 units as compared to nickel. There are no significant differences in the negative charge of the carboxyamido oxygen atoms throughout the series of complexes (between −0.511 and −0.520, see Table III-4). For complexes containing the same metal ion, the differences in the charges of the sulfurs and the metal are small and probably insignificant.

An electrostatic potential analysis of the derivatives of the $Ni(ema)^{2-}$ complex proves to be consistent with the frontier molecular orbital and natural bond orbital analyses presented above. As can be seen in Figure III-7, the electrostatic potential of

the oxygenated Ni(ema)•O_2^{2-} complex shows striking similarity to the parent Ni(ema)$^{2-}$, although electron density originally found on the unbound thiolate in the parent shifts to the oxygenate oxygens in the derivatized complex. A modification of this kind exhibits interesting similarity to the proposed DFT complex explored by Grapperhaus, *et al.*,[33] whereby a hydrogen of one molecule is placed into close proximity to the thiolate sulfur of a NiN_2S_2 complex, causing an intermolecular interaction.

An even more drastic shift is observed upon the derivatives that have undergone alkylation, see Figure III-7. In these cases, the negative character of the thiolate sulfurs is effectively quenched, as in the potential surfaces, the alkylated region of the molecule is deep blue, indicating intense electropositivity relative to the remainder of the molecule. This can be contrasted with the parent Ni(ema)$^{2-}$, in which the electron density oriented outward from the molecule is found to be significantly more electronegative. In this way, with the supposition that the $NiN_2S_2^{2-}$ complexes are good mimics of the distal metal of the ACS active site, the role of the distal metal appears to be one of structural integrity and potential reactivity, in that the thiolate sulfurs are primed to be very reactive towards an electrophile, which in the case of the ACS active site is the proximal Ni.

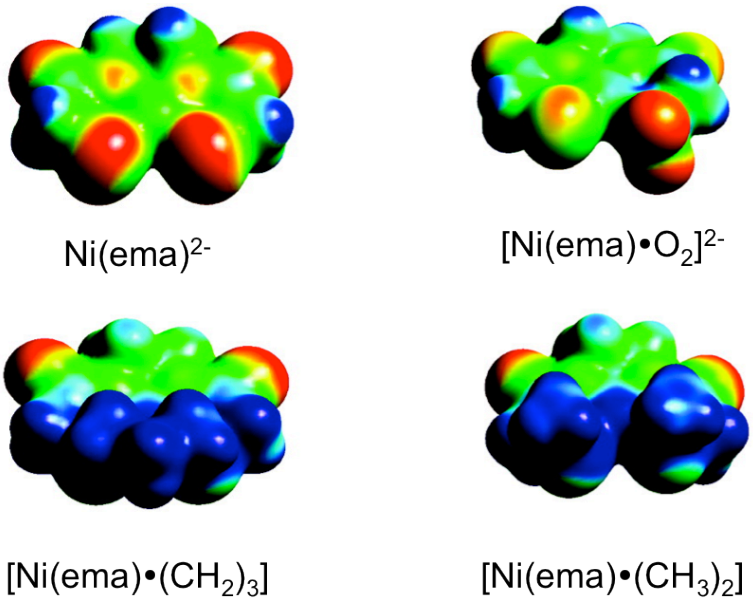

Figure III-7. Electrostatic potential maps of $Ni(ema)^{2-}$ and related derivatives. [Range is taken from 1.00 (electropositive, deep blue) to 0.33 (electronegative, bright red)]

Comments and Conclusions

The synthesis and characterization of new $CuN_2S_2^{2-}$ complexes by Dr. Kayla Green[30] has indicated that Cu^{II}, similar to Ni^{II} can occupy the rigid tetraanionic N_2S_2 coordination sites of ema^{4-}, emi^{4-}, and CGC^{4-}, despite longer M-S and M-N bonds due to the unpaired electron of Cu^{II} residing in a d_{x2-y2} orbital, which is antibonding with respect to sulfur and nitrogen. Through our computational studies it was determined that no evident steric or electronic effect excluded Cu^{II} from the distal site of Acetyl Coenzyme A Synthase. The HOMO-LUMO gaps of the $NiN_2S_2^{2-}$ complexes are around 4.1 eV, whereas the HOMO-SOMO gaps of the CuN_2S_2 complexes are on average 4.8 eV.

Electrostatic potential mapping indicates a greater covalency for the $NiN_2S_2^{2-}$ complexes and a greater ionicity for the $CuN_2S_2^{2-}$, which is borne out through the Mulliken charges and shows a greater degree of charge separation between the metal center and the coordination sphere atoms for Cu rather than Ni, although the differences are not substantial. As a result, through similarities of Ni and Cu in binding, frontier molecular orbitals, electrostatic potential mapping, and relative charge separation through population analysis, one cannot determine a physical feature responsible for exclusion of Cu in the ACS distal site. Thus, we have proposed that features of the biosynthetic pathway are likely responsible for the presence of nickel only in the distal site. The exclusion of copper must occur in upstream trafficking patterns that are as of now unknown.

In conjunction, a series of $Ni(ema)^{2-}$ derivatives that are effectively analogues of post-translationally modified Ni complexes have been calculated utilizing the same methodology. In these studies, we have concluded that there are several potential sites for electrophile binding, the N, S, and O atoms, as indicated by electrostatic potential maps. That the thiolate sulfurs should be the preferred source of electrophile interaction could not be explicitly predicted by computations alone, although the natural bond orbital analysis indicated a differing character between the Ni-N and Ni-S interactions, where in the parent complex, the sulfurs are overwhelmingly more electronegative than the nitrogen donors and show a covalent bond between Ni-S versus the dative Ni-N interaction. However, reactivity at sulfur could have been predicted *a priori* in that there have been many synthesized examples of NiN_2S_2 complexes exhibiting reactivity

through the thiolate sulfurs. Most importantly is the result that modification of the $Ni(ema)^{2-}$ at one or both of the thiolate sulfur atoms effectively deactivates the complex to further thiolate reactivity, for it has been well-established that the distal site of Acetyl Coenzyme A Synthase has thiolate sulfurs bound to the proximal nickel, which is analogous to alkylation of the model complexes. In terms of biomimicry, the $N_2S_2^{4-}$ ligand environment has served as a better mimic due to its appropriate charge, ligand architecture, and the strengthened Ni-S interaction. That it has been found to react with nucleophiles in the order $[NiN_2S_2]^{2-} > [NiN_2S_2]^{-} > [NiN_2S_2]^{0}$ has served to support this conclusion.[31-34]

CHAPTER IV

MODELING STRUCTURES AND VIBRATIONAL FREQUENCIES FOR DINITROSYL IRON COMPLEXES (DNICs) WITH DENSITY FUNCTIONAL THEORY*

Introduction

Nitrosyl chemistry has been a topic of interest for chemists for several decades, as nitric oxide (NO), released from various reagents, can have beneficial pharmacological effects.[49] However, in excess, such as an atmospheric pollutant and with subsequent oxidation to NO_2, its deleterious nature is equally well known.[48] Especially since 1990, enormous attention has been focused on the biological functions of NO such as signaling and neurotransmission,[51-53] vasodilation,[54] and immunology.[55-56] The discovery of NO bound to iron *in vivo* has led to a considerable body of work from inorganic chemists with the goal of modeling biological iron-nitrosyl complexes thereby mimicking the electronic structure and NO-release properties of these compounds.[61-68]

Biologically significant mononitrosyl iron complexes (MNICs) include the heme-based iron-nitrosyls as well as the as-isolated, inactive nitrile hydratase enzyme active site where the central Fe-NO occupies a tripeptide N_2S_2 coordination sphere.[60] Dinitrosyl iron complexes (DNICs) are known in high molecular weight forms where the

---

* Reprinted with permission from Brothers, S. M.; Darensbourg, M. Y.; Hall, M. B. *Inorg. Chem.* **2011**, *50*, 8532-8540. Copyright **2011** by American Chemical Society.

$Fe(NO)_2$ units, resulting from iron-sulfur cluster degradation, are protein bound through cysteinyl sulfurs.[64-67] The corresponding low molecular weight dinitrosyl iron complexes (LMW-DNICs), released from the protein by free cysteine, histidine or glutathione, are presumed to act as nitric oxide transport agents *in vivo*, while their protein bound precursors are expected to serve as NO storage units.[64-67] As an example, in the bis-cysteinyl $[(RS)_2Fe(NO)_2]^-$ species, the paramagnetic $[Fe(NO)_2]^+$ unit is described as the oxidized form of DNIC, and it is this form with its signature g = 2.03 EPR signal that has been targeted as a potential NO storage agent (in the high molecular weight (HMW), protein-bound form) and as a potential NO transport agent (in the LMW, protein-released form). Over the last decade a number of biomimetic DNICs have been synthesized and fully characterized, particularly by Liaw and coworkers.[64-67] A small sample of synthetic LMW-DNIC complexes with biologically relevant thiolate, carboxylate, or imidazole ligands is shown in Figure IV-1.[63,146] Additional instances of the $\{Fe(NO)_2\}$ motif are in the so-called "Roussin's red ester" complexes, which are a widely studied and well-characterized class of dimeric iron dinitrosyls bridged by sulfur atoms of the form $[(NO)_2Fe(\mu\text{-}SR)_2Fe(NO)_2]$.[68,70-79]

Transition metal nitrosyl complexes present challenging issues in the description and prediction of their electronic structure. The low-energy singly occupied π^* orbital of the NO ligand results in alternative assignments as NO^+, NO, and NO^- and correspondingly varying metal oxidation states. Enemark's and Feltham's (EF) notation $\{Fe(NO)\}^x$ avoids the oxidation state ambiguity by counting d and π^* electrons together as *x*.[44] For example, possible electronic configurations in the DNIC moiety of

$L_2Fe(NO)_2$, where the spectator ligand L = a neutral 2-electron donor ligand, may range from $[Fe^{2-}(NO^{+})_2]$ to $[Fe^{2+}(NO^{-})_2]$ with three intermediate combinations of Fe and NO redox levels between the two extremes. In the EF notation, these are all $\{Fe(NO)_2\}^{10}$. Although the EF notation avoids the oxidation state ambiguity, it hides the difficulty in describing and computing correctly the electronic structures that arise from the near degeneracy of the NO π^* and metal d orbitals.

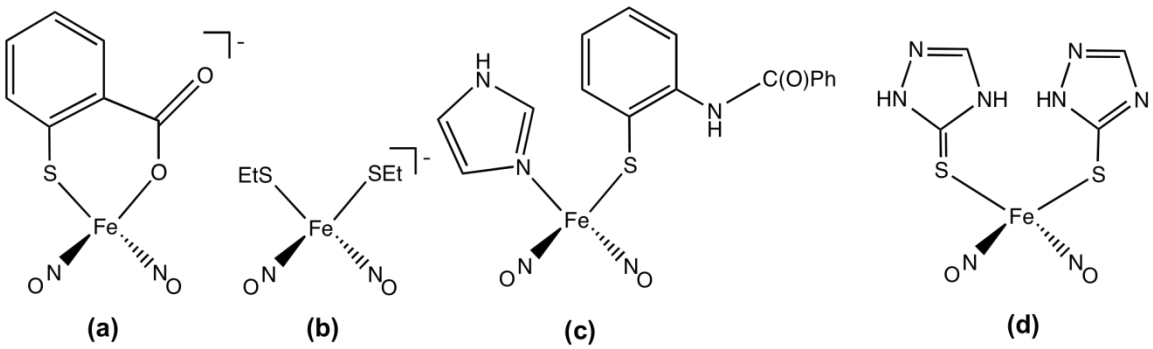

Figure IV-1. LMW-DNIC complexes containing thiolate, carboxylate, or imidazole donors.[63,146]

To address the challenges of iron nitrosyl chemistry in both molecular and electronic structures, density functional theory proves to be a powerful tool to explain chemical phenomena that may be difficult to interpret via typical spectroscopic methods alone. As succinctly discussed by Neese, *et al.*, the selection of a particular functional can be vital depending on the parameters of interest. As an example, the pure functional BP86 has been known to provide accurate geometries and frequencies but to struggle

with energetics, whereas PW91 is adept at calculation of exchange couplings.[98] Although the standard functional in inorganic and bioinorganic chemistry has been B3LYP, which is fitted with chemically derived parameters;[103] more modern functionals without chemically derived parameters such as TPSS are also finding utility.[102] In short, although in many cases a routinely chosen functional/basis-set combination may perform reasonably well, in order to understand complicated series such as iron nitrosyl complexes, it is advisable to calibrate the functional and basis set via a test set of complexes.

While there are numerous DFT studies of mononitrosyl iron complexes (MNICs),[147-150] computational explorations of DNIC-type complexes remain sparse. Early studies of DNIC complexes sought to model their geometric properties, their spin densities, and parameters derived from Mössbauer spectroscopy.[92,147-152] Specifically, some of the most extensive computational investigations of nitrosyls have been performed by Ghosh and coworkers on structures of various iron nitrosyl composition.[147-150] Through this work, they determined that for iron nitrosyl complexes, the pure functional OLYP was a better compromise for geometric and electronic properties than the hybrid functional B3LYP.[147-150] In a collaboration with Noodleman, Ghosh and coworkers performed broken-symmetry calculations on a series of mono-, bi, and tetrametallic iron complexes with varying numbers of nitrosyl ligands bound to determine spin densities and oxidation states.[149] Additionally, in work by Ye and Neese, isomer shifts, electronic characteristics, and molecular orbital diagrams of the DNIC [(Ar-nacnac)Fe$(NO)_2$] in both its neutral $\{Fe(NO)_2\}^9$ and one-electron reduced

$\{Fe(NO)_2\}^{10}$ forms were calculated and compared to experiment.[92] However, to our knowledge, no comprehensive study has been performed on the important issue of modeling the nitrosyl infrared frequencies, which are characteristic of the electronic nature of the iron dinitrosyl unit, and are important spectral signatures for both the EPR active and EPR silent states of DNICs.

In Chapter IV, the geometries and IR frequencies are calculated with various functionals and basis sets for a series of known monomeric $\{Fe(NO)_2\}^{10}$ complexes in order to determine the optimal pair. The methodology is then used to model two $\{Fe(NO)\}^7$-$\{Fe(NO)_2\}^9$ complexes previously investigated by Jaworska[151] in order to compare our selected functional/basis set pair results for the ground state, IR frequencies, and geometries. We also explore the applicability of our methodology from the reduced $\{Fe(NO)_2\}^{10}$ complexes to oxidized $\{Fe(NO)_2\}^9$. To expand the computational work on $\{Fe(NO)\}^7$-$\{Fe(NO)_2\}^9$ complexes, a newly synthesized complex, $[(NO)Fe(N_2S_2)Fe(NO)_2]^+$, where N_2S_2 = N,N'-Bis(2-mercaptoethyl)-1,4-diazacycloheptane (bme-dach) is examined.[61]

Experimental Parameters of Complexes for Calibration

Three well-characterized DNICs, $(L)(CO)Fe(NO)_2$ (L = CO, IMe, and MeImid, see figure caption for ligand description) $\{Fe(NO)_2\}^{10}$, are displayed in Figure IV-2. For complex **1**, $(CO)_2Fe(NO)_2$, the experimental infrared frequencies in tetrahydrofuran (THF) are $\nu_{(CO)}$ = 2089, 2038 cm^{-1} and $\nu_{(NO)}$ = 1808, 1762 cm^{-1}, from X-ray diffraction analysis, the average N-O bond distance is 1.171 Å. The carbonyl ligands in complex **1**

can be exchanged with ligands of varying donor strength with donor atoms = carbene-carbon, nitrogen, oxygen, sulfur, and phosphorus. Within the same redox level, exchanges with progressively stronger donor ligands lead to lower $\nu_{(CO)}$ and $\nu_{(NO)}$ values as expected by classical π-backbonding arguments.[153]

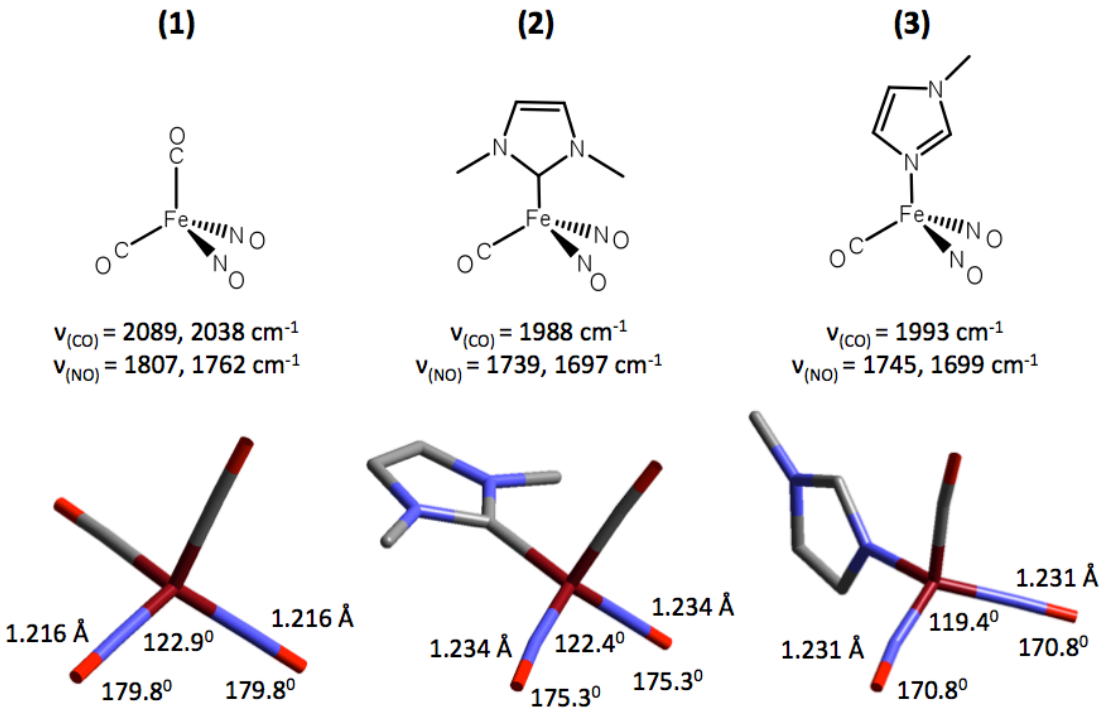

Figure IV-2. (L)(CO)Fe(NO)$_2$ series with salient geometric parameters and vibrational frequencies shown, where L = CO (**1**), IMe (N,N'-dimethyl-imidazol-2-ylidene) (**2**), and MeImid (1-methylimidazole) (**3**). [BP86/BS**2**]

For this triad of complexes, we sought to examine several variables in the computational study: (1) functional, (2) diffuse and polarization functions, (3) the effect of triple-

versus double-ζ basis sets on metal, and (4) effect of triple- versus double-ζ basis sets on ligand. The computational and experimental vibrational frequencies for complexes **1-3** can be compared in Table IV-1, and the salient geometric parameters of experiment versus selected functional/basis set pairs for complexes **1** and **2** can be compared in Table IV-2. As of yet, no crystallographic data has been reported for complex **3**.

Effect of Functionals on Vibrational Frequencies

For the six functionals investigated, three closely related pairs were found. The recently developed hybrid functionals M06 and ωB97X-D predicted the highest vibrational stretching frequencies, with the carbonyl frequencies calculated between 2000-2220 cm^{-1} and the nitrosyl frequencies between 1770-2000 cm^{-1} depending on basis set. The traditional hybrid functionals B3LYP and TPSSh were similar to each other, with both carbonyl and nitrosyl values approximately 50-60 cm^{-1} lower than the values found for M06 and ωB97X-D. Finally, the non-hybrid functionals BP86 and TPSS were again similar to each other, with carbonyl and nitrosyl values approximately 50-100 cm^{-1} lower than B3LYP and TPSSh, respectively; only geometries of **1** and **2** are compared with theory.

Table IV-1. Functional and Basis Set Vibrational Frequency Data for (L)(CO)Fe(NO)$_2$

Fe(CO)$_2$(NO)$_2$ *Experimental Values: $\nu_{(CO)}$ = 2089, 2038 cm^{-1}; $\nu_{(NO)}$ = 1807, 1762 cm^{-1}*

		BS1	$\Delta_{av.}$	BS2	$\Delta_{av.}$	BS3	$\Delta_{av.}$	BS5	$\Delta_{av.}$	BS6	$\Delta_{av.}$	BS7	$\Delta_{av.}$	BS8	$\Delta_{av.}$
B3LYP	$\nu_{(CO)}$	2142, 2097	56	2144, 2099	58	2148, 2105	63	2153, 2105	65.5	2154, 2114	70.5	2006, 1964	-78.5	2031, 1988	-54
	$\nu_{(NO)}$	1907, 1859	98.5	1907, 1856	97	1919, 1871	110.5	1927, 1879	118.5	1933, 1887	125.5	1767, 1725	-38.5	1779, 1738	-26
BP86	$\nu_{(CO)}$	2047, 1999	-40.5	2049, 2001	-38.5	2052, 2007	-34	2058, 2007	-31	2059, 2016	-26	1916, 1872	-169.5	1941, 1897	-144.5
	$\nu_{(NO)}$	1840, 1805	38	1840, 1804	37.5	1851, 1816	49	1857, 1822	55	1864, 1831	63	1704, 1674	-95.5	1716, 1685	-84
M06	$\nu_{(CO)}$	2177, 2129	89.5	2176, 2126	87.5	2181, 2133	93.5	2189, 2136	99	2176, 2131	90	2036, 1989	-51	2065, 2016	-23
	$\nu_{(NO)}$	1958, 1909	149	1959, 1911	150.5	1970, 1924	162.5	1977, 1929	168.5	1980, 1938	174.5	1822, 1783	18	1844, 1804	39.5
TPSS	$\nu_{(CO)}$	2063, 2013	-25.5	2064, 2016	-23.5	2068, 2021	-19	2073, 2021	-16.5	2074, 2030	-11.5	1930, 1885	-156	1955, 1910	-131
	$\nu_{(NO)}$	1852, 1815	49	1852, 1815	49	1862, 1827	60	1868, 1831	65	1872, 1838	70.5	1712, 1680	-88.5	1721, 1690	-79
TPSSh	$\nu_{(CO)}$	2114, 2065	26	2115, 2067	27.5	2118, 2072	31.5	2124, 2072	34.5	2124, 2080	38.5	1978, 1933	-108	2005, 1959	-81.5
	$\nu_{(NO)}$	1901, 1860	96	1902, 1859	96	1912, 1870	106.5	1917, 1875	111.5	1922, 1883	118	1760, 1724	-42.5	1769, 1733	-33.5
wB97X-D	$\nu_{(CO)}$	2198, 2152	111.5	2198, 2151	111	2202, 2157	116	2214, 2164	125.5	2204, 2161	119	2062, 2018	-23.5	2090, 2045	4
	$\nu_{(NO)}$	1963, 1907	150.5	1965, 1906	151	1978, 1922	165.5	1985, 1930	173	1989, 1937	178.5	1828, 1779	19	1843, 1794	34

(IMe)Fe(CO)(NO)$_2$ *Experimental Values: $\nu_{(CO)}$ = 1988 cm^{-1}; $\nu_{(NO)}$ = 1739, 1697 cm^{-1}*

		BS1	$\Delta_{av.}$	BS2	$\Delta_{av.}$	BS3	$\Delta_{av.}$	BS5	$\Delta_{av.}$	BS6	$\Delta_{av.}$	BS7	$\Delta_{av.}$	BS8	$\Delta_{av.}$
B3LYP	$\nu_{(CO)}$	2061	73	2064	76	2071	83	2074	86	2080	92	1929	-64	1955	-33
	$\nu_{(NO)}$	1830, 1780	87	1830, 1777	85.5	1843, 1793	100	1853, 1802	109.5	1860, 1814	119	1695, 1654	-47.5	1706, 1665	-32.5
BP86	$\nu_{(CO)}$	1966	-22	1967	-21	1973	-15	1977	-11	1982	-6	1839	-154	1865	-123
	$\nu_{(NO)}$	1770, 1734	34	1769, 1732	32.5	1782, 1745	45.5	1789, 1752	52.5	1799, 1765	64	1639, 1609	-98	1650, 1620	-83
M06	$\nu_{(CO)}$	2103	115	2100	112	2107	119	2110	122	2104	116	1957	-36	1983	-5
	$\nu_{(NO)}$	1889, 1845	148.5	1891, 1841	148	1903, 1856	161.5	1910, 1858	166	1914, 1871	174.5	1753, 1713	11	1770, 1729	31.5
TPSS	$\nu_{(CO)}$	1979	-9	1980	-8	1987	-1	1989	1	1994	6	1851	-142	1876	-112
	$\nu_{(NO)}$	1780, 1742	43	1780, 1741	42.5	1791, 1754	55.5	1799, 1759	61	1805, 1770	69.5	1645, 1614	-92.5	1654, 1622	-80

Table IV-1 continued.

TPSSh	$\nu_{(CO)}$	2031	43	2032	44	2038	50	2040	52	2045	57	1899	-94	1925	-63
	$\nu_{(NO)}$	1827, 1783	87	1829, 1783	88	1839, 1796	99.5	1847, 1802	106.5	1853, 1813	115	1690, 1655	-49.5	1698, 1662	-38
wB97X-D	$\nu_{(CO)}$	2123	135	2118	130	2125	137	2128	140	2132	144	1980	-13	2009	21
	$\nu_{(NO)}$	1889, 1830	141.5	1890, 1828	141	1903, 1845	156	1912, 1854	165	1919, 1865	174	1759, 1710	12.5	1772, 1723	29.5
Fe(MeImid)(CO)(NO)$_2$		*Experimental Values: $\nu_{(CO)}$ = 1992 cm^{-1}; $\nu_{(NO)}$ = 1744, 1698 cm^{-1}* [a]													
		BS1	**$\Delta_{av.}$**	**BS2**	**$\Delta_{av.}$**	**BS3**	**$\Delta_{av.}$**	**BS5**	**$\Delta_{av.}$**	**BS6**	**$\Delta_{av.}$**	**BS7**	**$\Delta_{av.}$**	**BS8**	**$\Delta_{av.}$**
B3LYP	$\nu_{(CO)}$	2058	66	2061	69	2069	77	2069	77	2078	86	1925	-67	1951	-41
	$\nu_{(NO)}$	1845, 1790	96.5	1844, 1787	94.5	1858, 1804	119	1866, 1813	118.5	1873, 1823	127	1710, 1664	-34	1720, 1675	-23.5
BP86	$\nu_{(CO)}$	1958	-34	1960	-32	1967	-25	1970	-22	1977	-15	1832	-160	1858	-134
	$\nu_{(NO)}$	1782, 1743	41.5	1781, 1740	39.5	1794, 1755	53.5	1800, 1762	60	1809, 1772	69.5	1652, 1619	-85.5	1661, 1628	-76.5
M06	$\nu_{(CO)}$	2097	105	2093	101	2101	109	2109	117	2101	109	1950	-42	1976	-16
	$\nu_{(NO)}$	1900, 1845	151.5	1902, 1848	154	1917, 1865	170	1925, 1871	177	1927, 1879	182	1768, 1725	25.5	1787, 1743	44
TPSS	$\nu_{(CO)}$	1971	-21	1973	-19	1980	-12	1982	-10	1989	-3	1843	-149	1868	-124
	$\nu_{(NO)}$	1791, 1751	50	1791, 1749	49	1803, 1763	62	1809, 1769	68	1816, 1778	76	1658, 1624	-80	1666, 1632	-72
TPSSh	$\nu_{(CO)}$	2024	32	2027	35	2033	41	2035	43	2041	49	1892	-100	1918	-74
	$\nu_{(NO)}$	1839, 1793	95	1840, 1791	94.5	1852, 1806	108	1857, 1811	113	1863, 1819	120	1704, 1665	-36.5	1711, 1672	-29.5
wB97X-D	$\nu_{(CO)}$	2118	126	2115	123	2122	130	2124	132	2131	139	1978	-14	2005	13
	$\nu_{(NO)}$	1903, 1839	150	1903, 1836	148.5	1918, 1855	165.5	1924, 1863	172.5	1932, 1873	181.5	1773, 1719	25	1784, 1731	36.5

[a] Values are taken from Fe(i^{Pr}Imid)(CO)(NO)$_2$

Table IV-2. Experimental versus Computational Geometric Data for (L)Fe(CO)$(NO)_2$.

$Fe(CO)_2(NO)_2$ Experimental Data: N-O_{av}: 1.171 Å; < N-M-N: 114.2^0					*$Fe(IMe)(CO)(NO)_2$ Experimental Data: N-O_{av}: 1.176(7) Å; < N-M-N: 111.3(2)^0*				
		BS1	**BS2**	**BS7**			**BS1**	**BS2**	**BS7**
B3LYP	*N-O_{av} (Å)* [a]	1.156	1.156	1.194	**B3LYP**	*N-O_{av} (Å)*	1.172	1.172	1.212
	< Fe-N-O_{av} (^{o})	178.2	178.2	179.1		*< Fe-N-O_{av} (^{o})*	174.8	174.8	177.0
	< N-Fe-N (^{o})	120.7	120.8	122.4		*< N-Fe-N (^{o})*	121.0	121.0	124.1
BP86	*N-O_{av} (Å)*	1.170	1.169	1.208	**BP86**	*N-O_{av} (Å)*	1.185	1.185	1.226
	< Fe-N-O_{av} (^{o})	178.9	178.9	179.6		*< Fe-N-O_{av} (^{o})*	174.3	174.2	176.1
	< N-Fe-N (^{o})	121.7	121.8	123.0		*< N-Fe-N (^{o})*	120.7	120.6	123.4
M06	*N-O_{av} (Å)*	1.150	1.150	1.186	**M06**	*N-O_{av} (Å)*	1.165	1.165	1.204
	< Fe-N-O_{av} (^{o})	177.9	177.7	178.7		*< Fe-N-O_{av} (^{o})*	176.8	176.5	178.2
	< N-Fe-N (^{o})	121.0	121.3	123.1		*< N-Fe-N (^{o})*	123.4	123.0	125.7
TPSS	*N-O_{av} (Å)*	1.167	1.167	1.206	**TPSS**	*N-O_{av} (Å)*	1.183	1.183	1.224
	< Fe-N-O_{av} (^{o})	178.9	178.9	179.6		*< Fe-N-O_{av} (^{o})*	175.1	174.9	176.8
	< N-Fe-N (^{o})	121.8	121.9	123.1		*< N-Fe-N (^{o})*	121.3	121.2	124.1
TPSSh	*N-O_{av} (Å)*	1.159	1.159	1.197	**TPSSh**	*N-O_{av} (Å)*	1.175	1.174	1.215
	< Fe-N-O_{av} (^{o})	178.8	178.7	179.5		*< Fe-N-O_{av} (^{o})*	175.2	175.1	177.0
	< N-Fe-N (^{o})	121.6	121.6	123.0		*< N-Fe-N (^{o})*	121.4	121.3	124.3
wB97X-D	*N-O_{av} (Å)*	1.148	1.148	1.184	**wB97X-D**	*N-O_{av} (Å)*	1.165	1.164	1.202
	< Fe-N-O_{av} (^{o})	177.7	177.4	178.3		*< Fe-N-O_{av} (^{o})*	175.4	175.0	177.4
	< N-Fe-N (^{o})	120.1	120.0	121.7		*< N-Fe-N (^{o})*	121.4	120.8	124.0

[a]The data is reported to be accurate for the N-O_{av} bond distance.

Effect of Diffuse and Polarization Functions on Vibrational Frequencies

The effect of the diffuse functions on the vibrational frequencies can be determined by comparison (Table IV-1) of BS**1**/BS**5** and BS**2**/BS**3** (diffuse/no diffuse functions). Removal of the diffuse functions from all atoms in the former and ligand atoms in the latter was probed. With the removal of diffuse functions on all atoms, the average difference in frequency between basis set pairs is approximately 10 cm^{-1} for CO stretching frequencies and approximately 20 cm^{-1} for NO stretching frequencies. In comparison, upon removal of the diffuse functions solely for the ligand atoms (BS**2** vs. BS**3**), an average shift of the CO and NO frequencies is 5 cm^{-1} and 15 cm^{-1}, indicating a metal contribution of about 5 cm^{-1}, a relatively minor effect.

The effect of elimination of polarization functions on the ligands can be evaluated by comparing basis sets BS**3** (6-311G(d,p)) and BS**7** (6-311G). Loss of the light atom *d* orbital shifted the vibrational frequencies drastically, on the order of 130 to 150 cm^{-1} for both carbonyl and nitrosyl frequencies. Conversely, upon removal of the polarization functions on the metal (BS**1** vs. BS**4**), no significant change in the calculated frequencies or bond distances is observed, indicating that the sensitivity of the frequencies to utilizing polarization functions lies predominantly on the ligand atoms rather than the metal center.

In order to determine whether the effect on polarization functions is intrinsic to the carbonyl and nitrosyl diatomic ligands or due to redistribution over the $\{Fe(NO)_2\}$ unit, the free ligands: CO, NO^+, NO, and NO^-, were calculated with basis sets BS**3** and

BS**7** and with the functionals BP86, B3LYP, and ωB97x-D, and these results are presented below.

Intrinsic Properties of Diatomic Molecules CO and NO

To separate the effect of polarization functions on the carbonyls and nitrosyls of $(L)_2Fe(NO)_2$ complexes into an intrinsic effect on the diatomic ligands or an effect involving their interaction with the Fe in the $\{Fe(NO)_2\}$ unit, free CO as well as the three oxidation states of free NO (NO^+, NO, and NO^-) were calculated with BS**3** and BS**7** (polarization functions vs. no polarization functions) with the three functionals BP86, B3LYP, and ωB97x-D. From this study, several important effects were realized:

1) The hybrid functional B3LYP most accurately calculates the bond distances of the diatomic molecules with the basis set including polarization functions (BS**3**), with BP86 slightly overestimating and ωB97x-D slightly underestimating the bond distance. With no polarization functions, all bond distances were overestimated by at least 0.015 Å.
2) However, BP86/BS**3** appears to be best for vibrational frequencies, with an error of -16 cm^{-1} for free CO and of -2 cm^{-1-} for free NO. B3LYP calculates the frequencies to be roughly 100 cm^{-1} higher for both CO and NO, while ωB97x-D calculates them roughly 130-150 cm^{-1} higher, consistent with the results from the $(L)_2Fe(NO)_2$ complexes as described above.
3) The difference in vibrational frequencies resulting from polarization functions appears to be intrinsic to the free diatomic molecules, as for the BP86 functional

between basis sets BS**3** and BS**7,** the difference is approximately 150 cm^{-1} for CO and approximately 150-180 cm^{-1} for NO and NO^-, very similar to the effect of these functions in the $\{Fe(NO)_2\}$ complexes. Interestingly, the difference for NO^+ is much higher at approximately 250 cm^{-1}, a result consistent with the expected ligand character of NO to NO^- rather than NO^+.

Effect of Triple- Versus Double-ζ Basis Sets on Metal

The effect of the size of the basis set on the metal was examined by using two different basis sets with electron core potentials on iron, the triple-ζ SDD basis set[132] and the double-ζ LANL2DZ basis set, BS**8** and BS**9**.[131] The ligand basis set was minimized to the Dunning-Huzinaga full double-ζ (D95). These results are summarized in Table IV-1. The difference between the two basis sets on the iron atom resulted in small differences in the CO frequencies (on average, ~ 1-5 cm^{-1}) with a greater difference in the NO frequencies (~ 5-10 cm^{-1}), although the values are on par with or less than prior modifications, *vide supra*. Clearly the nitrosyl frequencies were more sensitive in their response to changes in the iron basis set, affirming an effect, albeit minor, resulting from delocalization of electron density on the $\{Fe(NO)_2\}$ unit.

Effect of Triple- Versus Double-ζ Basis Sets on Ligand

In a similar fashion, changes due to the basis set of the ligands were queried systematically through comparisons of double- and triple-ζ basis sets. In these experiments, the SDD ECP was used as the standard basis set for iron, with the various

ligand basis sets. The basis sets selected for comparison were BS**3** (6-311G(d,p)) / BS**6** (6-31G(d,p)) and BS**7** (6-311G) / BS**8** (D95). In accordance with a change from a larger (triple-ζ) to a smaller (double-ζ) basis set, the nitrosyl frequencies shift by 15 cm^{-1}, while the carbonyl frequencies shift less systematically (negligible for BS**3**/BS**5** and 25 cm^{-1} for BS**6**/BS**7**).

Overall Commentary on Methodology

With respect to the nitrosyl stretching frequencies, the variables discussed above can be ranked as:

Polarization functions on the ligand (~150 cm^{-1}) >

Functional (60-120 cm^{-1}) >

Basis set of ligand (triple- vs. double-ζ) (15 cm^{-1}) ~ Diffuse functions on ligand (15 cm^{-1}) >

Basis set of metal (triple- vs. double-ζ) (5-10 cm^{-1}) >

Diffuse functions on metal (5 cm^{-1})

Polarization functions on metal (0-5 cm^{-1}).

An ideal functional/basis set pair should be that which provides a simultaneously close match to the experimental complex geometry and the carbonyl and nitrosyl vibrational frequencies, while the complexity of the functional and size of the basis set are balanced between suitable results and computational cost.

One consequence of this study indicates that the basis set on the ligand atoms has far more influence on diatomic ligand vibrational frequency values than does the iron

basis set. As expected, the calculated frequencies and bond distances are related as shown in Figure IV-3. Comparison of the various functionals show that the best functional for the average $\nu_{(NO)}$ is BP86. In this figure, it can be seen that a majority of the functionals achieve similar differences between the symmetric and the antisymmetric stretches of the dinitrosyls. Somewhat surprisingly, the new functionals M06 and ωB97X-D, thought to circumvent issues and improve results relative to classic functionals, perform the worst of the selected functionals due to a systematic underestimation of backbonding, reflected in shorter N-O bond distances and higher $\nu_{(NO)}$ values. It is worthwhile to note that in Figure IV-4, where the BP86 functional is used to compare to experiment by virtue of the eight basis sets, the best match is with BS**1** and BS**2**, with BS**2** somewhat lower in computational cost due to the ECP on the metal.

Summarily, the best compromise between qualitative and quantitative results in both calculated vibrational stretching frequencies and N-O bond distances is found with BP86/BS**2** (although TPSS/BS**2** is quite similar). Interestingly, calculation of the vibrational frequencies using a PCM solvation model for THF at the BP86/BS**2** level of theory demonstrates a shift of both carbonyl frequencies (from 2049/2001 cm^{-1} in gas-phase to 2037/1973 cm^{-1} for **1**) and nitrosyl frequencies (from 1840/1804 cm^{-1} to 1809/1755 cm^{-1} for **1**), with a larger effect on the latter values. The Mulliken charges between the gas-phase and solvation calculations indicate no significant charge redistribution. Due to these results, BP86 will be used further as the functional of choice.

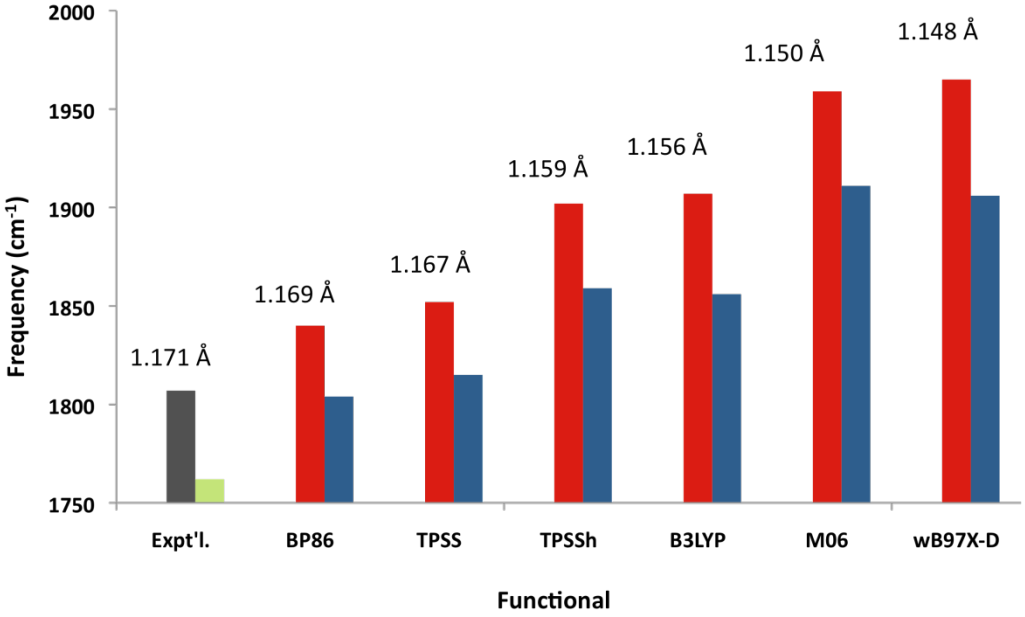

Figure IV-3. Frequency vs. Functional/Experiment of $(CO)_2Fe(NO)_2$ using BS**2**. The average N-O bond distance is listed above the bars. The red bars represent the values for the symmetric stretch and blue bars represent the antisymmetric stretch. (Gray and green bars are given for experimental values)

Computational Investigation of $\{Fe(NO)\}^7$-$\{Fe(NO)_2\}^9$ Coupled Systems

A series of $[(NO)Fe(L)Fe(NO)_2]^n$ (n = -1, 0, +1) complexes are shown in Figure IV-5, and we utilized our methodology to model these with BP86/BS**2** combinations. In this study, for all figures and tables, Fe' refers to the mononitrosyl iron and Fe" refers to the dinitrosyl iron.

Complex **4**, synthesized by Liaw and coworkers, was found to be diamagnetic.[154] Despite the similarities of the diamond shaped Fe_2S_2 core of **4** and **5**, complex **5** demonstrates quite different vibrational frequencies, a longer Fe-Fe distance

(2.669 Å for **4** vs. 2.766 Å for **5**), and a magnetic moment of μ_{eff} = 2.81 μ_B, signifying a triplet ground state.[155] The geometric and spectroscopic properties are summarized in Table IV-3.

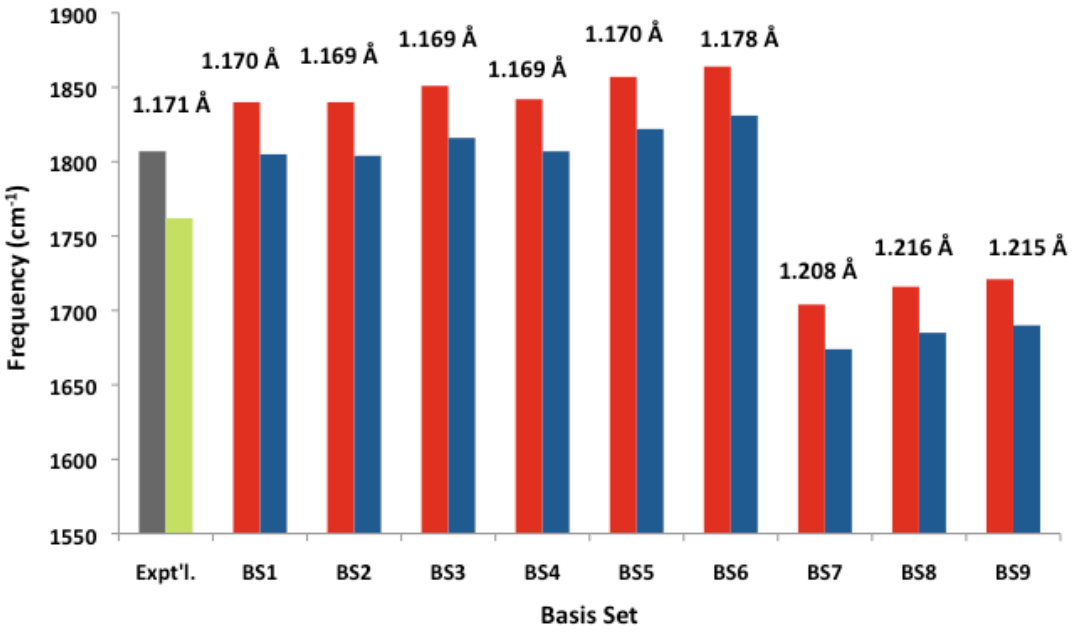

Figure IV-4. Frequency vs. Basis Set/Experiment of $(CO)_2Fe(NO)_2$ using BP86. The average N-O bond distance is listed above the bars. The red bars represent the values for the symmetric stretch and blue bars represent the antisymmetric stretch. (Gray and green bars are given for experimental values)

In previous computational investigations of **4** and **5,** the B3LYP/6-311G* functional/basis set pair (in our notation, B3LYP/BS**3**) was used to optimize the geometry and to determine the magnetic coupling,[151] and in a second study of complex

5, broken-symmetry calculations were used to model the Mössbauer parameters.[147-150] Jaworska examined the natural orbitals of **4** and **5** and found antiferromagnetic coupling in the [(NO)Fe(μ-S)$_2$Fe(NO)$_2$] core in each case.[151]

Complex **6** has been recently synthesized in our laboratory. Rather than the diamond-shaped Fe_2S_2 core found in **4** and **5**, the complex adopts a butterfly-shaped core with an Fe-Fe distance of 2.786 Å.[61] This observed difference in geometry is likely related to the increase in the vibrational stretching frequencies of the dinitrosyl unit compared to those of **4** and **5**, with the mononitrosyl vibrational energy between that of the symmetric and antisymmetric stretch, see Table IV-3.

In an effort to integrate complex **6** with **4** and **5** as a related series and to serve as a test set for our methodology described above, we used the calibrated functional/basis sets (BP86/BS**2**$_{\mathbf{LANL}}$; BP86/BS**2**$_{\mathbf{POP}}$) to model the vibrational frequencies and optimized geometries of the bimetallics. Salient computational values are presented alongside the experimental in Table IV-3.

Computational Exploration of [(NO)Fe(μ-S)$_2$Fe(NO)$_2$] Complexes 4, 5, and 6

The crystallographic structures of complexes **4**, **5**, and **6**, were utilized as the starting structures for the full optimizations at the BP86/BS**2**$_{\mathbf{LANL}}$ level of theory. Both the singlet and triplet state of this series of complexes were calculated, and in nearly all instances, the optimized geometry of the appropriate ground state structure matched reasonably well with the crystallographic parameters. One notable exception was in the triplet state of complex **5**. When optimized starting from the singlet geometry, the triplet

optimized with a linear NO and large Fe-Fe distance in contrast to the experimental results. In a second optimization the Fe'-N-O angle was initially frozen at the experimental value and the geometry allowed to relax. The new starting structure was fully optimized to a triplet-state geometry, which corresponds well to the crystallographic data. The three optimized structures are shown in Figure IV-5, and the geometric and vibrational frequency values can be compared in Table IV-3. The degree of coupling between the $\{Fe'(NO)\}^7$ and $\{Fe''(NO)_2\}^9$ units is illustrated in Figure IV-6 where the normal coordinates are shown. For each structure, the contribution of each oscillator is shown in both magnitude and direction.

Consistent with the experimental NMR data,[154] Complex **4** was predicted to be a singlet, with the triplet state nearly 15 kcal/mol higher in energy. The vibrational frequencies for both $\mathbf{4}_{sing.}$ and $\mathbf{4}_{trip.}$ match extremely well with $\mathbf{4}_{exp.}$. Likewise, the Fe'-N-O angle and N-O distance were relatively independent of these states. Thus, by any of these measurements, it was futile to identify the ground state. However, the predicted Fe'-Fe" distance expands from 2.649 Å in the singlet to 3.003 Å in the triplet and the former corresponds well with the experiment. Additionally, the Fe-(μ-S) distances match extremely well in the singlet geometry but are overestimated by nearly 0.1-0.2 Å in the triplet, corresponding to an average error of approximately 5%.

Table IV-3. Experimental and Computational Parameters for $\{Fe(NO)\}^7$-$\{Fe(NO)_2\}^9$ Complexes. (Data in italics represents the Fe'NO data)

	Functional/ Basis Set	Total Energy (kcal/mol)	$\nu_{(NO)}$ (cm^{-1})	Fe-N-O	N-O	Fe'-Fe''	Fe'-S	Fe'-(μ-S)	Fe''-(μ-S)
$[(NO)Fe(S_4)Fe(NO)_2]^-$ (4)									
Experimental			*1766*, 1746, 1719	172.2, 169.2, *178.2*	1.168, 1.167, *1.167*	2.669	2.293, 2.300	2.235, 2.247	2.286, 2.302
Calculated (S=0)	BP86/BS2$_{LANL}$	0	*1784*, 1759, 1724	168.0, 168.0, *180.0*	1.187, 1.187, *1.181*	2.649	2.335, 2.335	2.233, 2.233	2.307, 2.307
	BP86/BS2$_{POP}$	0	*1784*, 1758, 1723	167.7, 167.7, *180.0*	1.187, 1.187, *1.181*	2.656	2.334, 2.334	2.235, 2.235	2.307, 2.307
Calculated (S=1)	BP86/BS2$_{LANL}$	14.64	*1777*, 1740, 1726	167.9, 167.8, *175.2*	1.186, 1.186, *1.179*	3.003	2.355, 2.261	2.401, 2.320	2.340, 2.341
	BP86/BS2$_{POP}$	14.29	*1776*, 1738, 1724	167.8, 167.3, *174.9*	1.186, 1.186, *1.179*	3.011	2.352, 2.264	2.398, 2.319	2.340, 2.341
$[(NO)Fe(NS_3)Fe(NO)_2]$ (5)									
Experimental[a]			1789, 1736, *1654*	161.6, 173.3, *145.3* 170.1, 173.3, *151.8*	1.130, 1.158, *1.160* 1.230, 1.158, *1.150*	2.766	2.231	2.309, 2.355	2.298, 2.291
Calculated (S=0)	BP86/BS2$_{LANL}$	7.52	1829, 1777, *1739*	164.4, 174.1, *175.7*	1.179, 1.187, *1.171*	2.627	2.348	2.246, 2.232	2.265, 2.300
	BP86/BS2$_{POP}$	7.82	1831, 1776, *1738*	164.1, 174.0, *175.6*	1.179, 1.187, *1.170*	2.629	2.346	2.251, 2.234	2.269, 2.301
Calculated (S=1), bent Fe^1NO	BP86/BS2$_{LANL}$	0	1797, 1751, *1719*	164.5, 171.7, *151.8*	1.176, 1.183, *1.178*	2.758	2.239	2.329, 2.365	2.296, 2.298
	BP86/BS2$_{POP}$	0	1797, 1750, *1720*	164.4, 171.2, *151.9*	1.178, 1.183, *1.178*	2.765	2.241	2.329, 2.364	2.299, 2.300
$[(NO)Fe(N_2S_2)Fe(NO)_2]$ (6)									
Experimental			1795, *1763*, 1740	174.4, 166.6, *165.8*	1.170, 1.170, *1.147*	2.786	---	2.244, 2.259	2.252, 2.247
Calculated (S=0)	BP86/BS2$_{LANL}$	0	1849, *1803*, 1756	179.0, 161.2, *163.3*	1.166, 1.180, *1.171*	2.688	---	2.253, 2.253	2.236, 2.235
	BP86/BS2$_{POP}$	0	1849, *1803*, 1756	178.7, 161.0, *163.5*	1.166, 1.180, *1.171*	2.692	---	2.255, 2.255	2.238, 2.238
Calculated (S=1)	BP86/BS2$_{LANL}$	5.32	1839, *1780*, 1763	169.6, 169.4, *154.1*	1.166, 1.177, *1.172*	2.978	---	2.293, 2.293	2.319, 2.319
	BP86/BS2$_{POP}$	5.01	1838, *1779*, 1764	169.3, 168.9, *154.2*	1.166, 1.177, *1.172*	2.982	---	2.295, 2.295	2.321, 2.320

[a]The structure is reported to be disordered; both sets of data are shown.

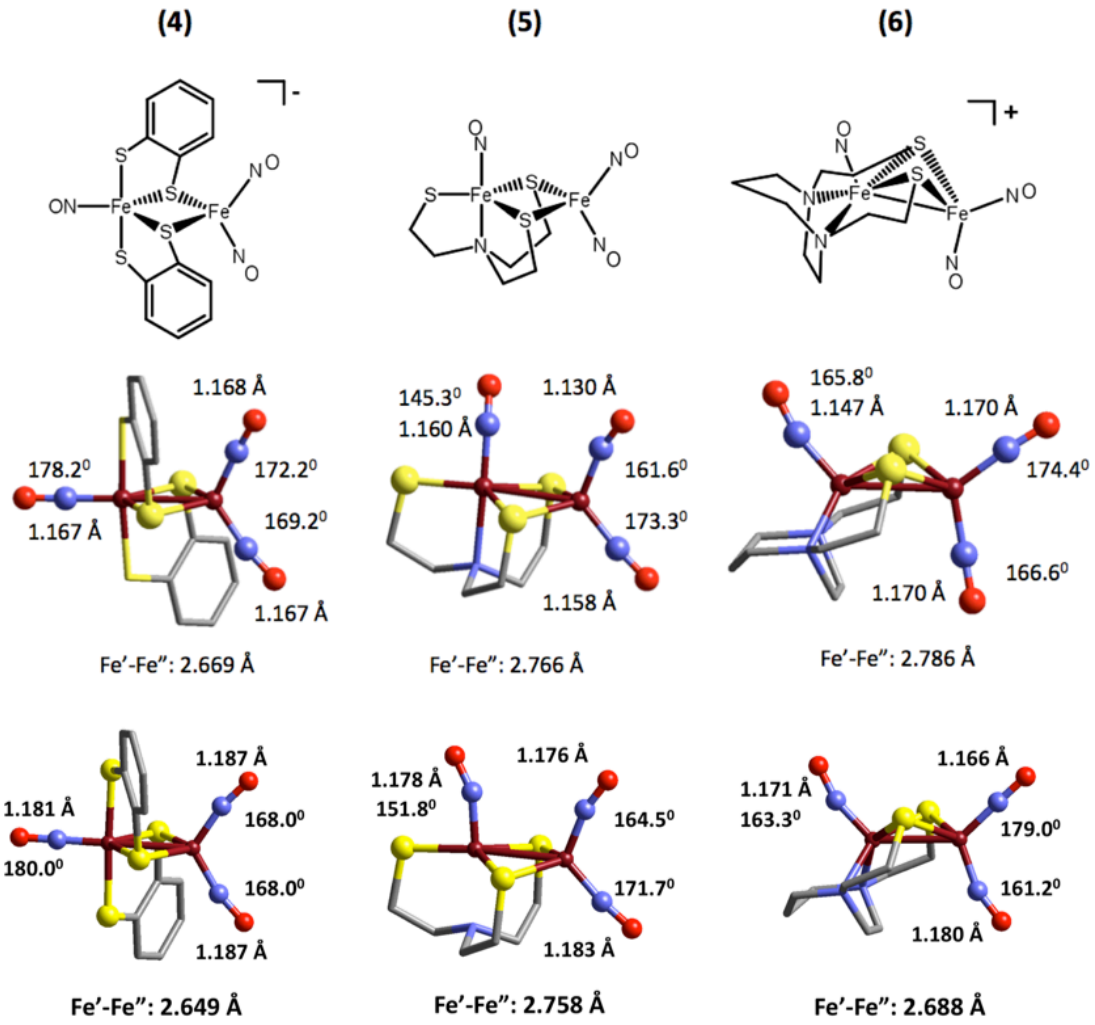

Figure IV-5. (from left to right) Experimental (top) and computational ground state (bottom) structures of $[(NO)Fe(S_4)Fe(NO)_2]^-$ (**4**)[154] , $[(NO)Fe(NS_3)Fe(NO)_2]$ (**5**)[155], and $[(NO)Fe(N_2S_2)Fe(NO)_2]$ (**6**)[61]. Fe'-Fe" and N-O bond distances are given in addition to < Fe-N-O, and the $[(NO)Fe(\mu\text{-}S)_2Fe(NO)_2]$ core is represented as ball and stick drawings.

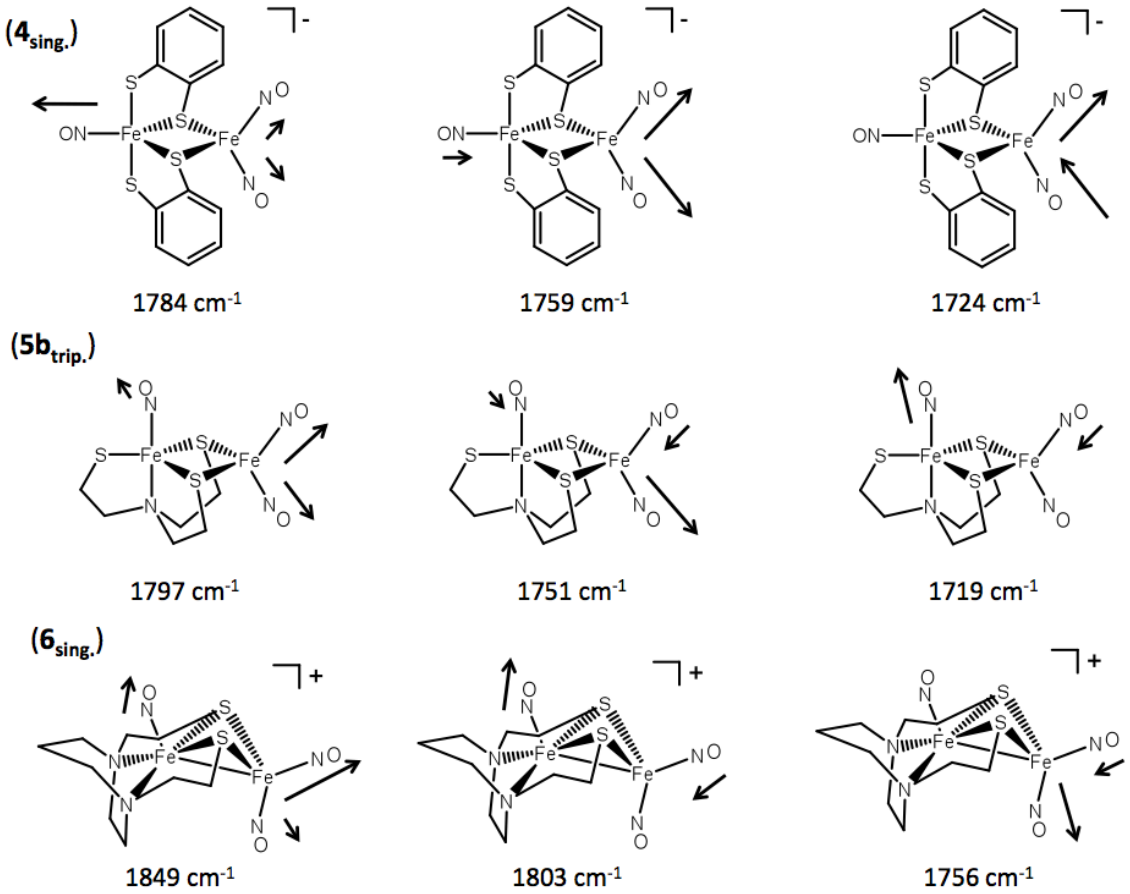

Figure IV-6. Vibrational coupling for the nitrosyl frequencies in the ground state structures of **4**, **5**, and **6**. Values listed correspond to BP86/BS**2**. The vibrational frequency represented is identified below the structures. The largest arrow represents the strongest nitrosyl stretch, and smaller stretches and contractions are represented by smaller arrows, and the length of the arrows is roughly drawn to scale.

Complex **5**, which has been recently investigated by both Jaworska[151] and Ghosh and coworkers,[148-149] has been reoptimized with our parameters. Three distinct isomers were found on the potential energy surface as follows: singlet state with a linear Fe'-N-O, triplet state with a linear Fe'-N-O, and a triplet state with a bent Fe'-N-O, the last of

which is consistent with the crystallographic structure. The ground state was found to be the bent Fe'NO triplet structure, with the linear triplet 4.42 kcal/mol and the linear singlet 7.52 kcal/mol higher in energy. The crystallographic structure was reported to possess disorder in the Fe'NO and Fe"NO nitrosyl oxygen atoms positioned *cisoid* to one another, with two Fe'-N-O angles extracted from the data at $145.3/151.8^0$ and the Fe"-N-O angle at $170.1/173.3^0$. The difficulty in accurate refinement of M-N-O complexes with nitrogen and sulfur based ligand sets has been previously noted.[41] Interestingly, the calculated Fe'-N-O angle for BP86 matched identically with the latter experimental value. The Fe'-Fe" distance was calculated to be 2.758 Å, close to the experimental value of 2.766 Å.

Finally, the frequencies of the lowest energy structure were calculated to be 1797, 1751, and 1719 cm^{-1} with the experimental values reported at 1789, 1736, and 1654 cm^{-1}. Thus, the two higher energy stretches match reasonably well, with a larger error in the lowest energy stretch. The assignment of the vibrational stretches, though, is determined to be appropriate with the visualization of the infrared frequencies identifying the lowest energy stretch as Fe'-N-O, consistent with the results by Hughes and coworkers.[155] Other salient geometric values, as well as those utilizing an alternate functional (TPSS) or basis set (BS$\mathbf{2_{LANL}}$)**,** can be observed in Table IV-3.

Extension of Methodology to Complex 6

From its sharp NMR features, the butterfly-shaped complex **6** is proposed to exist as a ground-state singlet.[61] With respect to the nature of the trinitrosyl butterfly complex,

we sought to use our computational methodology to identify the ground state. Like complex **4,** which indicated a clear preference for the singlet state, $\mathbf{6}_{trip}$ was calculated to be only 5.32 kcal/mol (BP86) higher than $\mathbf{6}_{sing}$. The experimental assignment of the infrared data of **6**, in which the highest and lowest nitrosyl stretching frequencies are assigned to the $\{Fe(NO)_2\}^9$ and the middle nitrosyl frequency is assigned to the $\{Fe(NO)\}^7$ is confirmed upon examination of the spectral pattern and visualization of the normal infrared coordinates in the theoretical calculation.

Despite the better match of both the N-O and Fe-S bond distances for $\mathbf{6}_{sing}$ than for $\mathbf{6}_{trip}$, in both cases the Fe'-Fe" distance (exp. 2.786 Å) is calculated too short in the singlet case (2.688 Å) and too long in the triplet case (2.978 Å). To alleviate concerns that the butterfly-shaped Fe_2S_2 core was not calculated with the same degree of accuracy as the diamond-shaped complexes due to a poor basis set on sulfur, all complexes were recalculated using the all-electron 6-311++G(d,p) basis set on sulfur. The results are found in Table 1 and show no significant difference in the computational values, with experimental vs. computational differences of the vibrational frequencies on the same magnitude of error relative to the test set, indicating that larger molecules, such as those containing sulfur atoms, do not reflect sensitivity to the effects listed above. Thus, we assign the ground state structure to be a diamagnetic singlet by virtue of energy, the vibrational frequencies, and the correspondence of geometric parameters to those of experimental values.

Summary and Comments

Examinations of various functionals and basis sets for the prediction of geometries and NO stretching frequencies in a series of $Fe(NO)_2$ complexes led to the following conclusions relative between functional/basis set pairs: a) the polarization functions on the ligand atoms are essential, contributing 150 cm^{-1} for $\nu_{(NO)}$; b) diffuse functions on the ligand account for 15 cm^{-1}; c) diffuse functions on the metal account for about 5 cm^{-1}; and d) the differences between a double- and triple-ζ basis sets account for approximately 15 cm^{-1} on the ligand and less than 10 cm^{-1} for the metal. The functionals utilized in this work provide a range with a maximum difference of 120 cm^{-1}. In this manner, we discovered that the best compromise between basis set size, quality of results and cost was BP86/BS**2** with TPSS/BS**2** a close second choice, whereas newer functionals such as M06 and ωB97x-D systematically underestimate the degree of backbonding, resulting in too short N-O bond distances and extremely high vibrational frequencies with better basis sets. Additionally, it is observed for the $(L)Fe(NO)_2(CO)$ complexes that NO is more sensitive to L both experimentally and theoretically than is CO, as a larger change in nitrosyl than carbonyl frequencies is seen for both the exchange of the ligand L and changes in the functional/basis set.

By utilizing our methodology, three known complexes containing a $\{Fe'(NO)\}^7$-$\{Fe''(NO)_2\}^9$ unit with a Fe_2S_2 bridging moiety and disparate geometries on the $\{Fe'(NO)\}^7$ fragment were calculated. Our computations confirmed that Complex **4** is a singlet and Complex **5** is a triplet, as has been concluded from experimental results, with improved computational agreement in the case of Complex **5**. Utilizing our

methodology, we were able to mimic both the values of the frequencies as well as the assignments of the experimental stretches, with an extension to the newly synthesized Complex **6**, which was calculated to have a singlet ground state with a low energy triplet state. This methodology is expected to have general utility for other $\{Fe(NO)_2\}$ applications.

CHAPTER V

TOWARDS UNDERSTANDING THE RESPONSE OF THE $Fe(NO)_2$ UNIT TO "SPECTATOR" LIGANDS IN DINITROSYL IRON COMPLEXES*

Background

Delocalization between the valence orbitals of iron and nitrosyl as ligand renders oxidation state assignments equivocal even in such a simple case as the mononitrosyl iron Fe(NO) unit, within a dianionic porphyrin ligand setting where alternate possibilities (neglecting the possible spin state ambiguities) exist as follows:

a) $Fe^{I}(NO^{+})$ b) $Fe^{II}(NO^{\bullet})$ c) $Fe^{III}(NO^{-})$

Recent studies, especially in the computational community, have led to the accepted description of nonheme mononitrosyl complexes as the latter case, i.e., Fe^{III} antiferromagnetically coupled to a triplet NO^{-}.[149-150,156-157] As a valuable aid for practical electron counting, the well known Enemark-Feltham approach sums electrons in valence orbitals of Fe^{n+} and NO and thus accepts the "non-innocent" nature of the NO ligand when bound to iron by ignoring specific assignments.[44] For interpretation of spectroscopies that might reflect physical and reactivity properties, however, a more explicit description of electron distribution is desired. This issue becomes critical in the dinitrosyl iron complexes (DNICs) where oxidized $\{Fe(NO)_2\}^9$ and reduced

* This chapter is to be submitted for review and publication with the following authorship list: Scott M. Brothers, Jennifer L. Hess, Chung-Hung Hsieh, Michael B. Hall, and Marcetta Y. Darensbourg.

$\{Fe(NO)_2\}^{10}$ electronic configurations are known, sometimes isolated as stable complexes in the presence of the same ligand.[81,89-91] For example, the bidentate β-diketimate ligand is found in $[(Ar\text{-}nacnac)Fe(NO)_2]^-$ and in $[(Ar\text{-}nacnac)Fe(NO)_2]^0$, with electronic assignments of $\{Fe(NO)_2\}^{10}$ and $\{Fe(NO)_2\}^9$, respectively. These complexes were isolated and structurally characterized by Lippard, *et al.*, finding small changes in Fe-N distances, and also minimal changes in Mössbauer parameters.[90-91] A computational study by Ye and Neese concluded that even though the redox processes were metal based, increased π-backbonding in the reduced level over the oxidized level led to similar overall charge on iron, accounting for the small difference in isomer shifts in the Mossbauer spectrum.[92] These configurations are known to exhibit different reactivity relative to NO release, in that the oxidized $\{Fe(NO)_2\}^9$ DNIC is more NO-labile than is the reduced $\{Fe(NO)_2\}^{10}$ form.[61,89]

We have recently reported a series of DNICs that made use of N-heterocyclic carbenes as neutral ligands that stabilize the two redox levels of DNICs as described above for the anionic nacnac ligand. With sterically bulky substituents on the nitrogens of the NHCs, stable trinitrosyl iron complexes have been isolated.[61,89] In addition, the steric and electronic nature of NHCs make them suitable as mimics for imidazoles or histidines as donor ligands, as histidines are likely of import to biological DNICs, in protonated or deprotonated forms. The NHC-DNICs are of significance as models. Representative complexes of this series can be found in Figure V-1.

In this chapter we report the DFT optimizations of structure and molecular orbital/electronic configuration conclusions in DNIC redox partners in order to explore

the effect of ligand on ease of interconversions, vibrational spectroscopic signatures, and electrochemical parameters. This effort expands on the work of Ye and Neese.[92] Our computations use the BP86 functional and a mixed basis set of SDD parameters with an effective core pseudopotential on the iron centers and 6-311++G(d,p) on all other atoms, a combination that was optimized for reference to structural and vibrational spectroscopic data, which was reported in the previous chapter.[158] In this way, a series of 16 DNICs shown in Figure V-1 containing biologically and semi-biologically relevant ancillary ligands over an expansive range of the spectrochemical series are examined in both oxidized and reduced form.

The Broken-Symmetry Approach to Dinitrosyl Iron Chemistry

In systems in which the electronic state is difficult to define adequately due to non-innocence or extensive delocalization, density functional theory calculations are often utilized to attempt to differentiate multiple low-energy excited states as a result of various ferro- or antiferromagnetic coupling. To this end, a methodology referred to as the "broken-symmetry" approach and pioneered by Noodleman and coworkers[117] on investigations of iron-sulfur clusters has been developed. In this approach, a local density functional approximation is used in order to provide the calculation a wave function whereby electrons are localized in opposite spins, such as assigning a spin-up S = 5/2 state to one iron of the iron-sulfur cluster and a spin-down S = 5/2 state to another.[118] This methodology avoids issues of highly delocalized or coupled systems whereby the pure wavefunction generally has multiconfiguration character, in which the

determination of appropriate energetics and spin states of individual atoms or ligands is challenging to deconvolute.[118]

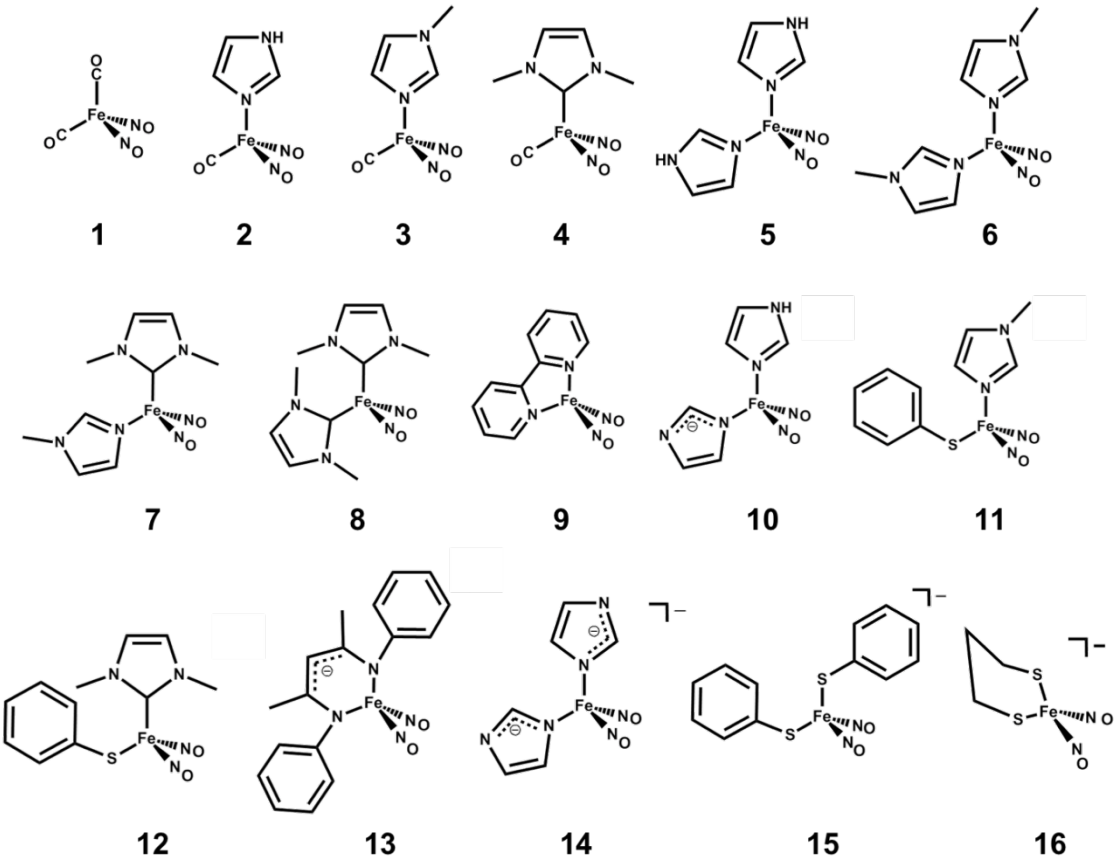

Figure V-1. 16 DNIC complexes under investigation, with the most common $\{Fe(NO)_2\}$ oxidation state shown: **1-9**, $\{Fe(NO)_2\}^{10}$ and **10-16**, $\{Fe(NO)_2\}^{9}$. Complexes **1-9** have been calculated as neutral and cationic, **10-13** have been calculated as monoanionic and neutral, and **14-16** have been calculated as dianionic and monoanionic.

An application of the broken-symmetry approach has been to diagnose the proper electronic state of a variety of DNICs. This technique has been widely employed by Ghosh, *et al.*, in a series of publications describing both mononitrosyl and dinitrosyl iron complexes, such as Roussin's red salts $[Fe_2(NO)_4(\mu\text{-}S)_2]^{2-}$, Roussin's black salt $[Fe_4(NO)_7(\mu_3\text{-}S)_3]^-$, heme-nitrosyl complexes, and a number of others.[147-150,156] The typical broken-symmetry methodology is to calculate the fully ferromagnetically coupled geometry. For example, in a "reduced" $\{Fe(NO)_2\}^{10}$ complex containing neutral ancillary ligands, the complex could be considered $Fe^{II}(NO^-)_2$, which would have 6 *d* electrons, and 4 π^* electrons; thus, the complex would be optimized with 8 unpaired electrons, i.e., fully ferromagnetic. Subsequently, the orbitals and geometry of the ferromagnetic guess can be imported into the calculation, and the α and β spins of the electrons of the ligands and metal can be explicitly assigned prior to optimization, and the desired antiferromagnetic guess can be computed.[149]

For example, in the exploration of an iron dinitrosyl complex containing a truncated β-diketimate ligand, Ye and Neese evaluated the electronic structure of the $\{Fe(NO)_2\}^9$ and $\{Fe(NO)_2\}^{10}$ forms of the complex by using a terminology given as BS(X,Y), where X is the total number of unpaired electrons on the metal center and Y is the total number of unpaired electrons summed over the two nitrosyl ligands.[92] More specifically, BS(5,4) indicates $S_{Fe} = 5/2$ antiferromagnetically coupled to each nitrosyl as a triplet with $S_{NO} = 1$. In this way, the oxidized complex was calculated with the electronic states BS(5,4), BS(4,3), BS(3,2), BS(2,1), and BS(1,0). For the reduced complex the electronic states BS(4,4), BS(3,3), BS(2,2) and BS(1,1) were calculated and

the energies compared. In their analysis, the oxidized complex was determined to be a mixture of the BS(5,4) and BS(4,3) electronic states, and the reduced complex was determined to be purely BS(4,4). Through the data obtained through this approach, the difference in geometric and Mössbauer data was rationalized, i.e., which was as a result of increased π-backbonding from the iron into the NO ligands of the reduced species, *vide supra*.[92]

Effects on Structural Parameters and Degree of Backbonding of Ligand Replacement

In order to delineate effects of ancillary ligands on the electronically ambiguous $\{Fe(NO)_2\}^x$ (x = 9,10) unit often found in the pseudo-tetrahedral $(L)(L')Fe(NO)_2$ composition, a series of biologically or quasi-biologically relevant C, N, or S-donor ligands embodying a broad scope of the spectrochemical range was investigated, as listed in Figure V-1.

Table V-1 lists calculated metric parameters for five of the above complexes representative of a variety of ligand types within known DNICs. For the sake of clarity, only this series is reported; however, the conclusions given are relevant to the full scope of the complexes. Complexes **1**, **4**, and **8** have been isolated and characterized in reduced $\{Fe(NO)_2\}^{10}$ form;[83,89] $\mathbf{8}^+$, **12** and **15** are known in the oxidized $\{Fe(NO)_2\}^9$ form.[89] The other redox partners either have not been isolated or are observed as transient intermediates if at all. Inspection of the data in Table V-1 leads to the following primary conclusions:

Table V-1. Computational Geometric and Frontier Molecular Orbital Data for a Series of (L)(L')$Fe(NO)_2$ Complexes.

		N-O_{av} (Å)	Fe-N_{av} (Å)	Fe-N-O_{av} (°)	N_{NO}-Fe-N_{NO} (°)	L-Fe-L (°)	Fe-L_{av} (Å)	HOMO/SOMO Fe_d Character[a]	HOMO/SOMO NO_p Character[a]
$(CO)_2Fe(NO)_2$ (1)	$\{Fe(NO)_2\}^{10}$	1.169	1.667	178.90	121.83	99.42	1.817	32%	46%
$(CO)_2Fe(NO)_2^+$ (1^+)	$\{Fe(NO)_2\}^{9}$	1.147	1.691	169.61	115.80	121.61	1.945	52% (α) / 47% (β)	14% (α) / 38% (β)
(NHC-Me)(CO)$Fe(NO)_2$ (4)	$\{Fe(NO)_2\}^{10}$	1.185	1.656	174.22	120.59	98.17	1.880	45%	21%
(NHC-Me)(CO)$Fe(NO)_2^+$ (4^+)	$\{Fe(NO)_2\}^{9}$	1.161	1.676	170.44	116.44	107.51	1.933	29% (α) / 27% (β)	12% (α) / 42% (β)
$(NHC\text{-}Me)_2Fe(NO)_2$ (8)	$\{Fe(NO)_2\}^{10}$	1.201	1.648	175.70	123.77	101.27	1.949	53%	12%
$(NHC\text{-}Me)_2Fe(NO)_2^+$ (8^+)	$\{Fe(NO)_2\}^{9}$	1.175	1.662	168.29	115.54	115.48	2.018	40% (α) / 32% (β)	12% (α) / 38% (β)
(NHC-Me)(SPh)$Fe(NO)_2^-$ (12^-)	$\{Fe(NO)_2\}^{10}$	1.209	1.644	168.82	119.71	100.45	2.137	45%	12%
(NHC-Me)(SPh)$Fe(NO)_2$ (12)	$\{Fe(NO)_2\}^{9}$	1.184	1.656	170.90	119.06	119.06	2.123	23% (α) / 21% (β)	5% (α) / 28% (β)
$(SPh)_2Fe(NO)_2^{2-}$ (15^{2-})	$\{Fe(NO)_2\}^{10}$	1.217	1.635	168.12	115.12	91.81	2.374	61%	4%
$(SPh)_2Fe(NO)_2^-$ (15^-)	$\{Fe(NO)_2\}^{9}$	1.191	1.654	167.17	116.30	103.99	2.304	23% (α) / 6% (β)	0% (α) / 18% (β)

[a] Data reported for the restricted, closed-shell calculations in the $\{Fe(NO)_2\}^{10}$ reduced complexes.

1) Oxidation of any given reduced $\{Fe(NO)_2\}^{10}$ monometallic complex leads to a decrease in the average N-O bond distance with a concomitant increase in the average Fe-N bond distance, consistent with less Fe to NO backbonding in the oxidized $\{Fe(NO)_2\}^9$ form.

2) As expected, the replacement of an electron-withdrawing ancillary ligand such as CO for a σ-donor such as NHC-R or π-donor such as SR^- causes more backbonding to NO in either redox level, evident in the longer N-O bond distances and lower $\nu_{(NO)}$ frequencies.

3) With less steric bulk on the ancillary ligands (i.e. L, L' = CO, NHC-Me), the N_{NO}-Fe-N_{NO} angle responds to oxidation by contraction by ca. $5\text{-}8^0$, whereas with L, L' = SPh^-, this angle is constant. In contrast, the L-Fe-L' angle is extremely responsive (covering a range of $91\text{-}122^0$) to redox level change in all ancillary ligands.

4) The Fe-L_{av} distance is in all cases in Table V-1, and in most cases over the explored series of data, an indicator as to the more stable redox level within a given $\{Fe(NO)_2\}^{10}/\{Fe(NO)_2\}^9$ pair. For example, the shorter Fe-L_{av} distance is 1.817 Å for **1** and 1.945 Å for $\mathbf{1}^+$. By comparison, the values for $\mathbf{15}^{2-}$ and $\mathbf{15}^-$ are 2.374 and 2.304 Å, respectively, consistent with a stable $\{Fe(NO)_2\}^{10}$ in **1** and $\{Fe(NO)_2\}^9$ in $\mathbf{15}^-$.

5) With stronger electron-donating ancillary ligands, more backbonding into the nitrosyl unit is responsible for less NO_p character in the

frontier molecular orbitals with a concomitant increase in the Fe_d character (and, if the energy is appropriately matched, an increase in the ancillary ligand character).

Molecular Orbital and Population Analyses

In order to attempt to quantify the electronic effects of ligand substitution via replacement of ligands with those in our chosen spectrochemical series, the frontier molecular orbitals and percent contributions (given in Table V-1) as well as a ground state population analysis was performed. Figure V-2 provides sketches of the highest occupied molecular orbitals for several of the complexes of Table V-1 in reduced and oxidized forms. Additionally, Table V-2 reports the NBO population analysis data for the complexes reported in this series.

Table V-2. Natural Electronic Configurations and NBO Natural Charges for Selected Complexes.

Complex	Natural Electron Configuration			NBO Natural Charges					
	4s	3d	4p	Fe	N_1	N_2	O_1	O_2	Σ[Fe(NO)$_2$]
1	0.40	7.49	1.19	-1.095	0.366	0.366	-0.144	-0.144	-0.651
1$^+$	0.42	7.20	0.95	-0.574	0.381	0.381	0.001	0.002	0.191
4	0.38	7.41	1.12	-0.901	0.325	0.321	-0.244	-0.245	-0.744
4$^+$	0.40	7.18	0.99	-0.566	0.354	0.354	-0.101	-0.101	-0.060
8	0.36	7.33	1.04	-0.760	0.269	0.271	-0.292	-0.289	-0.801
8$^+$	0.37	7.07	0.93	-0.381	0.298	0.298	-0.154	-0.154	-0.093
9	0.01	7.17	0.76	-0.273	0.240	0.257	-0.235	-0.239	-0.250
9$^+$	0.30	6.92	0.66	0.112	0.266	0.266	-0.101	-0.101	0.442
12$^-$	0.37	7.29	1.04	-0.706	0.261	0.236	-0.331	-0.336	-0.876
12	0.38	7.16	1.01	-0.569	0.301	0.289	-0.210	-0.220	-0.409
13$^-$	0.01	7.16	0.46	-0.268	0.223	0.200	-0.341	-0.318	-0.504
13	0.31	6.95	0.73	0.001	0.259	0.249	-0.210	-0.197	0.102
15^{2-}	0.02	7.24	1.00	-0.668	0.236	0.228	-0.369	-0.367	-0.940
15$^-$	0.40	7.10	1.00	-0.514	0.278	0.275	-0.255	-0.249	-0.465
16^{2-}	0.05	7.21	0.38	-0.653	0.216	0.201	-0.403	-0.411	-1.050
16$^-$	0.40	7.09	1.00	-0.517	0.257	0.258	-0.280	-0.287	-0.569

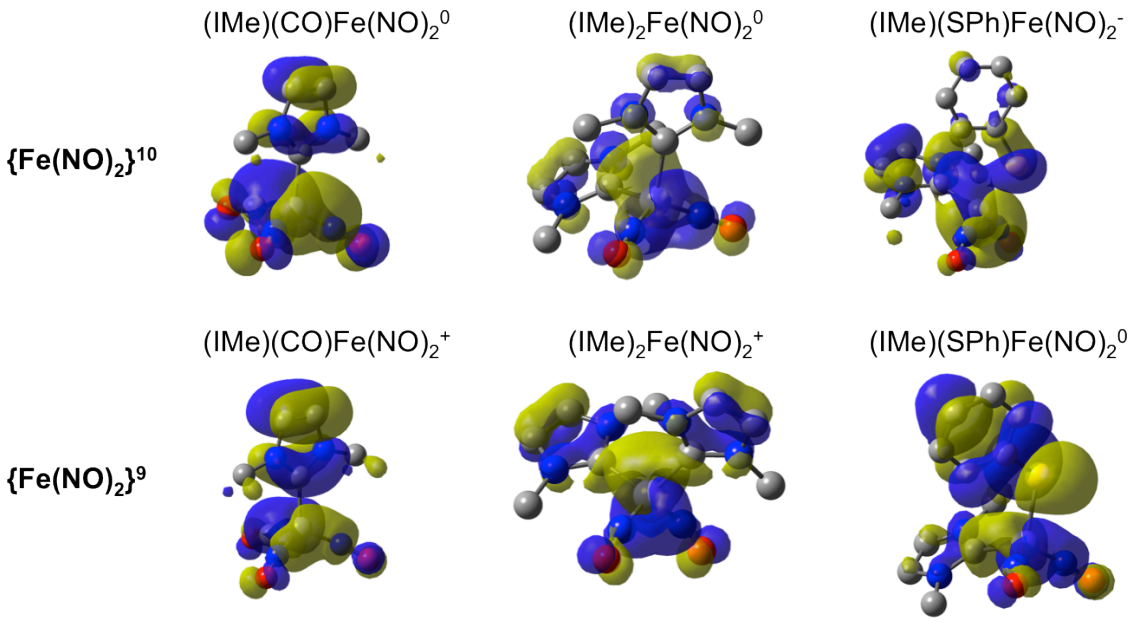

Figure V-2. HOMO of **4**, **8**, and **12**$^{-}$, and α-SOMO of **4**$^{+}$, **8**$^{+}$, and **12**.

Through this study, it was determined that subsequent ligand substitutions by stronger electronic donors cause a pronounced shift in the overall ground state population as well as the percentage electronic character in the highest occupied frontier molecular orbitals, HOMO for $\{Fe(NO)_2\}^{10}$ or SOMO for $\{Fe(NO)_2\}^{9}$. In the case of the $\{Fe(NO)_2\}^{10}$ reduced forms of the complexes shown above, the change between **4**, **8**, and **12**$^{-}$ is the most telling. As stronger donors replace the ancillary ligands, the natural charge of the iron atom becomes more positive, with the overall natural charge of the iron dinitrosyl unit exhibiting a more negative character. This is indicative that stronger electron donors induce an effect whereby the nitrosyl ligands bear a greater amount of

the negative charge, consistent with increased backbonding, described above. In other words, NO draws electron density away, very effectively skipping over the Fe.

In the case of the oxidized $\{Fe(NO)_2\}^9$ complexes $\mathbf{4}^+$, $\mathbf{8}^+$, and **12**, the effect is less clear. In this situation, oxidation from $\{Fe(NO)_2\}^{10}$ to $\{Fe(NO)_2\}^9$ exhibits both a more positive charge on the Fe center as well as the total $\{Fe(NO)_2\}$ unit, as would be expected in light of an oxidation. Furthermore, the natural charge of the $\{Fe(NO)_2\}$ unit again displays a more negative natural charge by replacement of stronger donating ligands, again reasonably consistent with a backbonding argument. That which is unclear is in the character of the thiolate ligand in the oxidized complex $(IMe)(SPh)Fe(NO)_2$. In the SOMO of the complex, it can be seen that SPh^- ligand bears a significant amount of the electronic character of the complex, which is not noted for the HOMO of the analogous reduced complex. The unusual characteristic of this complex, which is biologically relevant, could have relevance to NO storage or release mechanisms *in vivo*, which is a topic for future exploration.

Effects of Ligand Replacement on Vibrational Frequencies and Electrochemical Potentials

To date, electrochemical investigations of iron dinitrosyl complexes have been sparse.[81,83,85,88-89,91] Of the complexes approaching the solvent windows of the electrochemically accessible potentials of typical organic solvents, only one stable redox level is known. For example, the paradigm for the $\{Fe(NO)_2\}^{10}$ motif, $(CO)_2Fe(NO)_2$ (**1**) (calculated $E_{1/2}$ = +1.44 V) has been identified in its oxidized state $(CO)_2Fe(NO)_2^+$

(**1**$^{+}$) by infrared spectroscopy and utilized as a transient source of $\{Fe(NO)_2\}^9$ in ligand substitution reactions.[83] In contrast, the well-characterized complex $(SPh)_2Fe(NO)_2^-$ (**15**$^-$) (calculated $E_{1/2}$ = -2.36 V) is exclusively reported as the $\{Fe(NO)_2\}^9$ form and used as a starting material or derived from cleavage of Roussin's red ester (RRE) complexes. To our knowledge, neither of the aforementioned complexes has been electrochemically analyzed.

In the complexes that have been experimental analyzed by electrochemical techniques and found to have an accessible $\{Fe(NO)_2\}^{9/10}$ reduction potential, the values fall within a broad range (~ -1.5 V to +0.5 V) owing to the electron donating ability of the ancillary ligands or the overall charge of the complex.[81,83,85,88-89,91] In several cases, such as L,L'= PPh_3 or $OPPh_3$ (experimental $E_{1/2}$ = -0.59 V to 0.37 V)[81] and a bidentate β-diketimate ligand L,L' = Ar-nacnac (complex **13** in this study, experimental $E_{1/2}$ = -1.34 V),[90,91] both the oxidized and reduced forms of the $[(L)(L')Fe(NO)_2]$ complex have been isolated and crystallographically defined.

In order to better understand the differences between the oxidized and reduced forms of the dinitrosyl complexes with a broad variety of ligands, the infrared frequencies were calculated utilizing the previously reported methodology (Chapter IV), and the electrochemical reduction potentials were also calculated; these results are summarized in Table V-3. Figure V-3 reports the comparison of the calculated average $\nu_{(NO)}$ versus the experimental $\nu_{(NO)}$ values for either $\{Fe(NO)_2\}^9$ or $\{Fe(NO)_2\}^{10}$, whichever is appropriate to compare to experiment. In both cases the match is quite good, with the R^2 values for each set of data greater than 98%. It should be noted that

the data point for **14**$^{-}$ has been excluded, as in the crystal structure the [Na-18-crown-6-ether]$^{+}$ cation forms a tight ion pair with an imidazolate anion, affecting the value of the nitrosyl stretching frequencies versus that of the calculated gas phase values. From these data, several effects are pronounced:

1) The calculated frequencies are responsive to the overall charge of the complex, in that calculations of $\{Fe(NO)_2\}^{10}$ complexes are on average 30-50 cm^{-1} higher than the experimental counterparts, whereas $\{Fe(NO)_2\}^{9}$ complexes are calculated ca. 0-20 cm^{-1} higher than experiment, leading to the sharper slope for $\{Fe(NO)_2\}^{9}$ in Figure V-3.
2) Oxidation of the reduced form of a complex, as evidenced by **8**/**8**$^{+}$ and **13**$^{-}$/**13** in Table V-2, leads to a positive shift in experimental frequencies of about 120-140 cm^{-1} (computationally: 100 cm^{-1}), consistent with the backbonding argument described above.
3) Replacement of an electron-withdrawing carbonyl ligand by either a neutral imidazole or N-heterocyclic carbene ligand accounts for a negative shift of approximately -60 cm^{-1} in the average $\nu_{(NO)}$ value in the same redox level. Replacement of the σ-donating imidazole or NHC by a π-donating thiolate affects a -50 cm^{-1} shift in the same redox level, indicating that the magnitude of frequency shift of substitution of two ligands of a complex is on par with oxidation.

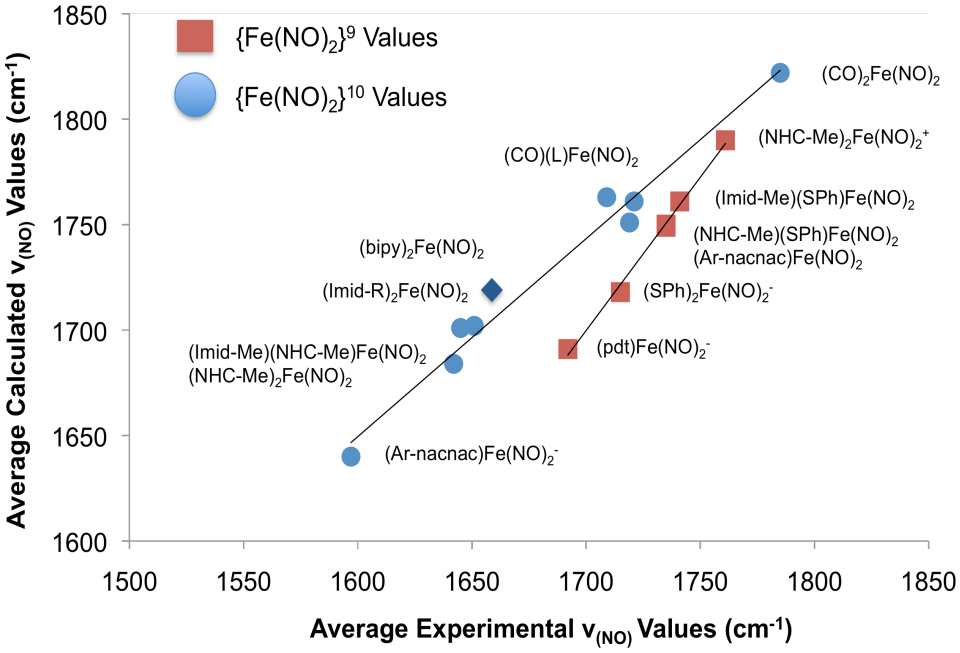

Figure V-3. Calculated versus experimental values of nitrosyl frequencies ($\nu_{(NO)}$)

Also reported in Table V-3 are the calculated $E_{1/2}$ values for the 16 complexes analyzed in the scope of this study. Additionally, experimental electrochemical data is presented for complexes **4**, **8**, **9**, **12**, and **13**.[85,89,91] Upon a cursory inspection of the data presented, several effects are immediately evident. In complexes containing carbonyl ligands, the experimental $E_{1/2}$ values are unknown, or in the case of **4**, ill-defined, as the value given is the E_{pc} for the irreversible oxidation rather than the $E_{1/2}$. It is presumed that oxidation of the carbonyl-containing iron dinitrosyl complexes leads to loss of CO, responsible for the transient nature of $(CO)_2Fe(NO)_2^+$, *vide supra*.

As a general trend, replacement of carbonyl by ligands throughout the spectrochemical series (in this work: Imid-R, NHC-R, SR^-) leads to a systematic shift in reduction potential, from +1.44 V in $(CO)_2Fe(NO)_2$ to -2.36 V in $(SPh)_2Fe(NO)_2^-$ with the intermediate case of $(NHC\text{-}Me)_2Fe(NO)_2$ at -0.82 V. Figure V-4 graphically describes the comparison of both experimental and computational reduction potentials versus average nitrosyl frequency in their $\{Fe(NO)_2\}^{10}$ reduced forms. The reduction potentials versus $\{Fe(NO)_2\}^9$ average nitrosyl frequencies are found to exhibit an identical trend and are not shown here. That the reduction correlate well with the infrared frequencies is interesting, and indicates that the reduction potential is related to the degree of backbonding in the iron dinitrosyl unit.

By comparison of the few experimental electrochemical potentials versus the calculated data, there is found to be a substantial correlation. The values determined differ by a minimum of 20 mV in the intermediary cases, with the experimental $E_{1/2}$ for **8** and **9** at -0.77 V and -0.48 V, respectively and the corresponding computational $E_{1/2}$ values at -0.82 V and -0.46 V. In the case of the neutral to anionic reduction such as those exhibited by complexes **12** and **13**, a greater difference was found between computation and experiment of -1.76 V vs. -1.33 V in **12** and -1.70 V vs. -1.34 V in **13**, although the trend is consistent. It is interesting to note that while the ligands in **12** and **13** are quite different, both the vibrational frequencies and electrochemical potentials are nearly identical in both experiment and computation, indicating that in systems of more anionic charge, it is likely that the charge rather than the nature of the ancillary ligands accounts for the spectroscopic and electrochemical characteristics.

On the most negative extreme of the calculated $E_{1/2}$ values lies the complexes that would have to undergo reduction from a monoanionic $\{Fe(NO)_2\}^9$ species to a dianionic $\{Fe(NO)\}^{10}$ species, with L,L' = $Imid^-$, SPh^-, or the bidentate propanedithiolate ligand (pdt^{2-}), with calculated values determined beyond -2 V. To our knowledge, none of these complexes have been reduced experimentally, probably owing to the very negative reduction potential. Nevertheless, recently a $[(L)(L')Fe(NO)_2]^{1-/2-}$ (L,L' = (SC_7H_4SN) or (OC_7H_4SN)) reduction was reported to occur at surprisingly mild potentials of -0.94 V and -1.17 V.[88]

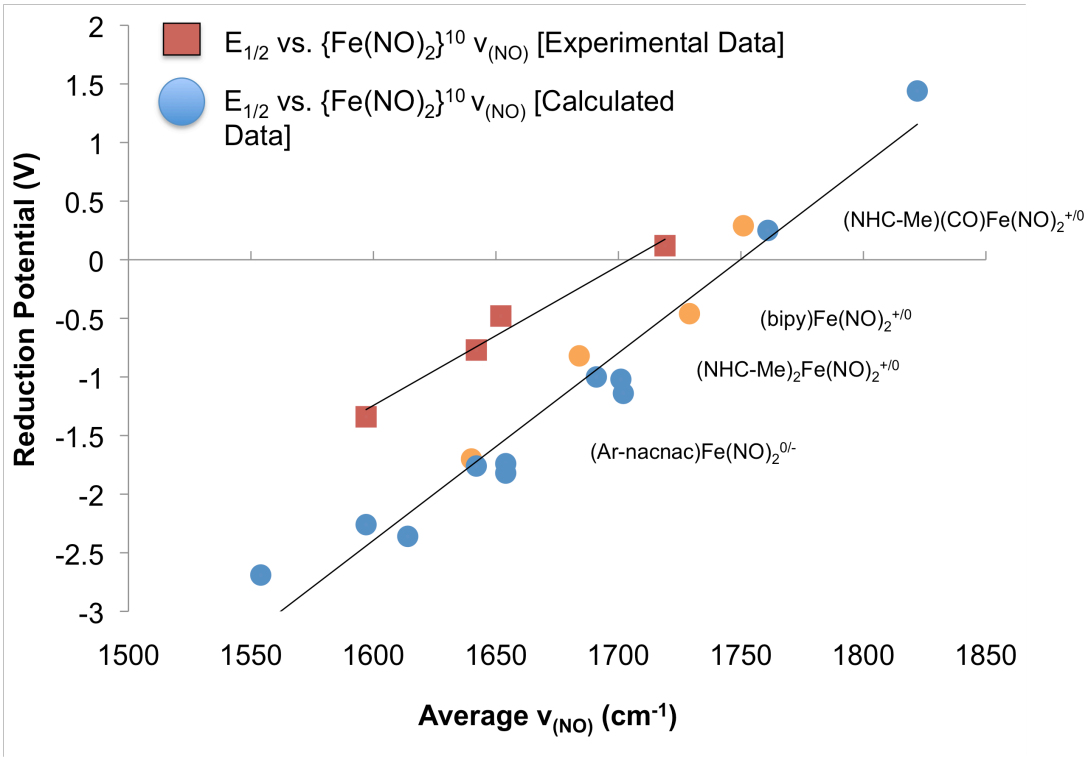

Figure V-4. Reduction potentials vs. average $\nu_{(NO)}$ for $\{Fe(NO)_2\}^{10}$ complexes. Orange circles represent the four computational complexes directly compared to experiment.

Table V-3. Experimental vs. Computational Spectroscopic and Electrochemical Data

	Complex	LL'Fe(NO)$_2$		Experimental $\nu_{(NO)}$	Calculated $\nu_{(NO)}$	Experimental $E_{1/2}$	Calculated $E_{1/2}$
		L	L'				
Neutral {Fe(NO)$_2$}^{10}	**1**	CO	CO	1807, 1762	1840, 1804	----	1.44 V
	2	CO	Imid-H	1731, 1687	1783, 1742	----	0.19 V
	3	CO	Imid-Me	1744, 1698[a]	1781, 1740	----	0.25 V
	4	CO	NHC-Me	1740, 1697	1770, 1732	0.12 V[b]	0.29 V
	5	Imid-H	Imid-H	1680, 1622	1726, 1678	----	-1.14 V
	6	Imid-Me	Imid-Me	1673, 1616	1724, 1677	----	-1.02 V
	7	Imid-Me	NHC-Me	----	1713, 1669	----	-1.00 V
	8	NHC-Me	NHC-Me	1667, 1616	1703, 1665	-0.77 V	-0.82 V
	9	bipy		1684, 1619	1750, 1708	-0.48 V	-0.46 V
Cationic {Fe(NO)$_2$}^{9}	**8$^+$**	NHC-Me	NHC-Me	1789, 1733	1809, 1771	-0.77 V	-0.82 V
Neutral {Fe(NO)$_2$}^{9}	**10**	Imid$^-$	Imid-H	----	1797, 1750	----	-1.74 V
	11	Imid-Me	SPh$^-$	1767, 1715[a]	1781, 1741	----	-1.82 V
	12	NHC-Me	SPh$^-$	1757, 1712[a]	1767, 1733	-1.33 V[a]	-1.76 V
	13	Ar-nacnac$^-$		1761, 1709	1768, 1730	-1.34 V	-1.70 V
Anionic {Fe(NO)$_2$}^{10}	**13$^-$**	Ar-nacnac$^-$		1627, 1567	1665, 1615	-1.34 V	-1.70 V
Anionic {Fe(NO)$_2$}^{9}	**14$^-$**	Imid$^-$	Imid$^-$	1774, 1712	1750, 1706	----	-2.26 V
	15$^-$	SPh$^-$	SPh$^-$	1737, 1693	1734, 1702	----	-2.36 V
	16$^-$	pdt^{2-}		1712, 1671	1707, 1674	----	-2.69 V

[a] Experimental data is given for corresponding ^{i}Pr NHC or Imid derivative.
[b] Potential is E_{pc} rather than $E_{1/2}$.

Commentary and Conclusions

Dinitrosyl iron complexes have been detected *in vivo* and *in vitro* as products of iron-sulfur cluster degradation by excess NO.[69,159-160] These protein-bound DNICs are posited as storage depots for NO, which might be mobilized by $Fe(NO)_2$ transfer to free cysteine, glutathione, or histidine. In these cases, the mobile, low molecular weight forms are suggested to be NO transporters, with possibility of delivering NO to a broad range of targets. Our studies relate to the possibility of redox states that promote or inhibit Fe-NO bond cleavage, with the oxidized form showing weaker Fe-NO interactions. More explicitly, we propose that the mechanism for NO release may be dependent on the presence of a biologically relevant mild redox potential so that the oxidized form of the DNIC is accessible, as $\{Fe(NO)_2\}^9$ is prone to NO release. As the reduced form of the complex is found to have stronger Fe-NO interactions versus the oxidized forms, we propose that $\{Fe(NO)_2\}^{10}$ must also be accessible biologically for NO storage. Neutral complexes with good σ-donors, such as protonated imidazole ligands, have oxidation potentials near the biological range described below.

As a majority of biochemical half-reactions occur within the range of +0.5 V to -0.5 V, with Fe^{3+} reductions noted to be approximately ~ +0.3 V, the data reported above can be analyzed in this regard.[161] Several points to note are that: 1) complexes that are known to epitomize the extremes of the reduced $\{Fe(NO)_2\}^{10}$ state, i.e. $(CO)_2Fe(NO)_2$ or the oxidized $\{Fe(NO)_2\}^9$ state, i.e. $(SPh)_2Fe(NO)_2^-$ exhibit electrochemical potentials that are quite positive (+1.44 V) or quite negative (-2.36 V), respectively; 2) complexes

that are good σ-donors versus π-donors or π-acceptors give more modest redox potentials, with the majority falling nearer the biological range (+0.25 V to -1.14 V); and 3) complexes that are the best mimics for biological coordination, that is, the imidazole complexes, have milder potentials in the protonated Imid-H form than the deprotonated $Imid^-$ form by approximately +0.6 V per ligand. Thus, the pH as well as the chemical environment is responsible for the variation in electrochemical potentials and could potentially regulate NO storage and release.

CHAPTER VI

CALCULATIONS OF MULTIMETALLIC CLUSTER COMPLEXES CONTAINING IRON DINITROSYL UNITS[*,‡]

Theoretical Investigations of Bimetallic $[Ni(N_2S_2)Fe(NO)_2(CO)]$ and Adamantyl $[Ni(N_2S_2)]_2[Fe(NO)_2]_3$ Complexes: Introduction

The discovery that the active site of [NiFe]-hydrogenase contains a nickel bound to four cysteinyl sulfurs,[162] two of which are bridging to an iron center has greatly advanced inorganic synthesis in the course of addressing specific ways to construct thiolate-S-bridged heterobimetallic complexes. The pseudo-square pyramidal iron center is completed by the biologically unusual diatomic ligands CO and CN^-, and the axial open site of the iron center is presumed to operate as the site promoting reactivity.[162] With this inspiration, we have set out to synthesize complexes with an architecture containing several distinguishing features: 1) a nickel site containing thiolate sulfurs bridging to an iron metal; and, 2) an iron center containing diatomic ligands. To date, only few complexes reproduce these features, and several of these are described in Figure VI-1.[163-165]

---

[*] Hsieh, C. –H.; Chupik, R. B.; Brothers, S. M.; Hall, M. B.; Darensbourg, M. Y. *Dalton Trans.* **2011**, *40*, 6047-6053. Reproduced by permission of the Royal Society of Chemistry (RSC).

[‡] Reproduced in part with permission from the *Journal of the American Chemical Society*, accepted for publication. Unpublished work copyright **2011** American Chemical Society. The manuscript has the following authorship list: Jennifer L. Hess, Chung-Hung Hsieh, Scott M. Brothers, Michael B. Hall, and Marcetta Y. Darensbourg.

The N_2S_2 binding motif, extensively described in Chapters I and III, has been utilized by both the Pohl group as well as our group in order to synthesize bimetallic $Ni(N_2S_2)Fe(L)_x$ complexes, and three of these are shown in Figure VI-2.[40,43,166] Figure VI-2 (a) indicates an example of a tetrahedral dinitrosyl iron complex bound to both thiolate sulfurs.[166] The analogous [Ni(bme-daco)Fe$(NO)_2$] was reported as an unisolated and unstable species by Darensbourg, *et al*. However, in this same report, a $(NO)Ni(S)_3Fe(NO)_2$, bridged by two thiolate sulfur atoms and reproducing several of the features of the [NiFe]-hydrogenase active site was characterized, and is shown in Figure VI-2 (c).[40]

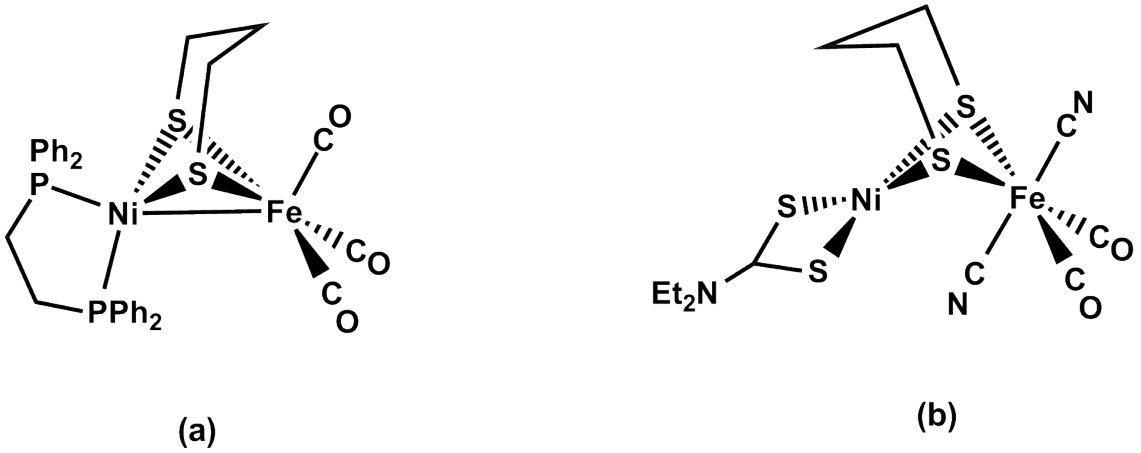

Figure VI-1. Ni-Fe complexes with bridging sulfurs and diatomic ligands on Fe.[163-165]

As the interest in both N_2S_2 and $Fe(NO)_2$ units has been a major focus of our group and others, we have recently isolated the complex [Ni(bme-dach)]$Fe(NO)_2(CO)$ for comparison to other $LFe(NO)_2(CO)$ complexes, *vide supra*.[167] That this complex binds Ni to Fe through only one sulfur begs the question of additional reactivity of the thiolate sulfur. This has been addressed experimentally by the addition of an equivalent of $(CO)_2Fe(NO)_2$, which leads to an interesting incomplete adamantane $Ni_2S_4Fe_3$ complex described below. We have also sought to explore the [Ni(bme-dach)]$Fe(NO)_2(CO)$ bimetallic complex by computations, especially regarding its unusual hinge angle ($\sim 90^0$) as well the likelihood for additional reactivity at sulfur. Density functional methods have also been applied to the multimetallic cluster structure. Here we address the presence and stability of the incomplete adamantane versus the complete adamantane structure.

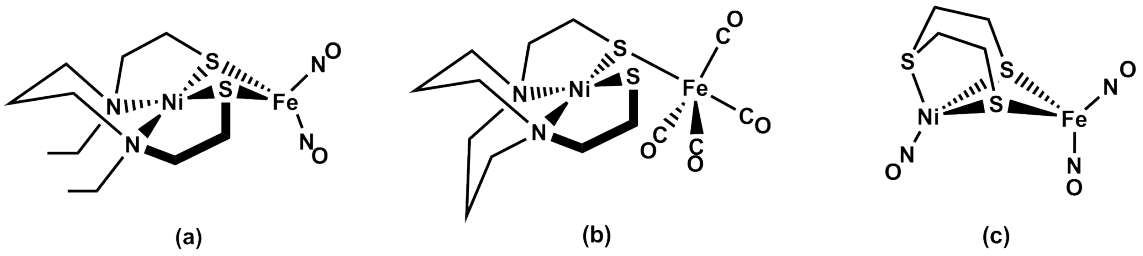

Figure VI-2. [NiFe]-hydrogenase models containing NiN_2S_2 metalloligands (a) and (b), or dinitrosyl iron units (a) and (c). [40,43,166]

Computational Details of Ni(bme-dach)Fe(NO)$_2$(CO)

The bimetallic complex [Ni(bme-dach)]Fe(NO)$_2$(CO), which has been synthesized by Dr. Chung-Hung Hsieh and Rachel Chupik, was probed computationally by the methodology developed for complexes containing an iron dinitrosyl unit and described in Chapter IV.[158] A reasonable computational/experimental match of both structural features and diatomic ligand stretching frequencies utilizes the TPSS functional[102] and a mixed basis set, with the Stuttgart-Dresden parameters and an effective core potential (ECP)[132] on the iron atom, the LANL2DZ ECP parameters unaugmented on nickel and with an additional d-function on the sulfurs.[131] For all other atoms, the basis set 6-311++G(d,p) was used.

These parameters adequately reproduce the crystallographic metric data, especially in the M–S and M–N bond lengths, which other functional/basis set pairs calculated too long. The salient features of the solid state structure, including the eclipsing of the Fe–N–O bond vector with the Ni–S bond, are computational/experimental matches; however we note a somewhat larger divergence in the Ni–S–Fe hinge angle, determined to be *ca.* 86° in the calculation *vs.* approximately 91° by experiment. The computed and crystallographic structures as well as an overlay structure are shown in Fig. VI-3, with geometric parameters given in Table VI-1.

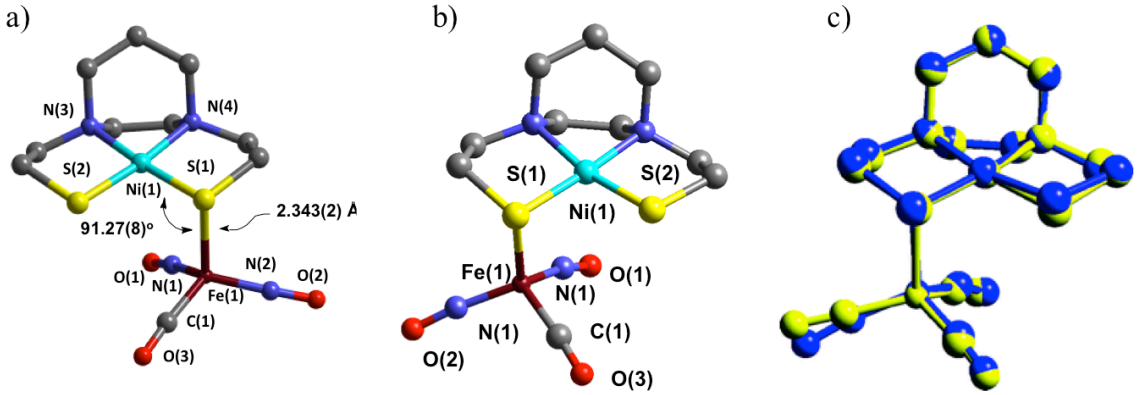

Figure VI-3. a) Crystallographic, b) computational, and c) overlay of experimental and computed structures of Ni(bme-dach)Fe$(NO)_2$(CO)

Table VI-1. Experimental vs. Calculated Data for Ni(bme-dach)Fe$(NO)_2$(CO)

	Experimental	**Calculated**
$\nu_{(CO)}, \nu_{(NO)}$ **(cm^{-1})**	*2006*, 1733, 1691	*2001*, 1767, 1694
Fe-S-Ni (°)	91.27(8)	86.18
Fe-N-O$_{in}$	172.4(3)	168.4
Fe-N-O$_{out}$	175.8(4)	172.0
Fe-Ni (Å)	3.229(3)	3.114
N-O$_{in}$	1.176(4)	1.193
N-O$_{out}$	1.167(5)	1.182
Fe-S(1)	2.3433(19)	2.360
Ni-S(1)	2.1699(17)	2.195
Ni-S(2)	2.161(2)	2.204

The experimental, THF solution-phase frequencies for the carbonyl and nitrosyl diatomic ligands were observed at $\nu_{(CO)}$ = 2007 cm^{-1} and ν(NO) = 1732 and 1689 cm^{-1}, whereas the calculated gas-phase frequencies are $\nu_{(CO)}$ = 2001 cm^{-1} and ν(NO) = 1767 (sym.) and 1694 cm^{-1} (asym.). The vibrational frequency at 2001/2007 cm^{-1}, is essentially a carbonyl stretch borrowing minimal intensity from the nitrosyl symmetric stretching vibration leading to an overall dipole oriented along the Fe–C–O vector. In a pseudo-C_{2v} system, which is assumed for other known iron dinitrosyl complexes of the form (L)Fe$(NO)_2$(CO) (where L = CO, N-heterocyclic carbene, *etc.*), the symmetric and asymmetric nitrosyl stretches are expected to draw equal intensity from each nitrosyl.

In the bimetallic Ni–Fe$(NO)_2$ complex **1**, one nitrosyl is oriented parallel to a Ni–S bond vector (defined as N–O_{in}) whereas the other is pointed away from the complex (defined as N–O_{out}). As a result of the asymmetry relative to regular C_{2v} complexes, the intensity gained from each nitrosyl in the symmetric and asymmetric stretches varies. The asymmetric stretch at 1694 cm^{-1} displayed a major intensity contribution from Fe–N–O_{in} with a corresponding minor intensity from Fe–N–O_{out}. The symmetric stretch, which was calculated as slightly higher than experiment (1767 *vs.* 1732 cm^{-1}) has its major intensity vector on the Fe–N–O_{out} vibration, drawing a moderate amount of intensity from the carbonyl vibration. A graphical depiction of these frequencies is found in Figure VI-4. The intensity ratios determined from computation are quite similar to those found experimentally, with the intensities of the nitrosyl stretches corresponding to 1732 and 1689 cm^{-1} having nearly the same intensity and that of the carbonyl stretch corresponding to 2007 cm^{-1} slightly smaller than that of the $\nu_{(NO)}$ stretches.

Among the frontier molecular orbitals (FMOs) of this bimetallic structure, the LUMO, HOMO, and HOMO-1 are mainly comprised of Ni and S character, with little to no contribution from the Fe unit; this manifold has been previously observed in computational studies of typical square planar $Ni(N_2S_2)$ complexes.[33,34,168] The three orbitals involved in the *ca.* 90° Ni–S–Fe interaction, which is essentially a Ni_d–S_p–Fe_d orbital manifold with small contributions from the p orbitals of N, C, and O in the $Fe(CO)_2(NO)$ moiety, are located below the HOMO-1. The atomic orbitals that make up these three molecular orbitals are as follows: the HOMO-2 is essentially of Fe character, with a smaller percentage of Ni character; the HOMO-3 is the reverse, with mainly Ni character and less Fe character; and the HOMO-4 is nearly equal in Ni and Fe character. A consequence of the energy separation of these delocalized Ni–Fe orbitals and the Ni–S based FMOs is that the HOMO, comprised of largely sulfur character, could be involved in additional S-based reactivity, a prediction corroborated by the formation of a Ni_2Fe_3 cluster. Representative orbitals are shown in Figure VI-5.

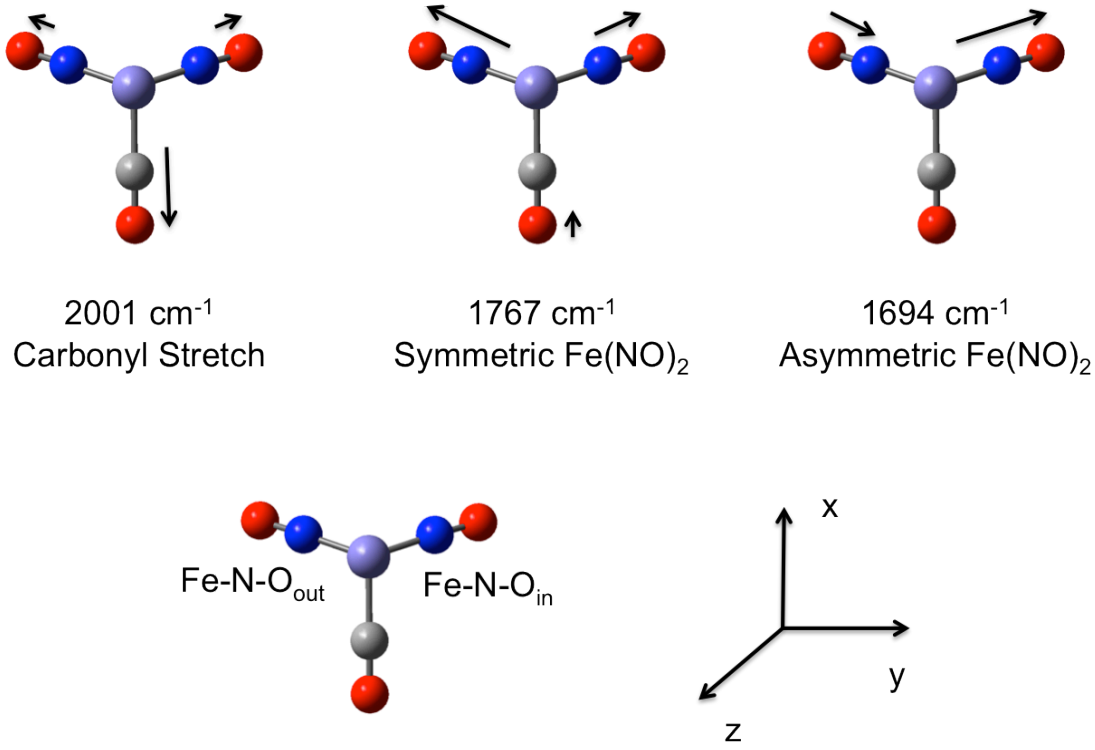

Figure VI-4. Composite intensities of [Ni(bme-dach)Fe(NO)$_2$CO] diatomic ligand vibrations (upper). View of the Fe(NO)$_2$(CO) unit is down the S-Fe bond vector, with the Ni-S bond eclipsing the Fe-N-O vector (defined as Fe-N-O$_{in}$).

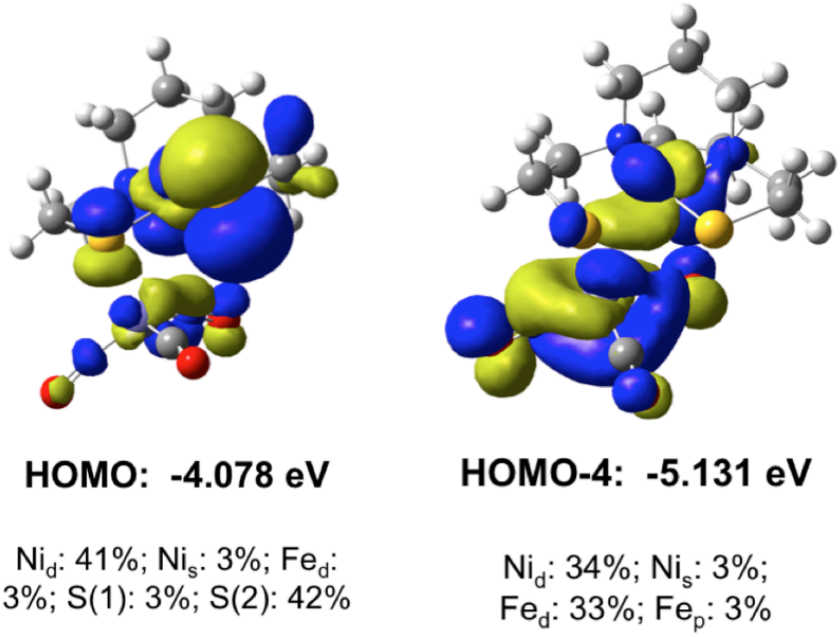

Figure VI-5. Selected Frontier Molecular Orbitals (FMOs) of [Ni(bme-dach)]$Fe(NO)_2(CO)$, generated at an isosurface value of 0.02. M_d, M_p, and M_s refer to the percentage of *d*, *p*, or *s* orbital character per metal, and S(1) refers to the bridging Ni–S–Fe sulfur, whereas S(2) is the terminal Ni–S thiolate.

Further synthetic work by Dr. Chung-Hung Hsieh explored the reaction of this [Ni(bme-dach)$Fe(NO)_2(CO)$] complex with an additional equivalent of the starting reagent $(CO)_2Fe(NO)_2$, with the expectation of binding a second $Fe(NO)_2(CO)$ unit on the available thiolate, as has been previously described for a NiN_2S_2 complex with two $W(CO)_5$ units.[25] In fact, self-assembly yielded a $Ni_2S_4Fe_3$ $[Ni(bme\text{-}dach)]_2[Fe(NO)_2]_3$ complex was synthesized, which internally contained an adamantane-type core with one missing apex; the skeleton structure of this is shown in Figure VI-5. Previously, adamantate-type structures containing CuN_2S_2 metalloligands had been formed in both

the $Cu^{II}_2S_4Cu^{I}_3$ and $Cu^{II}_2S_4Cu^{I}_4$ geometries, $[Cu^{II}(bme\text{-}daco)_2][Cu^{I}Cl]_3$ and $[Cu^{II}(bme\text{-}daco)_2][Cu^{I}Cl]_4$, respectively.[169] The skeleton structures of these two complexes can be compared to the Fe analogue, also in Figure VI-6.

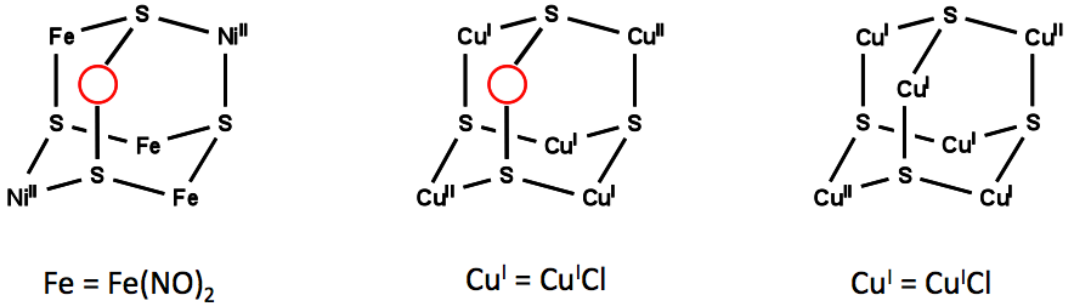

Figure VI-6. Skeleton structures of $Ni_2S_4Fe_3$, $Cu_2S_4Cu_3$, and $Cu_2S_4Cu_4$.

In order to understand why $Ni_2S_4Fe_3$ was found only in the incomplete 9-membered adamantane core, when the 10-membered version was found for $Cu_2S_4Cu_4$, we investigated the 9-membered $Ni_2S_4Fe_3$ cluster via density functional calculations. Overlays of $Cu_2S_4Cu_3$ and $Ni_2S_4Fe_3$ are presented in Figure VI-7, and it can be observed that the vacant site between the S atoms in the CuCu complex is approximately 0.15 Å shorter than that of the NiFe complex, 3.681 Å and 3.834 Å, respectively. In order to aid convergence, the model was truncated by clipping of the diazacycle carbon chains into methyl groups, *i.e.* each amine nitrogen of the metalloligand contained two methyl groups in order to decrease the overall number of basis functions. The space-filling

model of the optimized model complex is shown in Figure VI-7, and it shows that, although the S-S distance is overestimated, addition of a fourth $Fe(NO)_2$ can be excluded due to the steric blocks of the vacant site by the adjacent $Fe(NO)_2$ units. In fact, convergence of the 10-membered $Ni_2S_4Fe_4$ cluster was attempted but never achieved. However, the vacant site may have space enough to accommodate a linear metal unit as opposed to a tetrahedral metal unit, i.e., $Au(PPh_3)$ or Cu^ICl. This possibility is the topic of future investigation.

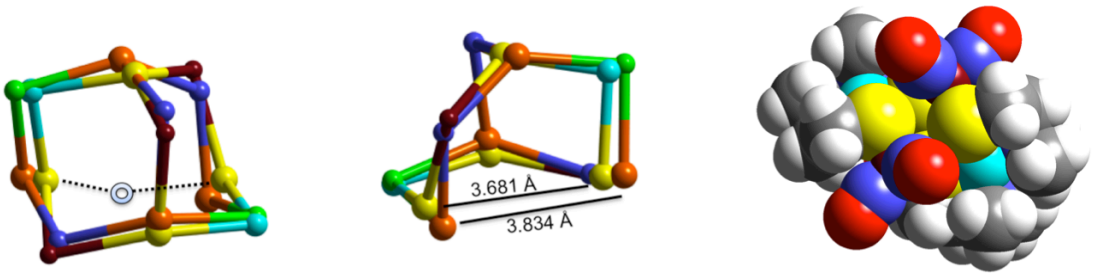

Figure VI-7. Overlay structures of $Cu_2S_4Cu_3$ (blue Cu^I, orange S, green Cu^{II}) and $Ni_2S_4Fe_3$ (red Fe, yellow S, blue Ni) [left] and optimized truncated model of $Ni_2S_4Fe_3$ with the vacant site facing out [right].

Comments and Conclusions

The orientation of the $[Ni(bme\text{-}dach)Fe(NO)_2(CO)]$ complex, with its near 90^0 hinge angle was investigated by density functional theory calculations. In this way, it was determined that the interaction responsible for this relatively pinched angle (close to

that of H_2S, 92^0) was a Ni_d - S_p - Fe_d interaction, with the *p* orbital of the sulfur oriented perpendicular to the NiN_2S_2, i.e., in the *z* direction. That the majority of the electron density of the HOMO of the bimetallic complex resides on the unbound thiolate sulfur is indicative of further reactivity, borne out by addition of $(CO)_2Fe(NO)_2$. However, a bidentate bridged [μ-Ni(bme-dach)][$Fe(NO)_2$]$_2$ structure was not obtained. Rather, self-assembly into a tight arrangement, resulting in a nine-atom cluster best described as an incomplete adamantane structure and missing one $Fe(NO)_2$ unit at an apex, was found.

The geometry and infrared frequencies of the bimetallic complex have been calculated and are found to match well with the experimental values, confirming the quality of the optimized structure. Calculation of several other bimetallic structures not reported here, including [Ni(bme-daco)$Fe(CO)_4$], [Ni(bme-dach)$Fe(CO)_4$], and Ni(bme-daco)$Fe(NO)_2(CO)$] indicate an that in increasing steric bulk of the NiN_2S_2 ligand backbone from bme-dach to bme-daco, an expansion of 13° of the Ni-S-Fe angle is seen. Furthermore, with an identical ligand backbone, i.e. bme-dach or bme-daco, and modification of the iron unit from $Fe(NO)_2(CO)$ to the isoelectronic $Fe(CO)_4$ also indicates an expansion of 13º. Calculations in which the orientation of the carbon atoms of the S-$(CH_2)_2$-N linkers have been minimally changed indicate the presence of low energy isomers; thus, the observed hinge angles are likely an effect of a variety of steric and electronic effects or possibly crystallographic packing.

Computations of Imidazolate-Edge-Bridged Molecular Squares Containing Dinitrosyl Iron Units: Introduction

In investigations of dinitrosyl iron complexes utilizing ligands that could be biologically relevant, a variety of $(L)(L')Fe(NO)_2$ complexes were prepared in our laboratory utilizing imidazoles with different substituents, such as N-heterocyclic carbenes and imidazoles.[89] Several complexes where L = CO and L' = Imid-R were synthesized and structurally characterized. However, in synthetic attempts using typical conditions for the bis-imidazole dinitrosyl iron complexes, auto-oxidation appeared to occur, producing the tetrameric $[(Imid\text{-}R)Fe(NO)_2]_4$ cluster. A cluster of this type had been previously reported by the group of Li and coworkers.[80] Dr. Jennifer Hess has also isolated and characterized the tetramers using both isopropylimidazole and benzylimidazole.[89] The core of the imidazolate-bridged tetramers is a so-called "molecular square" architecture, where the corners of the square-like structure are typically 3- or 4-coordinate metal atoms in which two ligands are near one another, causing a pinched L-M-L angle of approximately 90^0, much like the corner of a typical square. In these examples, the $Fe(NO)_2$ unit is found to exist as tetrahedral $\{Fe(NO)_2\}^9$, with S = ½ per iron, and the Imid-Fe-Imid angles form the geometric square.

The tetramers studied herein are $[(Imid\text{-}H)Fe(NO)_2]_4$ (**1**),[80] $[(Imid\text{-}^iPr)Fe(NO)_2]_4$ (**2**),[89] and $[(Imid\text{-}Benz)Fe(NO)_2]_4$ (**3**) and their structures and orientations of the imidazolate planes are shown in Figure VI-8. In **1**, the square exists in an all-up configuration (that is, all four imidazolate methylene carbons are oriented in the same direction in space), in which the imidazolate planes are canted away from one

another, see the green and orange planes. This can be compared to **2**, which has an up,down,up,down (that is, alternating imidazolate methylene carbons are pointed in opposite directions) configuration with the iso-propyl groups pointed inward toward the cavity. Finally, in the crystallographic structure of **3**, the up,down,up,down configuration is also seen, however rather than **1** and **2**, which have relatively equivalent pairs of opposite imidazolate groups, in **3**, one pair of imidazolate are pointed outward from one another (~10.2 Å), whereas one pair is pointed towards one another (~ 3.4 Å). Whether this arrangement is due to the crystallographic packing or arises from intramolecular bonding properties is the focus of this chapter. Extended packing diagrams of **1** and **3** can be seen in Figures VI-9 and VI-10.

Molecular squares containing bridging imidazolates have been previously observed by Lippard, *et al.*,[170-171] and Haupt, *et al.*,[172] in which the metal is Cu^{II} in a $(N,N')Cu(imid)_2$ environment, where N,N' is a bidentate nitrogen donor ligand. An interesting feature of both the $[Cu(imid)]_4$ and $[(imid)Fe(NO)_2]_4$ systems is the capability for magnetic coupling. Coupling in the copper-imidazolate systems is on the order of 50-100 cm^{-1}, with the strongest coupling at 163 cm^{-1}, as reported by Lippard.[173] A computational study of several bridging Cu-imid-Cu complexes has indicated that the degree of coupling (J value) is as a result of the M-N-C angle, where the carbon atom corresponds to the methylene carbon of the imidazolate unit.[134] We have undertaken a theoretical investigation of the bridged iron-imidazolate complexes in order to determine the structural effects of varying the orientation and steric bulk of the imidazolates, and a

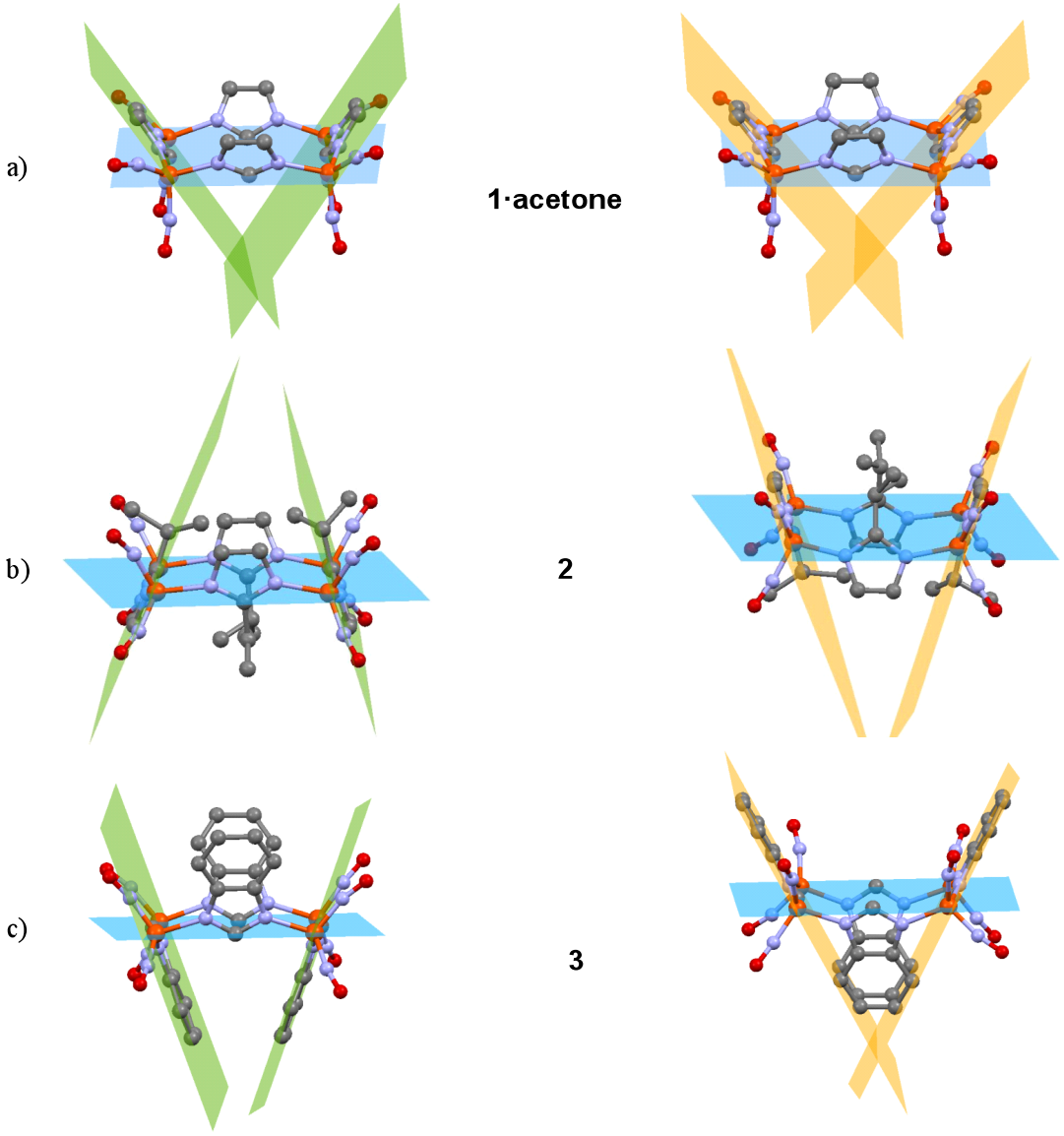

Figure VI-8. Crystallographic structures of tetramers **1**, **2**, and **3**. Figure reproduced with permission from Hess, J. L.; Hsieh, C. –H.; Brothers, S. M.; Hall, M. B.; Darensbourg, M. Y. *J. Am. Chem. Soc.*, submitted.

study of the magnetic coupling may be a topic for future investigation. The work presented herein is subject for publication and is currently under review.

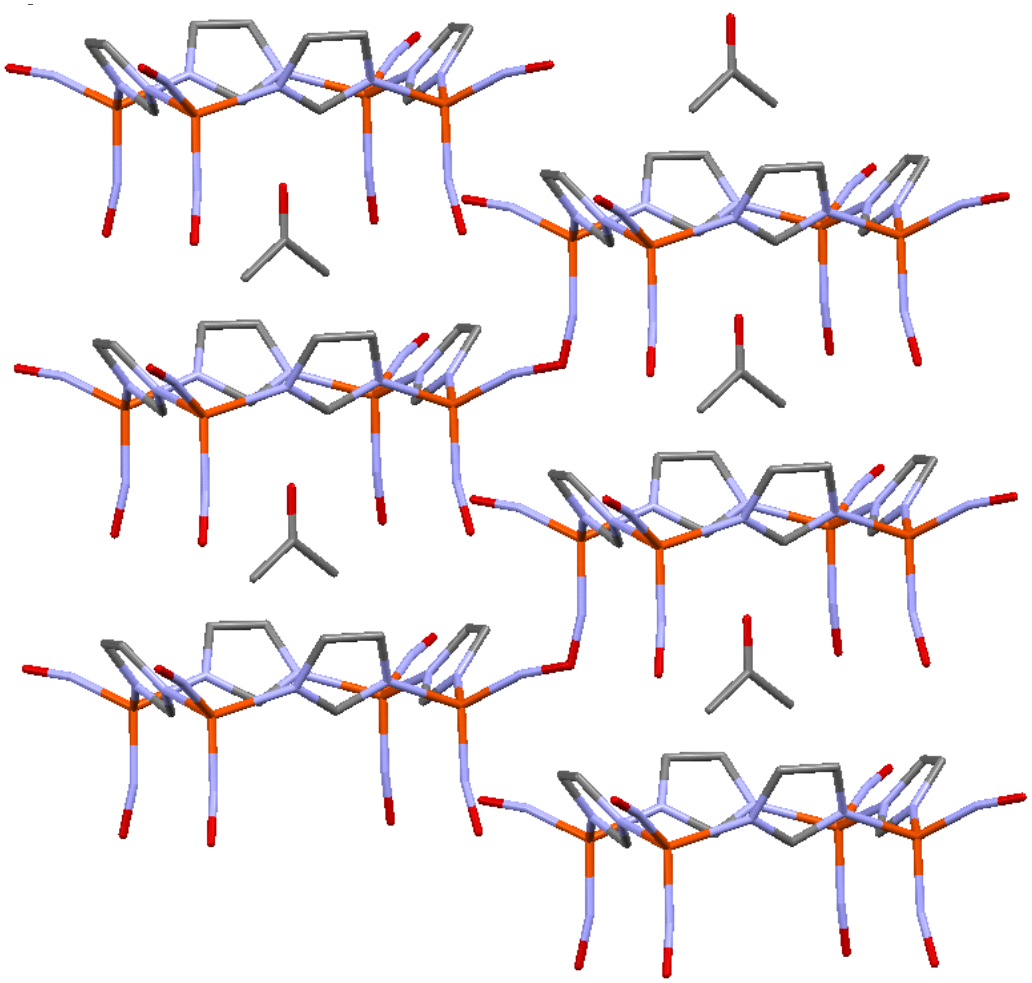

Figure VI-9. Extended packing diagram of complex **1**. Figure reproduced with permission from Hess, J. L.; Hsieh, C. –H.; Brothers, S. M.; Hall, M. B.; Darensbourg, M. Y. *J. Am. Chem. Soc.*, submitted.

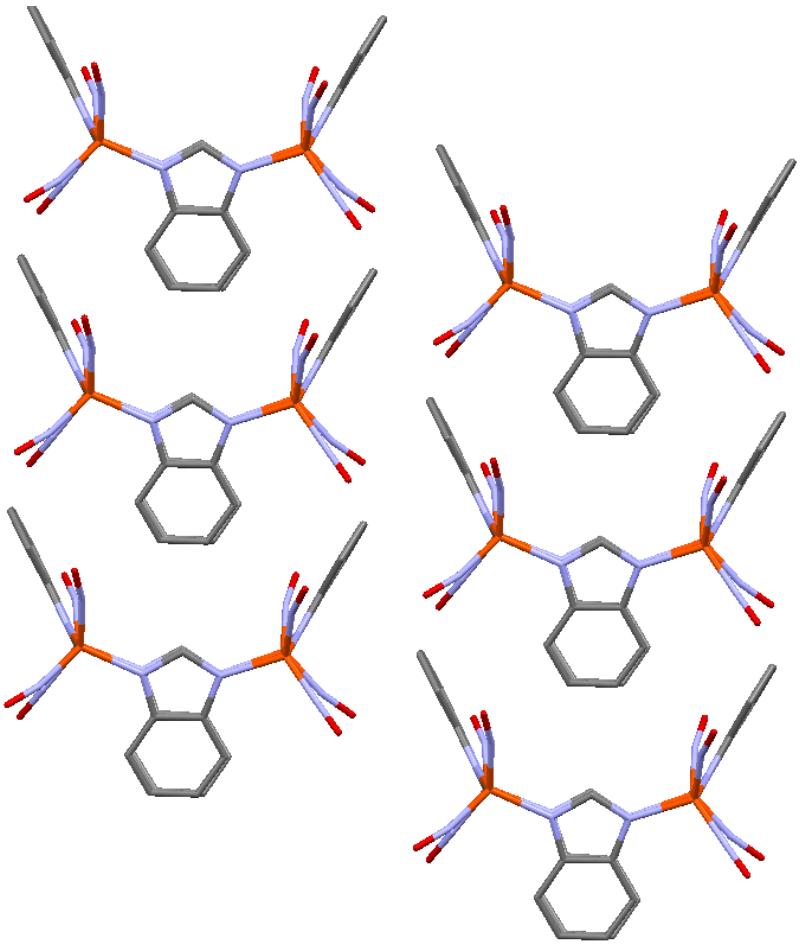

Figure VI-10. Extended packing diagram of complex **3**. Figure reproduced with permission from Hess, J. L.; Hsieh, C. –H.; Brothers, S. M.; Hall, M. B.; Darensbourg, M. Y. *J. Am. Chem. Soc.*, submitted.

Computational Studies

The optimizations of [(Imid-H)Fe$(NO)_2]_4$ (**1**), originally synthesized by Li, *et al.*,[80] [(Imid-^{i}Pr)Fe$(NO)_2]_4$ (**2**),[89] and [(Imid-Benz)Fe$(NO)_2]_4$ (**3**), both originally synthesized by Dr. Jen Hess of our group, were performed. They were started from crystallographic structure coordinates of the single tetramer, with the acetone molecule

removed from the broad edge of the bowl in **1**, and were performed on the singlet, triplet, and quintet states of the molecules. The antiferromagnetic singlet state was found to be of lowest energy, with the triplet and quintet states only slightly higher in energy (for **1**, 0.54 and 1.09 kcal/mol, for **2**, 0.73 and 1.47 kcal/mol and for **3**, 0.88 and 1.61 kcal/mol, respectively), indicating a very low energy barrier for spin flipping at room temperature, increasing with the larger imidazolate and a greater degree of molecular asymmetry. Energy diagrams for the isomers are described in Figures VI-11 through VI-13. Any coupling present in the tetramer is expected to be weak due to the large distances between the iron atoms. Consistent with this, room temperature Evans' method magnetic susceptibility data indicates 1 unpaired electron per iron.

The computational methodology used reproduced the vibrational frequencies especially when solvation was included. The vibrational frequencies for $\mathbf{1}_{\mathbf{calc.}}$ and $\mathbf{3}_{\mathbf{calc.}}$ for the gas-phase and solution-phase are follows: $\mathbf{1}_{\mathbf{calc.}}$: 1824/1774 cm^{-1} (g.p.) and 1813/1739 cm^{-1} (CH_2Cl_2), similar to that found for $\mathbf{1}_{\mathbf{exp.}}$, 1805 and 1737 in CH_2Cl_2. Similarly, the frequencies for $\mathbf{3}_{\mathbf{calc.}}$ were found to be 1810/1767 cm^{-1} (g.p.) and 1797/1733 cm^{-1} (CH_2Cl_2), matching well with the $\mathbf{3}_{\mathbf{exp.}}$ CH_2Cl_2 values of 1805 and 1739 cm^{-1}. Additional results are found in Table VI-2.

The geometric parameters from optimized structures are not significantly different between singlet, triplet, and quintet states. Beginning from the orientations of the x-ray crystal structures, the calculated metric parameters of one unit of complexes **1**, **2** and **3** substantially match experimental values (see Table VI-2). However, as shown in Figure VI-11 through Figure VI-13 and Table VI-2, there are differences in the

canting of the imidazolate planes, particularly for the benzimidazole of complex **3**. The gas phase calculation of this tetramer finds the imidazolate planes ⊥ to the Fe_4 plane and largely parallel to each other. This distinction suggests a role for non-covalent interactions or crystal packing in the solid state.

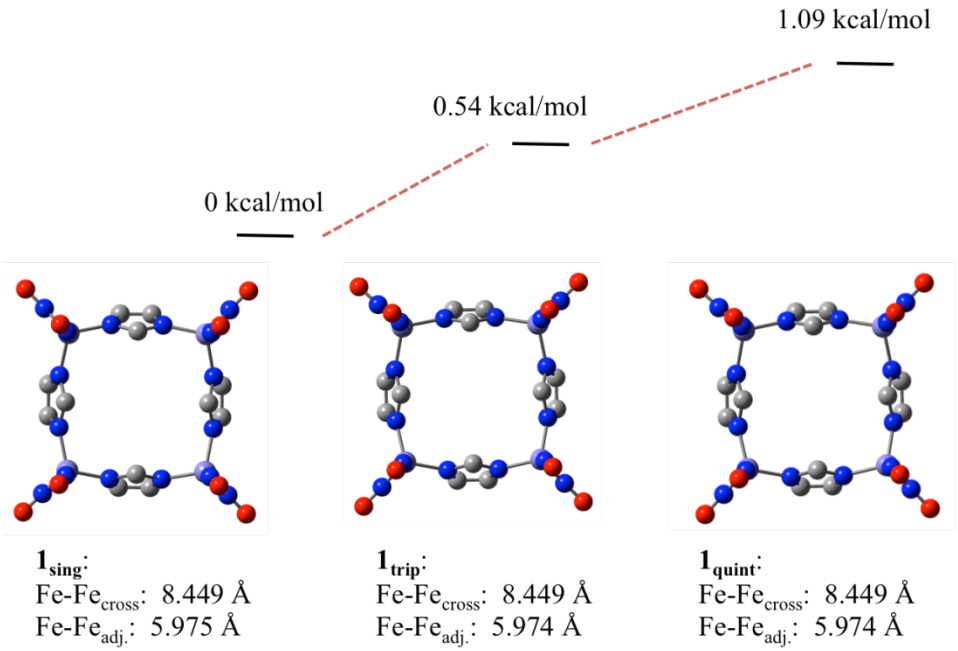

Figure VI-11. Energy diagrams for $\mathbf{1}_{sing.}$, $\mathbf{1}_{trip.}$, and $\mathbf{1}_{quint.}$.

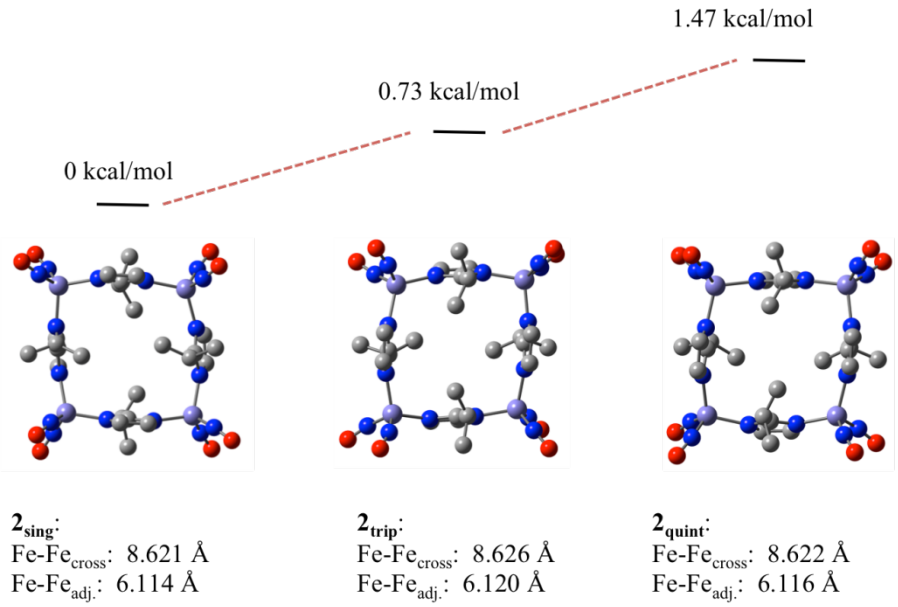

Figure VI-12. Energy diagrams for $\mathbf{2}_{\mathbf{sing.}}$, $\mathbf{2}_{\mathbf{trip.}}$, and $\mathbf{2}_{\mathbf{quint.}}$.

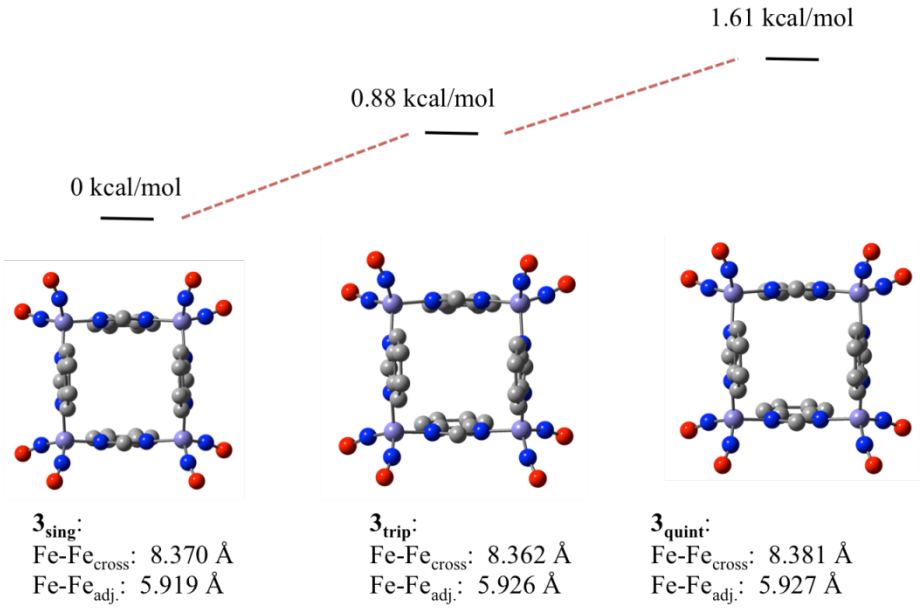

Figure VI-13. Energy diagrams for $\mathbf{3}_{\mathbf{sing.}}$, $\mathbf{3}_{\mathbf{trip.}}$, and $\mathbf{3}_{\mathbf{quint.}}$.

Table VI-2. Selected Averaged Bond Distances (Å), angles (°), and $\nu_{(NO)}$ (cm^{-1}) for Complexes **1**, **2**, and **3**.

	Fe-Fe_{cross}	Fe-Fe_{adj}	Imid-$Imid_{cross}$[a]	Fe-N-C(imid)	$\nu_{(NO)}$ (cm^{-1}, CH_2Cl_2) [$\nu_{(NO)}$ (cm^{-1}, g.p.)]
$\mathbf{1}_{exp}$	8.440	5.971	8.425	125.33	1805, 1737
$\mathbf{1}_{quint}$	8.449	5.974	7.493	126.87	1813, 1739 [1824, 1774]
$\mathbf{1}_{up/down}$	8.407	5.945	5.665	126.13	
$\mathbf{2}_{exp}$	8.826	6.241	7.777	133.31	1797, 1729
$\mathbf{2}_{quint}$	8.624	6.118	7.079	131.22	[1807, 1759]
$\mathbf{3}_{exp}$	8.520	6.027	10.240 / 3.409	127.33	1805, 1739
$\mathbf{3}_{quint}$	8.371	5.924	5.419 / 5.418	124.62	1797, 1733 [1810, 1767]
$\mathbf{3}_{frozen}$	8.413	5.948	10.240 / 4.776	125.06	
$\mathbf{3}_{up/up}$	8.419	5.953	9.854 / 9.816	125.49	

[a] Defined as the distance between opposite imidazolate groups.

An additional calculation of complex **3** was performed; a structure corresponding to a single tetramer in which bond distances, valence angles, and dihedral angles of the cross imidazolate groups that correspond to the broad edge of the bowl were frozen to observe the effect on the cross imidazolate interactions corresponding to the narrow edge of the bowl ($\mathbf{3_{frozen}}$). In $\mathbf{3_{frozen}}$, in which the arene rings of **3** opposite one another (the rings outlined in red in Figure VI-14) were held frozen, the arene rings 3.4 Å apart were allowed to relax. In this conformation, *i.e.*, with the observed canting as described in Figure VI-14 and in the experimental structure, the distance between the unfrozen rings expanded (see Table VI-2) and the calculated energy is 3.59 kcal higher than the optimized gas phase structure. It should be noted that the opposite frozen structure was calculated (*i.e.*, the close arene rings held frozen with the distant arene rings allowed to relax), and a similar effect was found, with the arene rings 10.2 Å apart optimizing to a structure whereby they approximate a parallel geometry.

By computations we explored the interchange of imidazolate orientational isomers of **1** and **3** ($\mathbf{1_{up/down}}$ and $\mathbf{3_{up/up}}$), creating for **3** a "super-bowl" when in the (up, up, up, up) orientation, Figure VI-15. The difference in energy between the two isomers of **1** is 0.82 kcal/mol, favoring the all-up configuration that is found in the solid state structure. As an acetone molecule crystallized in the open bowl of complex **1**, the energetic preference of this orientation even in its absence was unexpected. For gas-phase **3**, the all-up orientation is favored over the (up, down, up, down) orientation, albeit by a mere 0.05 kcal/mol. This is in contrast with the orientation in the crystallographic structure, again implying that intermolecular interactions are

responsible for the observed conformation in the solid state. Structural details of these additional computed isomers of **1** and **3** can be found in Table VI-2 and Figure VI-15.

To further probe such solid state effects on structure, a structure comprised of two adjacent tetramers lifted from the crystallographic unit cell was optimized with starting coordinates taken from the experimental data (**3"**). This dimer of tetramers was optimized with each tetramer in an open-shell, quintet spin state (S = 2). As shown in Figure VI-16, the nested (interior) imidazolates of the dimer of tetramers have arene-arene cross distances similar to the x-ray structures, while the exterior arene-arene orientations are little perturbed from the gas phase, single tetramer structure. The electronic energy of the dimer of tetramers was calculated to be 1.31 kcal/mol higher in energy than the sum of the electronic energies of two independent tetramers. This indicates that the crystal packing and nesting with close arene edge-face intermolecular distances promotes the "open, closed" structure in $\mathbf{3}_{\mathbf{exp.}}$; the solution- or gas-phase ground state is likely the average structure seen in $\mathbf{3}_{\mathbf{calc}}$.

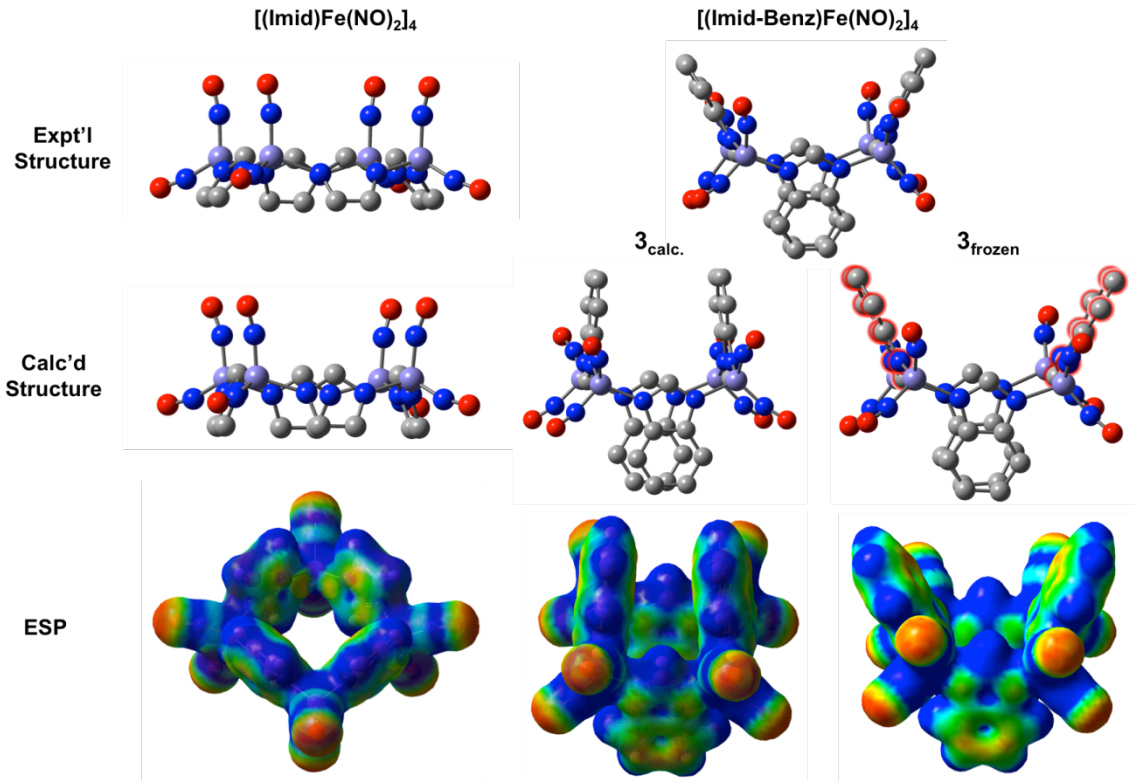

Figure VI-14. Experimental and computational structures and electrostatic potentials for **1** (left) and **3** (right), with the calculated coordinates taken from $\mathbf{3}_{\mathbf{quint.}}$ Both $\mathbf{3}_{\mathbf{calc.}}$ and $\mathbf{3}_{\mathbf{frozen}}$ are shown, with the imidazolate groups held frozen in the latter shown outlined in red. Electrostatic potentials were generated at an isosurface value of 0.01.

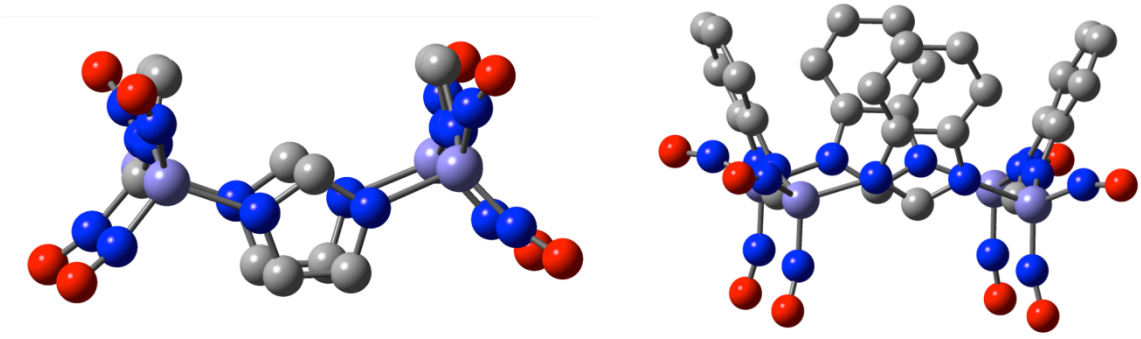

Figure VI-15. Orientational isomers of **1** (up/down, left) and **3** (up/up, right).

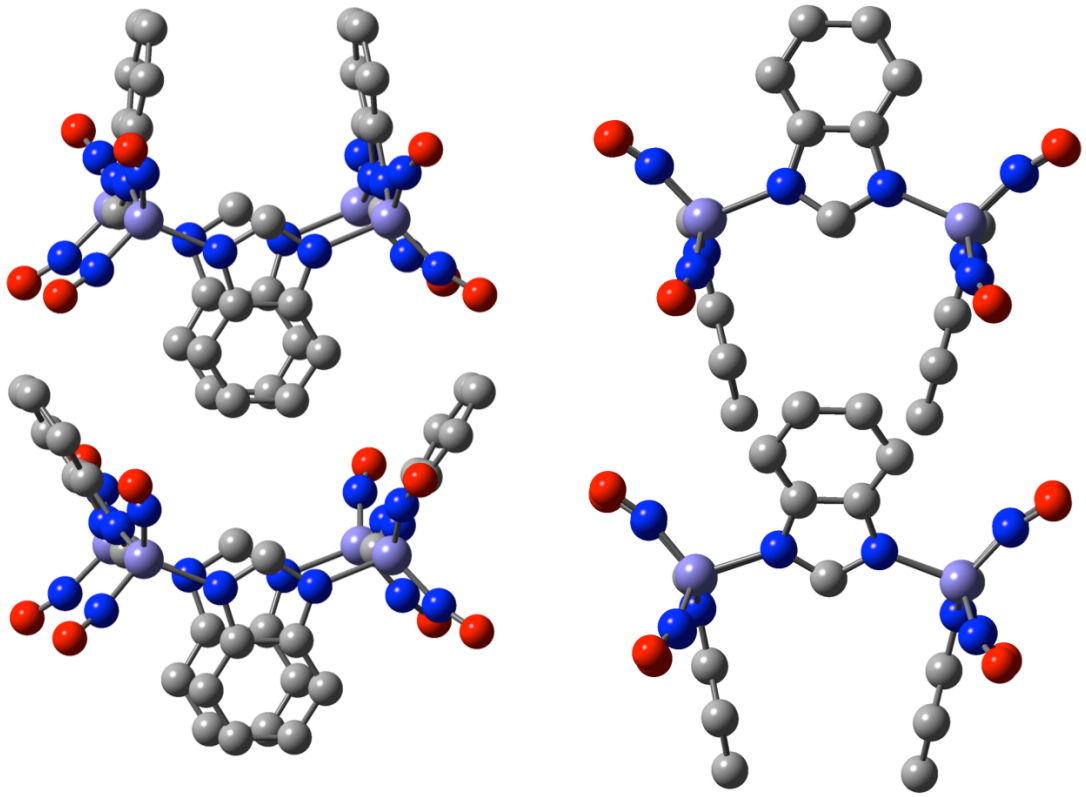

Figure VI-16. Two views of **3"**, which is two units of $\mathbf{3}_{\mathbf{calc.}}$, rotated 90^0 from one another.

Comments and Conclusions

The gas-phase calculations of **1** indicated that the optimal orientation is the bowl-like structure as adopted in the solid-phase, x-ray determined structure, with each methylene C-H unit pointed into space on the same face of the molecular square. That the up/down/up/down configuration was higher in energy confirms this geometry, although the small energy difference could indicate that other low energy isomers could

arise. Despite this result, the solid-state structure experimental structure adopts the bowl structure with an included solvent molecule.

Alternatively, calculations of **3** in the gas-phase indicate that the "super-bowl", in which the benzyl groups of the benzimidazolate ligands are pointed outward from the same face of the molecular square is energetically favored over the crystallographically determined geometry, which adopts the up,down,up,down configuration with one set of oppositely oriented imidazolates 10.2 Å and the other set of oppositely oriented imidazolates 3.4 Å apart. To probe a rationale for an orientation of this type, a structure containing two adjacent tetrameric units of the unit cell (**3"**) was computed. It was found that the external imidazolate units attempted to reach the average structure found in the gas-phase calculations, whereas the internal imidazolate units were found to mimic the structure of the solid-state structure, implying that intermolecular effects introduced by efficient crystal packing are responsible for the solid-state crystallographic structure. As in **1**, other low energy isomers for **3** cannot be ruled out in the gas- or solution-phases.

CHAPTER VII

CONCLUSIONS

Theoretical chemistry, which traditionally has been utilized in the fields of organic and solid-state inorganic chemistry, has seen its applications expand due to the development of density functional theory. Through the use of these lightweight computational techniques as well as newly developed and user-friendly software programs, DFT has rapidly become a tool by which experimentalists in all fields of chemistry use to augment their crystallographic and spectroscopic results. In particular, the combination of DFT with experimental results in biological based systems meant to mimic active sites of enzymes or transport systems has led to a deeper understanding of how these systems operate *in vivo*. The endgame of all of these studies resides in how we may imitate their reactivity through synthetic models in efforts to solve current catalytic challenges. A leader in the field of integration of theoretical results with modern and advanced synthetic techniques is Dr. Ed Solomon, one of our collaborators, at Stanford University, who has pioneered investigations using copper complexes.[174-175]

In our studies, with the aid of density functional theory calculations, electronic effects of systems as diverse as $M(N_2S_2)$ as biomimetics for the distal site of ACS as well as dinitrosyl complexes as NO storage/delivery agents have been explored and, whenever possible, compared to experiment. A common theme in metallobiochemistry, and in particular the work described above has been in understanding the "non-innocence" and extensive delocalization that may be present in the ligand environment

of metals, specifically those metals found both in biological and biomimetic coordination environments. Although the topics of $M(N_2S_2)$ and $Fe(NO)_2$ chemistry may at first seem unrelated, that in the reactive frontier molecular orbitals a large degree of the electron density and reactivity is a result of induction effects of the ligands themselves shows the complexity of binding sites of metals in biology. Furthermore, we have synthesized and computationally explored a complex that literally bridges both of the topics, [Ni(bme-dach)$Fe(NO)_2(CO)$],[167] which has been described in Chapter VI.

Current Directions in Biomimicry of N_2S_2 Binding Sites

Although the original syntheses of nickel in $N_2S_2^{4-}$ binding sites was undertaken as an approach towards models of the NiS_4 environment of the nickel of [NiFe]-hydrogenase,[11] the complexes were later found to have applicability in other active sites upon the discovery of ACS and Nitrile Hydratase, both of which have a Cys-X-Cys binding motif.[56,58-59] Whereby a number of neutral NiN_2S_2 as synthesized by us,[12-15] anionic mixed amido/amine complexes by others,[31-32] and the direct peptidic $Ni(CGC)^{2-}$ complex by us and Riordan, *et al.* have been investigated,[27,29-30] still the most widely used model of Ni_d in ACS is Holm's $Ni(ema)^{2-}$ complex.[11] This complex maintains a Ni^{II} in a square planar geometry with two amido nitrogens and two thiolate sulfurs and an overall dianionic charge, all vital characteristics for the $Ni(CGC)^{2-}$ binding motif. That the Ni_d unit of ACS is found to bind to the Ni_p through thiolate sulfurs has been of interest to synthetic chemists.

By investigations of the $Ni(ema)^{2-}$ unit with a variety of electrophiles, Dr. Kayla Green, Dr. Marilyn Rampersad, and others successfully synthesized complexes displaying a wide array of reactivity at the thiolates, see Scheme VII-1.[23,27,34] With this inspiration, we sought to describe the effects of thiolate reactivity, which is akin to biological post-translational modifications. We determined that the result of modification of one sulfur results in a decreased nucleophilicity of the second sulfur, which had been previously indicated, and that modification of both sulfurs led to full deactivation of the thiolate sulfurs.[33] Correspondingly, upon alkylation of the thiolate sulfurs, NBO analyses displayed an effect whereby the covalent Ni-S and dative Ni-N interactions of the parent $Ni(ema)^{2-}$ complex switch in the modified complex to indicate a weakened, dative Ni-S interaction and a stronger, covalent Ni-N interaction. Since the binding of one of the thiolate sulfurs to an electrophile appears to reduce the nucleophilicity of the second sulfur, this result would be consistent with the ACS mechanism proposed previously by Hall, *et al.*, in which they invoke a hemilabile Ni_p-S interaction.[35]

Furthermore, the $N_2S_2^{4-}$ coordination sphere was examined by virtue of replacing Ni^{II} with Cu^{II}, as the discovery of Cu_p led to the question of why there is apparent exclusion of Cu in the distal site. Through our investigations, it was determined that, despite difference in the M-N and M-S bond lengths due to the electron in the d_{x2-y2} antibonding orbital with Cu, no significant difference was present by which to rule out Cu_d. Thus, the absence of Cu_d in biological studies to date indicates that it is as a result of a biosynthetic pathway and upstream regulation.[30]

Scheme VII-1

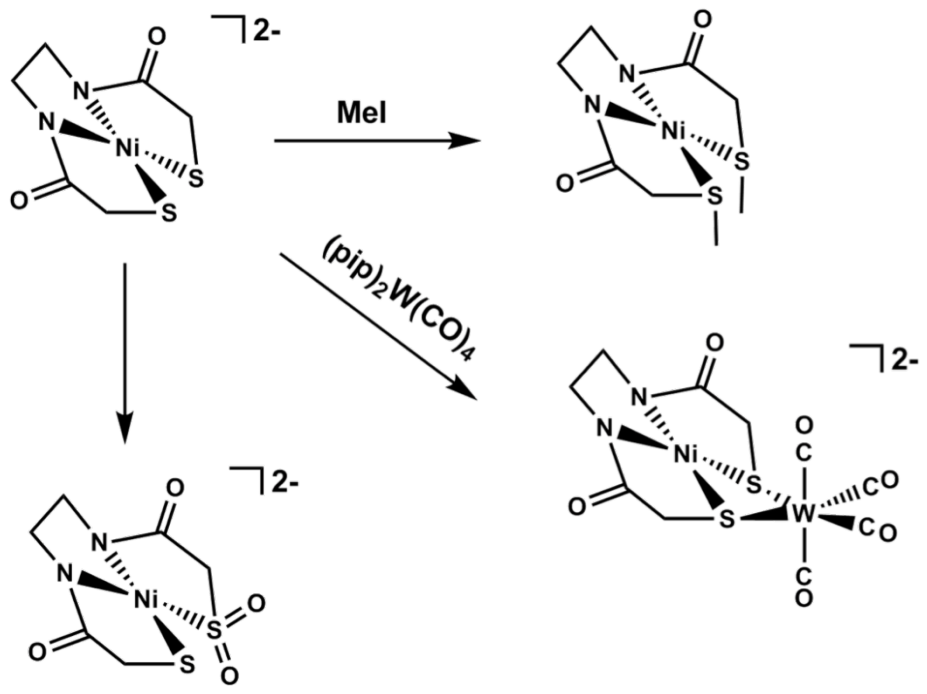

Horizons in Dinitrosyl Iron Chemistry

Since the discovery of the protein-bound DNIC that was produced by addition of a $Fe(NO)_2$ unit to human glutathione transferase,[69] as well as through the studies of both HMW-DNICs and LMW-DNICs and Roussin's red esters by a number of research groups, the biological role for NO has been more thoroughly investigated.[64-68,70-79] The possibility that HMW-DNICs can be invoked for NO storage and LMW-DNICs for NO transport has gained popularity as the mechanism for NO delivery *in vivo*. In our laboratories we have utilized biologically-relevant ligands (i.e. imidazoles and thiolates) as well as N-heterocyclic carbenes in order to investigate the ancillary ligand effect on

the $\{Fe(NO)_2\}$ unit, in addition to monitoring ligand substitutions by infrared spectroscopy.[61,89] Through these studies it was concluded that NO release was significantly easier in the oxidized $\{Fe(NO)_2\}^9$ complexes versus the reduced $\{Fe(NO)_2\}^{10}$ complexes, which indicates that these two forms could be targets for NO transport and NO storage, respectively. In several cases, both the oxidized and reduced forms of a complex containing identical ligands was observed, indicating that there may be a trigger for NO release in oxidation from the reduced form to the oxidized form.[89]

In Chapter V, we have investigated a series of dinitrosyl iron complexes utilizing a wide variety of ligands ranging throughout the spectrochemical series. A methodology developed as a computational probe of DNICs was used, and it was found that the calculated geometric, spectroscopic, and electrochemical parameters determined matched well with experiment.[158] The above studies utilized a set of computational parameters commonly used by inorganic chemists such as the BP86 functional and typical Pople basis sets. Armed with these techniques, we have deemed it important to explore various combinations of functionals and basis sets to achieve a good match of computational and experimental results. We have determined that the $(L)(L')Fe(NO)_2$ complexes using biologically relevant ligands such as imidazoles or N-heterocyclic carbenes displayed electrochemical potentials that fall well in the realm of biologically-accessible potentials, supporting a NO release trigger activated by some potential gradient in biology. The potential may also be governed by the pH of the environment, as comparison of $[(Imid^-)_2Fe(NO)_2]^-$ to $[(Imid\text{-}H)_2Fe(NO)_2]^+$ complexes shows a positive

shift of +0.6 V with each protonation, with the doubly protonated system showing a potential in the biologically relevant range. This is indicated in Figure VII-1.

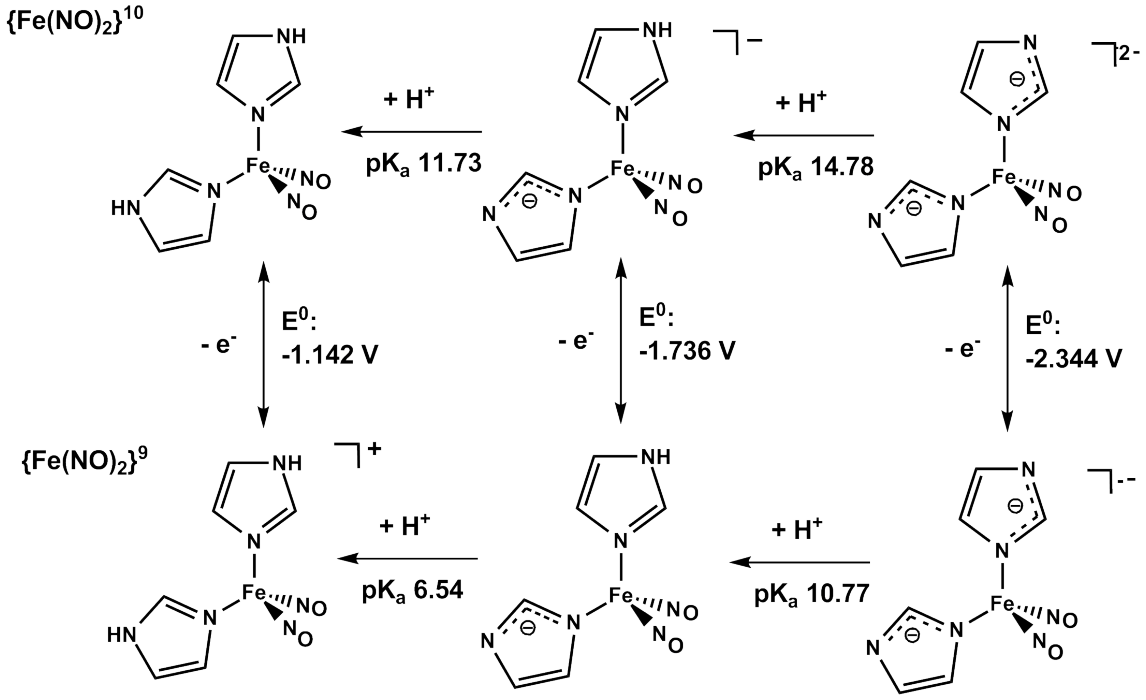

Figure VII-1. Calculated electrochemical and pK_a data for $(Imid)_2Fe(NO)_2$ complexes.

Future Directions

In this work, the N_2S_2 and $Fe(NO)_2$ units have been examined extensively by density functional theory. In the NiN_2S_2 case of the former and the imidazole case in the latter, each of these types of units have shown aggregation to cluster complexes. NiN_2S_2 complexes are well-known to aggregate into paddlewheel and other multimetallic motifs

through the bridging μ-S thiolates,[12,21] whereas the $Fe(NO)_2$ unit has been shown to form both bimetallic and tetrameric complexes.[89,167] Although in proteins there is typically control to avoid such aggregation, which is likely governed by the second coordination sphere, many enzymes do display multimetallic active sites, a number of which have been described within this dissertation. Therefore, investigation of these motifs is important, as, even though there are likely preventative measures against aggregation *in vivo*, the breakdown of such protection may lead to biological cluster complexes of importance to disease mechanisms detected as a result of these types of ligation.

In order to better understand the work described above, future directions regarding the electronic effects of the dinitrosyl iron unit will be in the calculation and modeling of the Mössbauer parameters of a series of $(L)_2Fe(NO)_2$ complexes, similar to previous studies by Ghosh, *et al.*[147-150] and Neese, *et al.*[92] Furthermore, additional studies are underway to assimilate the singlet, triplet, and quintet states of the tetrameric complexes with magnetic SQUID data, and to determine the true ground-state by means of broken-symmetry calculations. With these calculations, we can better understand the intricacies and versatility of the $\{Fe(NO)_2\}$ unit in a various ligand environments.

REFERENCES

1. Peters, J. W. *Curr. Opin. Struct. Biol.* **1999**, *9*, 670-676.
2. Bolin, J. T.; Ronco, A. E.; Mortenson, L. E.; Morgan, T. V.; Williamson, M.; Xuong, N. –H. *Nitrogen Fixation: Achievements and Objectives. Proc. 8th Int. Congr. Nitrogen Fixation*; Grashoff, P. M.; Roth, L. E.; Stacey, G.; Newton, W.E., Eds.; Chapman and Hall, New York, 1990.
3. Kim, J.; Rees, D. C. *Science* **1992**, *257*, 1677-1682.
4. Selmann, D. *Angew. Chem. Int. Ed. Eng.* **1993**, *32*, 64-67.
5. Doukov, T. I.; Iverson, T. M.; Seravalli, J.; Ragsdale, S. W.; Drennan, C. L. *Science* **2002**, *298*, 567-572.
6. Darnault, C.; Volbeda, A.; Kim, E. J.; Legrand, P.; Vernède, X.; Lindahl, P. A.; Fontecilla-Camps, J. C. *Nat. Struct. Biol.* **2003**, *10*, 271-279.
7. Wuerges, J.; Lee, J. –W.; Yim, Y. –I.; Yim, H. –S.; Kang, S. –O.; Carugo, K. D. *Proc. Nat. Acad. Sci.* **2004**, *101*, 8569-8574.
8. Barondeau, D. P.; Kassmann, C. J.; Bruns, C. K.; Tainer, J. A.; Getzoff, E. D. *Biochemistry* **2004**, *43*, 8038-8047.
9. Shin, W; Anderson, M. E.; Lindahl, P. A. *J. Am. Chem. Soc.* **1993**, *115*, 5522-5526.
10. Bramlett, M. R.; Tan, X.; Lindahl, P. A. *J. Am. Chem. Soc.* **2003**, *125*, 9316-9317.
11. Krüger, H. –J.; Peng, G.; Holm, R. H. *Inorg. Chem.* **1991***, 30*, 734-742.
12. Smee, J. J.; Miller, M. L.; Grapperhaus, C. A.; Reibenspies, J. H.; Darensbourg, M. Y. *Inorg. Chem.* **2001**, *40*, 3601-3605.

13. Darensbourg, M. Y.; Font, I.; Pala, M.; Reibenspies, J. H. *J. Coord. Chem.* **1994**, *32*, 39–49.

14. Mills, D. K.; Reibenspies, J. H.; Darensbourg, M. Y. *Inorg. Chem.* **1990**, *29*, 4364-4366.

15. Buonomo, R. M.; Goodman, D. C.; Musie, G.; Grapperhaus, C. A.; Maguire, M. J.; Lai, C.-H.; Hatley, M. L.; Smee, J. J.; Bellefeuille, J. A.; Darensbourg, M. Y. *Inorg. Synth.* **1998**, *32*, 89–98.

16. Golden, M. L.; Yarbrough, J. C.; Reibenspies, J. H.; Darensbourg, M. Y. *Inorg. Chem.* **2004**, *43*, 4702-4707.

17. Darensbourg, M. Y.; Tuntulani, T.; Reibenspies, J. H. *Inorg. Chem.* **1994**, *33*, 611-613.

18. Lyon, E. J.; Musie, G.; Reibenspies, J. H.; Darensbourg, M. Y. *Inorg. Chem.* **1998**, *37*, 6942-6946.

19. Bellefeuille, J. A.; Grapperhaus, C. A.; Buonomo, R. M.; Reibenspies, J. H.; Darensbourg, M. Y. *Organometallics*, **1998**, *17*, 4813-4821.

20. Font, I.; Buonomo, R. M.; Reibenspies, J. H.; Darensbourg, M. Y. *Inorg. Chem.*, **1993**, *32*, 5897-5898.

21. Musie, G.; Reibenspies, J. H.; Darensbourg, M. Y. *Inorg. Chem.* **1998**, *37*, 302-310.

22. Farmer, P. J.; Solouki, T.; Mills, D. K.; Soma, T.; Russell, D. H.; Reibenspies, J. H.; Darensbourg, M. Y. *J. Am. Chem. Soc.* **1992**, *114*, 4601-4605.

23. Rampersad, M. V.; Jeffery, S. P.; Golden, M. L.; Lee, J.; Reibenspies, J. H.; Darensbourg, D. J.; Darensbourg, M. Y. *J. Am. Chem. Soc.* **2005**, *127*, 17323-17334.

24. Rampersad, M. V.; Jeffery, S. P.; Reibenspies, J. H.; Ortiz, C. G.; Darensbourg, D. J.; Darensbourg, M. Y. *Angew. Chem. Int. Ed.* **2005**, *44*, 1217-1220.

25. Jeffery, S. P.; Singleton, M. L.; Reibenspies, J. H.; Darensbourg, M. Y. *Inorg. Chem.* **2007**, *46*, 179-185.

26. Phelps, A. L.; Rampersad, M. V.; Fitch, S. B.; Darensbourg, M. Y.; Darensbourg, D. J. *Inorg. Chem.* **2006**, *45*, 119-126.

27. Green, K. N.; Jeffery, S. P.; Reibenspies, J. H.; Darensbourg, M. Y. *J. Am. Chem. Soc.* **2006**, *128*, 6493-6498.

28. Green, K. N.; Rampersad, M. V.; Reibenspies, J. H.; Darensbourg, M. Y. *Dalton Trans.*, **2006**, 4244-4252.

29. Krishnan, R.; Riordan, C. G. *J. Am. Chem. Soc.* **2004**, *126*, 4484-4485.

30. Green, K. N.; Brothers, S. M.; Lee, B.; Darensbourg, M. Y.; Rockcliffe, D. A. *Inorg. Chem.* **2009**, *48*, 2780-2792.

31. Shearer, J.; Zhao, N *Inorg. Chem.*, **2006**, *45*, 9637-9639.

32. Shearer, J.; Long, L. M. *Inorg. Chem.* **2006**, *45*, 2358-2360.

33. Mullins, C. S.; Grapperhaus, C. A., Kozlowski, P. M. *J. Biol. Inorg. Chem.* **2006**, *11*, 617-625.

34. Green, K. N.; Brothers, S. M.; Jenkins, R. M.; Carson, C. E.; Grapperhaus, C. A.; Darensbourg, M. Y. *Inorg. Chem.* **2007**, *46*, 7536-7544.

35. Webster, C. E.; Darensbourg, M. Y. Lindahl, P. A.; Hall, M. B. *J. Am. Chem. Soc.*, **2004**, *126*, 3410-3411.

36. Hanns, J.; Krüger, H. –J. *Angew. Chem. Int. Ed. Engl.* **1996**, *35*, 2827-2830.

37. Bharadwaj, P. K.; Potenza, J. A.; Schugar, H. J. *J. Am. Chem. Soc.* **1986**, *108*, 1351-1352.

38. Houser, R. P.; Tolman, W. B. *Inorg. Chem.* **1995**, *34*, 1632-1633.

39. Mills, D. K.; Hsiao, Y. M.; Farmer, P. J.; Atnip, E. V.; Reibenspies, J. H.; Darensbourg, Y. D. *J. Am. Chem. Soc.* **1991**, *113*, 1421-1423.

40. Chiang, C. –Y.; Miller, M. L.; Reibenspies, J. H.; Darensbourg, M. Y. *J. Am. Chem. Soc.* **2004**, *126*, 10867-10874.

41. Chiang, C. –Y.; Lee, J.; Dalrymple, C.; Sarahan, M. C.; Reibenspies, J. H.; Darensbourg, M. Y. *Inorg. Chem.* **2005**, *44*, 9007-9016.

42. Hess, J. L.; Conder, H. L.; Green, K. N.; Darensbourg, M. Y. *Inorg. Chem.* **2008**, *47*, 2056-2063.

43. Osterloh, F.; Saak, W.; Haase, D.; Pohl, S. *Chem. Comm.* **1997**, 979-981.

44. Enemark, J. H.; Feltham, R. D. *Coord. Chem. Rev.* **1974**, *13*, 339-406.

45. Crabtree, R. H. *The Organometallic Chemistry of the Transition Metals*, 4th ed.; John Wiley & Sons, Inc.: New York, 2005.

46. Eisenberg, R.; Meyer, C. D. *Acc. Chem. Res.* **1975**, *8*, 26-34.

47. Brown, G.C.; Borutaite, V. *Cardiovascular Research*. **2007**, *75*, 283-290.

48. Fontijn, A.; Sabadell, A. J.; Ronco, R. J. *Anal. Chem.* **1970**, *42*, 575-579.

49. Lippard, S. J.; Berg, J. M. *Principles of Bioinorganic Chemistry*; University Science Books: Mill Valley, CA, 1994.

50. Culotta, E.; Koshland, Jr., D.E.. *Science*. **1992**, *258*, 1862-1865.

51. Rand, M.; Li, C.; La, M.; De Luca, A.; Najbar-Kaszkiel, A.; Jiang, F.; Di Iulio, J.; Ellis, A. *Asia Pac. J. Pharm.* **1997**, *12*, 137-148.

52. Talman, W.T. *Annals of the New York Acad. Sci.* **1997**, *835*, 225-233.

53. Lowenstein, C.J.; Dinerman, J.L.; Snyder, S.H. *Annals of Inter. Med.* **1994**, *120*, 227-237.

54. Gladwin, M.T.; Raat, N.J.H.; Shiva, S.; Dezfulian, C.; Hogg, N.; Kim-Shapiro, D.B.; Patel, R.P. *Amer. J. Physiol.* **2006**, *291*, H2026-H2035.

55. Nahrevanian, H.; Amini, M. *Iranian J. Basic Med. Sci.* **2009**, *11*, 197-204.

56. Tripathi, P. *Indian J. Biochem. and Biophys.* **2007**, *44*, 310-319.

57. Hayashi, T.; Miner, K. D.; Yeung, N.; Lin, Y. –W.; Lu, Y.; Moënne-Loccoz, P. *Biochem.* **2011**, *50*, 5939-5947.

58. Nagashima, S.; Nakasako, M.; Dohmae, N.; Tsujimura, M.; Takio, K.; Odaka, M.; Yohda, M.; Kamiya, N.; Endo, I. *Nat. Struct. Biol.* **1998**, *5*, 347-351.

59. Endo, I.; Nojiri, M.; Tsujimura, M.; Nakasako, M.; Nagashima, S.; Yohda, M.; Odaka, M. *J. Inorg. Biochem.* **2001**, *83*, 247-253.

60. Xu, N.; Yi, J.; Richter-Addo, G. B. *Inorg. Chem.* **2010**, *49*, 6253-6266.

61. Hsieh, C.-H.; Darensbourg, M.Y. *J. Am. Chem. Soc.* **2010**, *132*, 14118-14125.

62. Vanin, A.F.; Mikoyan, V.D.; Kubrina, L.H.; *Biophys.* **2010**, *55*, 5-12.

63. Chang, H.-H.; Hung, H.-J.; Ho, Y.-L.; Wen, Y.-D.; Huang, W.-N.; Chiou, S.-J. *Dalton Trans.* **2009**, 6396-6402.

64. Chen, Y.-J.; Ku, W.-C.; Feng, L.-T.; Tsai, M.-L.; Hsieh, C.-H.; Hsu, W.-H.; Liaw, W.-F.; Hung, C.-H.; Chen, Y.-J. *J. Am. Chem. Soc.* **2008**, *130*, 10929-10938.

65. Tsai, M.-L.; Hsieh, C.-H.; Liaw, W.-F. *Inorg. Chem.* **2007**, *46*, 5110-5117.

66. Lu, T.-T.; Chiou, S.-J.; Chen, C.-Y.; Liaw, W.-F. *Inorg. Chem.* **2006**, *45*, 8799-8806.

67. Tsai, M.-L.; Liaw, W.-F. *Inorg. Chem.* **2006,** *45*, 6583-6585.

68. Dillinger, S.A.T.; Schmalle, H.W.; Fox, T.; Berke, H. *Dalton Trans.* **2007**, 3562-3571.

69. Cesareo, E.; Parker, L. J.; Pedersen, J. Z.; Nuccetelli, M.; Mazzetti, A. P.; Pastore, A.; Federici, G.; Caccuri, A. M.; Ricci, G.; Adams, J. J.; Parker, M. W.; Lo Bello, M. *J. Biol. Chem.* **2005**, *280*, 42172-42180.

70. Rakova, O. A.; Sanina, N. A.; Shilov, G. V.; Shul'ga, Y. M.; Martynenko, V. M.; Ovanesyan, N. S.; Aldoshin, S. M. *Russ. J. Coord. Chem.* **2002**, *28*, 341-345.

71. Sanina, N. A.; Rakova, O. A.; Aldoshin, S. M.; Chuev, I. I.; Atovmyan, E. G.; Ovanesyan, N. S. *Russ. J. Coord. Chem.* **2001**, *27*, 179-183.

72. Glidewell, C.; Harman, M.E.; Hursthouse, M.B.; Johnson, I.L.; Motevalli, M. *J. Chem. Res., Syn.* **1988**, 212-213.

73. Marsh, R.E.; Spek, A.L. *Acta. Crystallogr.* **2001**, *57*, 800-805.

74. Harrop, T.C.; Song, D.; Lippard, S.J. *J. Inorg. Biochem.* **2007**, *101*, 1730-1738.

75. Harrop, T.C.; Song, D.; Lippard, S.J. *J. Am. Chem. Soc.* **2006**, *128*, 3528-3529.

76. Chen, Y.-J.; Ku, W.-C.; Feng, L.-T.; Tsai, M.-L.; Hsieh, C.-H.; Hsu, W.-H.; Liaw, W.-F.; Hung, C.-H.; Chen, Y.-J. *J. Am. Chem. Soc.*, **2008**, *130*, 10929-10938.

77. Lu,T.-T.; Tsou, C.-C.; Huang, H.-W.; Hsu, I.-J.; Chen, J.-M.; Kuo, T.-S.; Wang, Y.; Liaw, W.-F. *Inorg. Chem.* **2008**, *47*, 6040-6050.

78. Tsou, C.-C.; Lu, T.-T.; Liaw, W.-F. *J. Am. Chem. Soc.* **2007**, *129*, 12626-12627.

79. Wang, R.; Camacho-Fernandez, M.A.; Xu, W.; Zhang, J.; Li, L. *Dalton Trans.* **2009**, 777-786.

80. Wang, X.; Sundberg, E. B.; Li, L.; Kantardjieff, K. A.; Herron, S. R.; Lim, M.; Ford, P. C. *Chem. Comm.*, **2005**, 477-479.

81. Atkinson, F. L.; Blackwell, H. E.; Brown, N. C.; Connelly, N. G.; Crossley, J. G.; Orpen, A. G.; Rieger, A. L.; Rieger, P. H. *Dalton Trans.*, **1996**, 3491-3502.

82. Bitterwolf, T. E.; Steele, B. *Inorg. Chem. Comm.* **2006**, *9*, 512-513.

83. Dessy, R. E.; Charkoudian, J. C.; Rheingold, A. L. *J. Am. Chem. Soc.* **1972**, *94*, 738-745.

84. Mazak, R. A.; Collins, R. L. *J. Chem. Phys.* **1969**, *51*, 3220-3225.

85. Wang, R.; Wang, X.; Sundberg, E. B.; Nguyen, P.; Grant, G. P. G.; Sheth, C.; Zhao, Q.; Herron, S.; Kantardjieff, K. A.; Li, L. *Inorg. Chem.* **2009**, *48*, 9779-9785.

86. Tsai, M. –C.; Tsai, F. –T.; Lu, T. –T.; Tasai, M. –L; Wei, Y. –C.; Hsu, I. –J.; Lee, J. –F.; Liaw, W. –F. *Inorg. Chem.* **2009**, *48*, 9579-9591.

87. Woolum, J. C.; Tiezzi, E.; Commoner, B. *Biochim. Biophys. Acta* **1968**, *160*, 311-320.

88. Wang, J. –H.; Chen, C –H. *Inorg. Chem.* **2010**, *49*, 7644-7646.

89. Hess, J. L.; Hsieh, C. –H.; Reibenspies, J. H.; Darensbourg, M. Y. *Inorg. Chem.* **2011**, *50*, 8541-8552.

90. Tonzetich, Z. J.; Héroguel, F.; Do, L. H.; Lippard, S. J. *Inorg. Chem.* **2011**, *50*, 1570-1579.

91. Tonzetich, Z. J.; Do, L. H.; Lippard, S. J. *J. Am. Chem. Soc.* **2009**, *131*, 7964-7965.

92. Ye, S.; Neese, F. *J. Am. Chem. Soc.* **2010**, *132*, 3646-3647.

93. Ghosh, A. *Coord. Chem. Rev.* **2009**, *253*, 523-525.

94. Zvereva, E. E.; Shagidullin, A. R.; Katsyuba, S. A. *J. Phys. Chem. A* **2011,** *115*, 63-69.

95. Surawatanawong, P.; Tye, J. W.; Darensbourg, M. Y.; Hall, M. B. *Dalton Trans.* **2010**, *39*, 3093-3104.

96. Ruiz, E.; Cirera, J.; Alvarez, S. *Coord. Chem. Rev.* **2005**, *249*, 2649-2660.

97. Sinnecker, S.; Slep, L. D.; Bill, E.; Neese, F. *Inorg. Chem.* **2005**, *44*, 2245-2254.

98. Neese, F. *Coord. Chem. Rev.* **2009**, *253*, 526-563.

99. Gencic, S.; Grahame, D.A. *J. Biol. Chem.* **2003**, *278*, 6101-6110.

100. Becke, A.D. *J. Chem. Phys.* **1993**, *98*, 5648-5652.

101. Lee, C.; Yang, W.; Parr, R.G. *Phys. Rev. B.* **1988**, *37*, 785-789.

102. Tao, J.M.; Perdew, J.P.; Staroverov, V.N.; Scuseria, G.E. *Phys. Rev. Lett.* **2003**, *91*, 146401-1-146401-4.

103. Cramer, C. J. *Essentials of Computational Chemistry*, 2nd ed.; Wiley: West Sussex, U.K., 2004.

104. Allinger, N. L.; Burkett, U. *Molecular Mechanics*; Washington: American Chemical Society, 1982.

105. Schrödinger, E. *Phys. Rev.* **1928**, *28*, 1049-1070.

106. Born, M.; Oppenheimer, R. *Annalen. Der Physik* **1927**, *389*, 457-484.

107. McQuarrie, D. A. *Physical Chemistry: A Molecular Approach*; University Science Books: Sausalito, CA, 1997.

108. Hohenberg, P.; Kohn, W. *Phys. Rev. B* **1964**, *136*, B864-B871.

109. Kohn, W.; Sham, L. J. *Phys. Rev. A.* **1965**, *140*, A1133-A1138.

110. Thomas, L. H. *Math. Proc. Cambridge Phil. Soc.* **1927**, *23*, 542-548.

111. Fermi, E. *Rend. Accad. Naz. Lincei* **1927**, *6*, 602-607.

112. Heisenberg, W. *Zeitschrift für Physik* **1926**, *38*, 411-426.

113. Dirac, P. A. M. *Proc. Royal Soc. London* **1926**, *112*, 661-667.

114. Becke, A.D. *Phys. Rev. A*. **1988**, *38*, 3098-3100.

115. Perdew, J.P. *Phys. Rev. B*. **1986**, *33*, 8822-8824.

116. Chai, J.-D.; Head-Gordon, M. *Phys. Chem. Chem. Phys.* **2008**, *10*, 6615-6620.

117. Noodleman, L. *J. Chem. Phys.*, **1981**, *74*, 5737-5743.

118. Noodleman, L.; Case, D. A.; Aizman, A. *J. Am. Chem. Soc.* **1988**, *110*, 1001-1005.

119. Frisch, M. J.; Trucks, G. W.; Schlegel, H. B.; Scuseria, G. E.; Robb, M. A.; Cheeseman, J. R.; Montgomery, Jr., J. A.; Vreven, T.; Kudin, K. N.; Burant, J. C.; Millam, J. M.; Iyengar, S. S.; Tomasi, J.; Barone, V.; Mennucci, B.; Cossi, M.; Scalmani, G.; Rega, N.; Petersson, G. A.; Nakatsuji, H.; Hada, M.; Ehara, M.; Toyota, K.; Fukuda, R.; Hasegawa, J.; Ishida, M.; Nakajima, T.; Honda, Y.; Kitao, O.; Nakai, H.; Klene, M.; Li, X.; Knox, J. E.; Hratchian, H. P.; Cross, J. B.; Bakken, V.; Adamo, C.; Jaramillo, J.; Gomperts, R.; Stratmann, R. E.; Yazyev, O.; Austin, A. J.; Cammi, R.; Pomelli, C.; Ochterski, J. W.; Ayala, P. Y.; Morokuma, K.; Voth, G. A.; Salvador, P.; Dannenberg, J. J.; Zakrzewski, V. G.; Dapprich, S.; Daniels, A. D.; Strain, M. C.; Farkas, O.; Malick, D. K.; Rabuck, A. D.; Raghavachari, K.; Foresman, J. B.; Ortiz, J. V.; Cui, Q.; Baboul, A. G.; Clifford, S.; Cioslowski, J.; Stefanov, B. B.; Liu, G.; Liashenko, A.; Piskorz, P.; Komaromi, I.; Martin, R. L.; Fox, D. J.; Keith, T.; Al-

Laham, M. A.; Peng, C. Y.; Nanayakkara, A.; Challacombe, M.; Gill, P. M. W.; Johnson, B.; Chen, W.; Wong, M. W.; Gonzalez, C.; and Pople, J. A. *Gaussian 03*, Revision C.02; Gaussian, Inc.: Wallingford CT, 2004.

120. Frisch, M. J.; Trucks, G. W.; Schlegel, H. B.; Scuseria, G. E.; Robb, M. A.; Cheeseman, J. R.; Scalmani, G.; Barone, V.; Mennucci, B.; Petersson, G. A.; Nakatsuji, H.; Caricato, M.; Li, X.; Hratchian, H. P.; Izmaylov, A. F.; Bloino, J.; Zheng, G.; Sonnenberg, J. L.; Hada, M.; Ehara, M.; Toyota, K.; Fukuda, R.; Hasegawa, J.; Ishida, M.; Nakajima, T.; Honda, Y.; Kitao, O.; Nakai, H.; Vreven, T.; Montgomery, Jr., J. A.; Peralta, J. E.; Ogliaro, F.; Bearpark, M.; Heyd, J. J.; Brothers, E.; Kudin, K. N.; Staroverov, V. N.; Kobayashi, R.; Normand, J.; Raghavachari, K.; Rendell, A.; Burant, J. C.; Iyengar, S. S.; Tomasi, J.; Cossi, M.; Rega, N.; Millam, N. J.; Klene, M.; Knox, J. E.; Cross, J. B.; Bakken, V.; Adamo, C.; Jaramillo, J.; Gomperts, R.; Stratmann, R. E.; Yazyev, O.; Austin, A. J.; Cammi, R.; Pomelli, C.; Ochterski, J. W.; Martin, R. L.; Morokuma, K.; Zakrzewski, V. G.; Voth, G. A.; Salvador, P.; Dannenberg, J. J.; Dapprich, S.; Daniels, A. D.; Farkas, Ö.; Foresman, J. B.; Ortiz, J. V.; Cioslowski, J.; Fox, D. J. *Gaussian 09*, Revision A.1, Gaussian, Inc.: Wallingford CT, 2009.

121. Neese, F. *ORCA – an ab initio, Density Functional and Semiempirical program package*, Version 2.6. University of Bonn, 2008.

122. Dennington, R., II; Keith, T.; Millam, J.; Eppinnett, K.; Hovell, W. L.; Gilliland, R.; *GaussView*, version 3.09; Semichem, Inc.: Shawnee Mission, KS, 2003.

123. AMPAC ™ 9, Semichem, Inc., 12456 W 62nd Terrace – Suite D, Shawnee, KS 66216, 1992-2008.

124. Krishnan, R.; Binkley, J. S.; Seeger, R.; Pople, J. A. *J. Chem. Phys.* **1980**, *72*, 650-654.

125. Wachters, A. J. H. *J. Chem. Phys.*, **1970**, *52*, 1033-1036.

126. Hay, P. J. *J. Chem. Phys.* **1977**, *66*, 4377-4384.

127. Raghavachari, K.; Trucks, G.W. *J. Chem. Phys.* **1989**, *91*, 1062-1065.

128. *Cerius*^{2}, version 3.0; MSI: Cambridge, U.K.

129. Manson, J.; Webster, C. E.; Pérez, L. M.; Hall, M. B. *JIMP2*. http://www.chem.tamu.edu/jimp2/ (accessed Oct 26, 2007).

130. Zhao, Y.; Truhlar, D.G. *Theor. Chem. Acc.* **2008**, *120*, 215-241.

131. Kaupp, M.; Schleyer, P.V.R.; Stoll, H.; Preuss, H. *J. Chem. Phys.* **1991**, *94,* 1360-1366.

132. Hay, P. J.; Wadt, W. R. *J. Chem. Phys.*, **1985**, *82*, 270-283.

133. Check, C.E.; Faust, T.O.; Bailey, J.M.; Wright, B.J.; Gilbert, T.M.; Sunderlin, L.S. *J. Phys. Chem. A*, **2001**, *105*, 8111-8116.

134. Sun, Y. –M.; Liu, C. –B.; Lin, X. –J.; Bi, S. –W. *New J. Chem.*, **2004**, *28*, 270-274.

135. Hatlevik, Ø; Blanksma, M. C.; Mathrubootham, V.; Arif, A. M.; Hegg, E. L. *J. Biol. Inorg. Chem.* **2004**, *9*, 238-246.

136. Jenkins, R. M.; Singleton, M. L.; Almaraz, E.; Reibenspies, J. H.; Darensbourg, M. Y. *Inorg. Chem.* **2009**, *48*, 7280-7293.

137. Jenkins, R. M.; Singleton, M. L.; Leamer, L. A.; Reibenspies, J. H.; Darensbourg, M. Y. *Inorg. Chem.*, **2010**, *49*, 5503-5514.

138. Colman, P. M.; Freeman, H. C.; Guss, J. M.; Murata, M.; Norris, V. A.; Ramshaw, J. A. M.; Venkatappa, M. P. *Nature* **1978**, *272*, 319-324.

139. Greenwood, N.N.; Earnshaw, A. *Chemistry of the Elements*, 2nd Ed., Elsevier: Jordan Hill, Oxford, U.K., 2003.

140. Holm, R.H.; Kennepohl, P.; Solomon, E.I. *Chem. Rev.* **1996**, *96*, 2239-2314.

141. Casella, L.; Ibers, J. A. *Inorg. Chem.* **1981**, *20*, 2438-2448.

142. Klein, E. L.; Khan, M. A.; Houser, R. P. *Inorg. Chem.* **2004**, *43*, 7272-7274.

143. Pratesi, A.; Zanello, P.; Giorgi, G.; Messori, L.; Laschi, F.; Casini, A.; Corsini, M.; Gabbiani, C.; Orfei, M.; Rosani, C.; Ginanneschi, M. *Inorg. Chem.* **2007**, *46*, 10038-10040.

144. Fiedler, A. T.; Bryngelson, P. A.; Maroney, M. J.; Brunold, T. C. *J. Am. Chem. Soc.* **2005**, *127*, 5449-5462.

145. Bellefeuille, J. A.; Grapperhaus, C. A.; Derecskei-Kovacs, A.; Reibenspies, J. H.; Darensbourg, M. Y. *Inorg. Chim. Acta* **2000**, 73-81.

146. Sanina, N. A.; Rakova, O. A.; Aldoshin, S. M.; Shilov, G. V.; Shul'ga, Y. M.; Kulikov, A. V.; Ovanesyan, N. S. *Mendeleev Commun.* **2004**, 7-8.

147. Conradie, J.; Hopmann, K. H.; Ghosh, A. *J. Phys. Chem. B* **2010**, *114*, 8517-8524.

148. Hopmann, K. H.; Noodleman, L.; Ghosh, A. *Chem. – Eur. J.* **2010**, *16*, 10397-10408.

149. Hopmann, K. H.; Ghosh, A.; Noodleman, L. *Inorg. Chem.* **2009**, *48*, 9155-9165.

150. Hopmann, K. H.; Conradie, J.; Ghosh, A. *J. Phys. Chem. B* **2009**, *113*, 10540-10547.

151. Jaworska, M. *Polyhedron* **2007**, *26*, 3247-3254.

152. Shestakov, A. F.; Shul'ga, Y. M.; Emel'yanova, N. S.; Sanina, N. A.; Aldoshin, S. M. *Russ. Chem. Bull., Int. Ed.* **2007**, *56*, 1289-1297.

153. Hedberg, L.; Hedberg, K.; Satija, S. K.; Swanson, B. I. *Inorg. Chem.* **1985**, *24*, 2766-2771.

154. Chen, H. –W.; Lin, C. –W.; Chen, C. –C.; Yang, L. –B.; Chiang, M. –H.; Liaw, W. –F. *Inorg. Chem.* **2005**, *44*, 3226-3232.

155. Davies,, S. C.; Evans, D. J.; Hughes, D. L.; Konkol, M.; Richards, R. L.; Sanders, J. R.; Sobota, P. *Dalton Trans.* **2002**, 2473-2482.

156. Conradie, J.; Quarless, D. A., Jr.; Hsu, H. –F.; Harrop, T. C.; Lippard, S. J.; Koch, S. A.; Ghosh, A. *J. Am. Chem. Soc.* **2007**, *129*, 10446-10456.

157. Brown, C. A.; Pavlosky, M. A.; Westre, T. E.; Zhang, Y.; Hedman, B.; Hodgson, K. O.; Solomon, E. I. *J. Am. Chem. Soc.* **1995**, *117*, 715-732.

158. Brothers, S. M.; Darensbourg, M. Y.; Hall, M. B. *Inorg. Chem.* **2011**, *50*, 8532-8540.

159. Sellers, V. M.; Johnson, M. K.; Dailey, H. A. *Biochemistry* **1996**, *35*, 2699-2704.

160. Ding, H.; Demple, B.; *Proc. Natl. Acad. Sci. U.S.A.* **2000**, *97*, 5146-5150.

161. Loach, P. A. Oxidation-Reduction Potentials, Absorbance Bands, and Molar Absorbance of Compounds Used in Biochemical Studies. In *Handbook of*

Biochemistry and Molecular Biology, *Physical and Chemical Data*; Fasman, G. D., Ed.; CRC Press: Boca Raton, FL, 1976; Vol. 1, 123-130.

162. Fontecilla-Camps, J. C.; Volbeda, A.; Cavazza, C.; Nicolet, Y. *Chem. Rev.* **2007**, *107*, 4273-4303.

163. Zhu, W.; Marr, A. C.; Wang, Q.; Neese, F.; Spencer, D. J. E.; Blake, A. J.; Cooke, P. A.; Wilson, C.; Schröder, M. *Proc. Natl. Acad. Sci. U.S.A.* **2005**, *102*, 18280.

164. Li, Z. L.; Ohki, Y.; Tatsumi, K. *J. Am. Chem. Soc.* **2005**, *127*, 8950.

165. Ohki, Y.; Yasumura, K.; Ando, M.; Shimokata, S.; Tatsumi, K. *Proc. Natl. Acad. Sci. U.S.A.* **2010**, *107*, 3994-3997.

166. Lai, C. –H.; Reibenspies, J. H.; Darensbourg, M. Y. *Angew. Chem. Int. Ed. Engl.* **1996**, *35*, 2390-2393.

167. Hsieh, C. –H.; Chupik, R. B.; Brothers, S. M.; Hall, M. B.; Darensbourg, M. Y. *Dalton Trans.* **2011**, *40*, 6047-6053.

168. Dey, A.; Green, K. N.; Jenkins, R. M.; Jeffrey, S. P.; Darensbourg, M. Y.; Hodgson, K. O.; Hedman, B.; Solomon, E. I. *Inorg. Chem.*, **2007**, *46*, 9655-9660.

169. Miller, M. L.; Ibrahim, S. A.; Golden, M. L.; Darensbourg, M. Y. *Inorg. Chem.* **2003**, *42*, 2999-3007.

170. Kolks, G.; Frihart, C. R.; Coughlin, P. K.; Lippard, S. J. *Inorg. Chem.* **1981**, *20*, 2933-2940.

171. Kolks, G.; Lippard, S. J.; Waszczak, J. V.; Lilienthal, H. R. *J. Am. Chem. Soc.* **1982**, *104*, 717-725.

172. Chaudhuri, P.; Karpenstein, I.; Winter, M.; Lengen, M.; Butzlaff, C.; Bill, E.; Trautwein, A. X.; Flörke, U.; Haupt, H. –J. *Inorg. Chem.* **1993**, *32*, 888-894.

173. Dewan, J. C.; Lippard, S. J. *Inorg. Chem.* **1980**, *19*, 2079-2082.

174. Sun, N.; Liu, L. V.; Dey, A.; Villar-Acevedo, G.; Kovacs, J. A.; Darensbourg, M. Y.; Hodgson, K. O.; Hedman, B.; Solomon, E. I. *Inorg. Chem.* **2011,** *50*, 427-436.

175. Dey, A.; Jeffrey, S. P.; Darensbourg, M. Y.; Hodgson, K. O.; Heddman, B.; Solomon, E. I. *Inorg. Chem.* **2007**, *46*, 4989-4996.

VITA

Scott Michael Brothers was born in Wheeling, WV in March 1983 and received his Bachelor of Science degree in chemistry from Wheeling Jesuit University in 2005, graduating *Summa cum Laude*. He began his graduate studies at Texas A&M University in the summer of 2005 under the direction of Marcetta Y. Darensbourg and later joined the group of his coadvisor, Michael B. Hall in the summer of 2010 and defended his Ph.D. in October 2011. Scott can be contacted either through his parents, Jeff and Cheryl Brothers at 55223 Maple Ave., Lansing, OH 43934 or through Marcetta Y. Darensbourg at the Department of Chemistry, Texas A&M University, Mail Stop 3255, College Station, TX 77843-3255 or at marcetta@mail.chem.tamu.edu.